FLOW SIMULATION AND CHARACTERIZATION OF FRACTURE SYSTEMS USING FAST MARCHING METHOD AND NOVEL DIAGNOSTIC PLOTS

A Dissertation

by

XU XUE

Submitted to the Office of Graduate and Professional Studies of
Texas A&M University
in partial fulfillment of the requirements for the degree of

DOCTOR OF PHILOSOPHY

Chair of Committee,	Akhil Datta-Gupta
Committee Members,	Michael J. King
	Nobuo Morita
	Debjyoti Banerjee
Head of Department,	Jeff Spath

May 2019

Major Subject: Petroleum Engineering

ABSTRACT

Recently, the industrial trend of hydraulic fracturing is reducing the cluster spacing while increasing the fluid and proppant usage, which often generates complex fracture networks. The challenge from this trend is to understand and characterize the complex fracture networks. Recently, a novel approach has been proposed based on the high-frequency asymptotic solution of the diffusivity equation leading to the Eikonal equation. The Eikonal equation governs the pressure front propagation and can be solved by a front-tracking algorithm called Fast Marching Method (FMM). In this dissertation, we extend this method to complex fracture networks characterization and simulation, using novel diagnostic plots and FMM-based simulation.

First, we develop novel diagnostic plots for complex fracture networks characterization. We directly use the field data to calculate the well drainage volume, instantaneous recovery ratio (IRR) and w(τ) function. The w(τ) function serves as a diagnostic plot to detect fracture geometry and flow regimes and the IRR plot is used to detect fracture conductivity.

Second, we extend the FMM-based simulation workflow to local grid refinements (LGRs). The detailed workflow is proposed to generate the computational grid for the diffusive time of flight (DTOF) calculation. We use various models to validate the accuracy and computational efficiency of this workflow. In addition, we investigate various discretization schemes for the transition between local and global domain.

Third, we extend the FMM-based simulation workflow to embedded discrete fracture model (EDFM). We utilize a novel gridding to link the embedded discrete fractures and the matrix based on Delaunay triangulation. Using the DTOF as a spatial coordinate, the FMM-based flow simulation reduces the 3D complex fracture networks simulation to an equivalent 1D simulation. Multiple examples are shown to validate the accuracy and computational efficiency of this workflow.

Lastly, we investigate the impact of tighter cluster spacing of the hydraulic fractures using the Eagle Ford field data. The hydraulic fracture propagation simulator Mangrove® is used to generate the fracture patterns based on the completion data. A manual history matching is conducted to match the field injection treatment pressure. The impact of cluster spacing is examined through the calibrated fracture models.

DEDICATION

To my parents and wife for their endless love and support.

ACKNOWLEDGEMENTS

I would like to express my gratitude to my advisor, Dr. Akhil Datta-Gupta for his guidance and financial support throughout my Ph.D. study. He has helped me overcome many obstacles in my life and research. He offered significant support of my internships at Chevron, which made an excellent starting point for my future career.

I would like to thank Dr. Michael J. King for his valuable ideas and discussion through my Ph.D. study. Many of the ideas that served as the basis for this dissertation resulted from my discussions with Dr. King. I am grateful to my other committee members, Dr. Nobuo Morita and Dr. Debjyoti Banerjee for their comments and suggestions to improve the quality of this work.

I would like to thank Chevron ETC for offering me three times internship and full time job. These opportunities allowed me to gain knowledge and industry experience.

Special thanks to all my friends in the MCERI group, petroleum department and Texas A&M University for making my Ph.D. journey an unforgettable experience.

Finally, thanks to my parents and beloved wife, Shuang Zhang for their endless love and support.

CONTRIBUTORS AND FUNDING SOURCES

Contributors

This work was supervised by a dissertation committee consisting of Professor Akhil Datta-Gupta (advisor), Michael J. King, and Nobuo Morita of the Department of Petroleum Engineering and Professor Debjyoti Banerjee of the Department of Mechanical Engineering.

The quantitative analysis using the $w(\tau)$ plot in Chapter II was in collaboration with Jaeyoung Park and was published in 2018. In Chapter IV, the EDFM validation results include contributions by Tsubasa Onishi. This work will be published in an upcoming SPE conference (SPE-193822-MS). The Chapter V of this dissertation was in collaboration with Rongqiang Chen. He contributed to the production history matching part, which will be included in his dissertation.

All other work conducted for the dissertation was completed by the student independently.

Funding Sources

This work was made possible by the financial support of the member companies of the Model Calibration and Efficient Reservoir Imaging (MCERI) consortium.

TABLE OF CONTENTS

LIST OF FIGURES

Page

LIST OF TABLES

CHAPTER I

INTRODUCTION AND LITERATURE REVIEW[*]

1.1 Introduction

Unconventional tight/shale reservoirs development has become a topic of interest in the oil and gas industry, and the production from this kind of reservoirs contributes significantly to the energy market in the US and the world (Holditch 2013). The common practice of the ultra-low permeability reservoir development is utilizing a long horizontal well with multistage hydraulic fractures. This technology directly introduced the shale revolution in the US. Recently, the industrial trend of hydraulic fracturing is reducing the cluster spacing while increasing the fluid and proppant usage. This strategy often generates complex fracture networks, which significantly enhances the well productivity (Huang et al. 2016; Zhou, J. et al. 2016; Evans et al. 2018; Tang et al. 2018c; Tang et al. 2018d). However, due to the complexity of the hydraulic fracture networks as well as the fluid flow mechanisms between fractures and matrix such as spontaneous imbibition and water adsorption etc., characterization and simulation remain a challenging task (Deng and King 2016, 2018, 2019). Right now, the most popular techniques to understand the complex fracture networks include microseismic monitoring (Tafti and Aminzadeh 2012;

---

[*] Part of this section is reprinted with permission from "Reservoir and Fracture Flow Characterization Using a Novel w(τ) Formulation" by Xue et al. (2016), paper URTEC-2440083-MS presented at the Unconventional Resources Technology Conference, 1-3 Aug., San Antonio, Texas, USA. Copyright [2016] URTEC.

Grechka et al. 2018), distributed temperature and acoustic sensing (Zhang and Zhu 2017; Zhu et al. 2018; Zhang and Zhu 2019a, 2019b) and well logging (Maity and Aminzadeh 2012; An et al. 2017; Xian et al. 2018).

From the reservoir engineering point of view, we either use the analytical method or numerical reservoir simulation method to characterize and optimize the complex fracture networks. The analytical methods, mainly the decline curve analysis and pressure/rate transient analysis, are still the most common techniques in the industry to quickly understand the reservoir and fractures. The original idea of the decline curve analysis dates back to 1945. Arps (1945) first designed this method for conventional reservoirs with vertical wells under boundary-dominated flow. After that, many researchers modified and extended this method to unconventional reservoirs to predict the well production rate, estimated ultimate recovery (EUR) and reserves (Duong 1989; Valko and Lee 2010). The decline curve analysis is easy to use on large number of wells and only requires minimal data to make the prediction. However, this method is lack of physics and is often associated with huge uncertainty when predicting the EUR. The pressure/rate transient analysis is an alternate way to understand the reservoir and fractures (Al-Kobaisi et al. 2006; Song and Ehlig-Economides 2011). Using this method, we first identify different flow regimes then estimate the reservoir and fracture properties as well as the reserve from the corresponding flow regimes. Although the equations of the pressure/rate transient analysis are derived directly from the physical models, we usually assume homogeneous reservoir with planar fractures. These assumptions and the poor quality of the field production data often make the interpretation unreliable. However, ease of use property still makes the analytical methods the dominant tool for unconventional reservoir analysis.

Numerical reservoir simulation is another way to understand and characterize the reservoir and fractures. This method also has a long history for fractured reservoir analysis. The simplest way to simulate the fractured reservoir is the dual continuum model, which dates back to 1963 by Warren and Root (1963). Currently, the most popular techniques for fractured reservoir modeling are local grid refinements (LGRs), discrete fracture model (DFM) and embedded discrete fracture model (EDFM) (Mohammed and Al-Ansari 1995; Karimi-Fard and Firoozabadi 2001; Karimi-Fard et al. 2004; Li and Lee 2008; Moinfar et al. 2014). All of these methods require a detailed geological model as well as explicit fracture geometries. Compared with the analytical methods, the numerical reservoir simulation can handle reservoir heterogeneity, complex fracture geometries, and complex physics. However, the numerical reservoir simulation often requires long time of computation, especially at the field level. For the characterization and optimization purpose, we often require to run the simulation thousands of time. The computational efficiency is currently the bottleneck of the numerical reservoir simulation to the application of unconventional reservoirs characterization and optimization.

Recently the Fast Marching Method (FMM) based flow simulation has shown great promise for rapid modeling of unconventional reservoirs (Xie et al. 2015a; Fujita et al. 2016; Zhang et al. 2016; Iino et al. 2017; Iino and Datta-Gupta 2018; lino et al. 2018). The FMM-based simulation is based on the high frequency limit of the asymptotic solution of the diffusivity equation. The corresponding Eikonal equation governs the pressure front propagation (Vasco et al. 2000). By solving the Eikonal equation, we obtain the diffusive time of flight (DTOF), which is a generalization of the 'radius of investigation'. Using the DTOF as a spatial coordinate, we transform the original 3D model to an equivalent 1D model and solve the fluid flow equations. The FMM-based simulation stands midway between the analytical methods and numerical reservoir simulation. This method can handle complex physics while increasing the computational speed orders of magnitude faster than the traditional numerical reservoir simulation.

1.2 Literature Review

In this section, we provide a brief literature review of the Fast Marching Method and the FMM-based simulation.

1.2.1 Fast Marching Method and Diffusive Time of Flight

The starting point is the diffusivity equation in slightly compressible system, which can be expressed as:

$$\phi\left(x\right)\mu c_t \frac{\partial p(x,t)}{\partial t} - \nabla \cdot \left(k(x)\cdot \nabla p(x,t)\right) = 0 \tag{1.1}$$

The high frequency limit of the diffusivity equation, which represents the rapidly varying component in pressure, gives rise to the Eikonal equation for the DTOF τ(x) (Kulkarni et al. 2000; Vasco et al. 2000). The Eikonal equation is expressed as:

$$\nabla \tau\left(x\right)\cdot \alpha(x)\cdot \nabla \tau\left(x\right) = 1 \tag{1.2}$$

The α denotes the diffusivity and can be calculated as:

$$\alpha = \frac{\lambda_t k}{\phi c_t} \tag{1.3}$$

where λ_t is total mobility, k is permeability, ϕ is porosity and c_t is total compressibility. The Eikonal equation governs the pressure front propagation in the reservoir and the DTOF serves as the footprint of the pressure front (Datta-Gupta et al. 2011). This idea is a generalization of the 'radius of investigation' in homogeneous reservoir. Figure 1.1 illustrates a comparison of the 'radius of investigation' in homogeneous reservoir and the DTOF in heterogeneous reservoir. The cylindrical contours in homogeneous reservoir become twisted irregular contours because of reservoir heterogeneity. However, the DTOF captures the pressure front propagation.

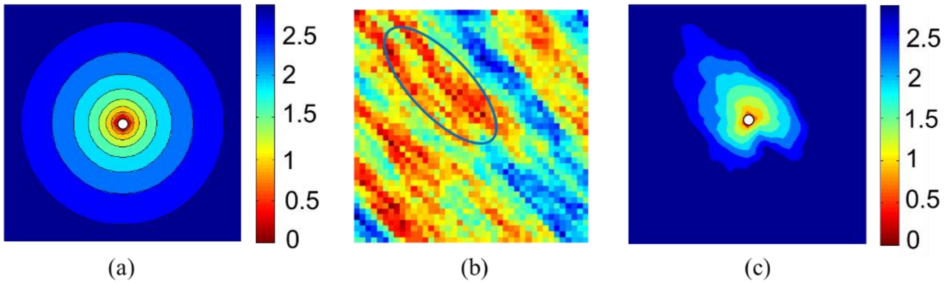

(a) (b) (c)

Figure 1.1 Examples of the pressure front propagation (a) Radius of investigation in homogeneous reservoir (b) Log permeability field (c) DTOF in heterogeneous reservoir (reprinted from Datta-Gupta et al. 2011)

The Eikonal equation can be efficiently solved by a front-tracking algorithm called the Fast Marching Method. The FMM was first proposed by Sethian (1996) to efficiently solve the Eikonal equation. FMM is a single-pass method which utilizes the fact that the value of τ(x) for the first-order partial differential equation depends only on the value of τ along the characteristic(s) passing through the point (Sethian 1996). Analogous to the Dijkstra's algorithm to solve the shortest path problem (Dijkstra 1959), FMM directly tracks the pressure wave starting from the source or sink. Figure 1.2 provides the basic framework of the FMM calculation, which comprises of the following steps (Sethian 1999):

(1) Label all grid nodes as *unknown*;

(2) Assign τ values (usually zero) to the nodes corresponding to the source or sink. Usually the source or sink are the wells or completions. Label them as *accepted* (Figure 1.2(a));

(3) For each node that is *accepted*, locate its immediate neighboring nodes that are *unknown* and label them as *considered* (Figure 1.2(b) points A, B, C, D);

(4) For each node labeled as *considered*, update its τ value using the minimum local solutions (Update the τ values for points A, B, C, D in Figure 1.2(b));

(5) Once we update all the nodes labeled as *considered*, we pick up the node, which has the minimum τ value, and label it as *accepted* (Figure 1.2(b) points A);

(6) Go to step (3) until all nodes are accepted.

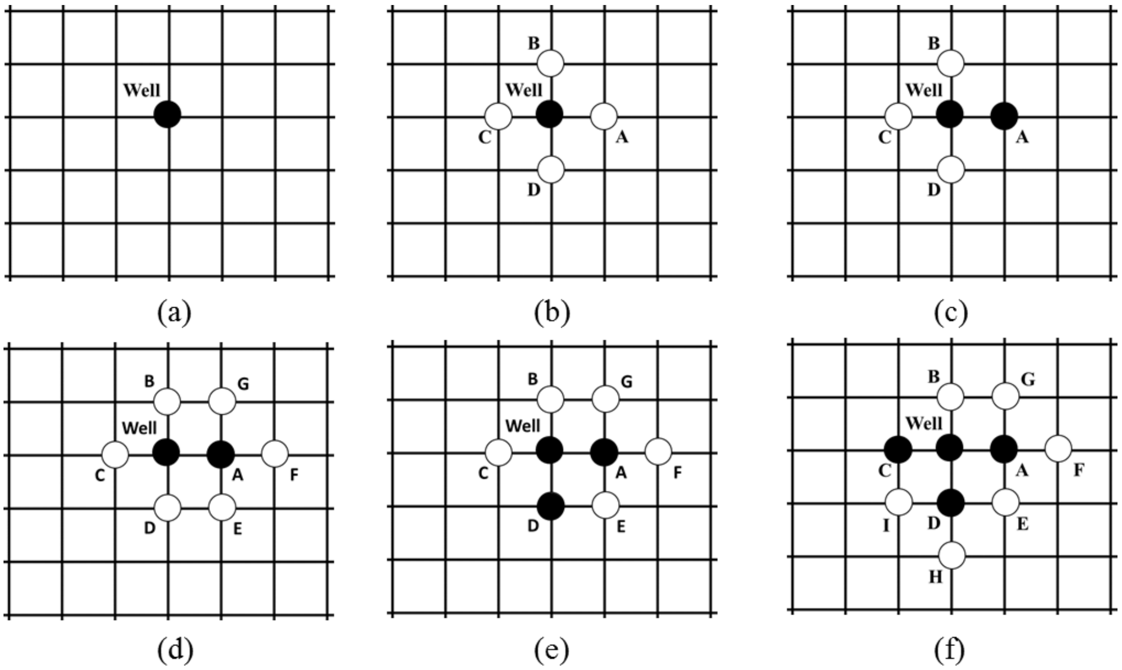

Figure 1.2 Procedures of FMM on 2D Cartesian grid (reprinted from Xie et al. 2015a)

We discretize the Eikonal Eq. (1.2) on the 2D Cartesian grid as (Xie et al. 2015a):

$$\max\left(D_{ij}^{-x}\tau, -D_{ij}^{+x}\tau, 0\right)^2 + \max\left(D_{ij}^{-y}\tau, -D_{ij}^{+y}\tau, 0\right)^2 = \frac{1}{\alpha} \tag{1.4}$$

where D denotes the first-order upwind finite difference operator. In the x-direction, D operator can be expressed as $D_{ij}^{-x}\tau = (\tau_{i,j} - \tau_{i-1,j}) / \Delta x$ and $D_{ij}^{+x}\tau = (\tau_{i+1,j} - \tau_{i,j}) / \Delta x$ while in the y direction $D_{ij}^{-y}\tau = (\tau_{i,j} - \tau_{i,j-1}) / \Delta y$ and $D_{ij}^{+y}\tau = (\tau_{i,j+1} - \tau_{i,j}) / \Delta y$. The final form is a quadratic equation for unknown τ(x), which can be solved very efficiently. The computation complexity of the FMM is $O(N \log N)$, which is same as the Dijkstra's algorithm.

1.2.2 FMM-based Reservoir Simulation

The FMM has already been applied in many disciplines, such as computational geometry, fluid mechanics, computer vision, and materials science. Our main contribution is to apply the FMM to petroleum related problems. The Eikonal equation governs the pressure front propagation and the DTOF serves as the footprint of the pressure front. By summing up the reservoir pore volume within each DTOF contour, we can calculate the transient drainage volume as a function of DTOF. Using the FMM, we can easily visualize the drainage volume evolution without solving the 3D fluid flow equations. Furthermore, analogous to the radius of investigation in homogeneous reservoirs, the DTOF can be used as a spatial coordinate to transform the 3-D model into an equivalent 1-D model. The so-called FMM-based reservoir simulation can achieve orders of magnitude faster computation than the traditional finite difference simulation and has been used in multiple field examples from history matching to EOR optimization (Zhang et al. 2016; Iino et al. 2017; Iino and Datta-Gupta 2018).

The first attempt of the FMM-based reservoir simulation was done by Xie et al. (2015a) and Xie et al. (2015b). In their work, they first calculated the drainage volume as a function of DTOF. Using the relationship between DTOF and the physical time, they generated the correlation between the drainage volume and the physical time. Finally, they used a pseudo-steady state solution to calculate the pressure within the drainage volume. This method is accurate in homogeneous reservoirs where the relationship between the DTOF and the physical time is well-known under different flow regimes. However, under heterogeneous conditions, the relationship is not rigorously defined, which makes the geometric pressure solution deviate from the real solution.

To generalize the geometric pressure solution, Zhang et al. (2016) first proposed to use the DTOF as a spatial coordinate to reduce the model and equations from 3D to 1D. Figure 1.3 illustrates the radius of investigation in homogeneous reservoir, the DTOF in heterogeneous reservoir, as well as the diffusivity equations. Again, we clearly see the analog between the radius of investigation in a homogeneous reservoir and the DTOF in a heterogeneous reservoir. By introducing the w(τ) function and assuming the pressure gradients are aligned with the τ(x) gradients, the 3D diffusivity equation can be simplified to 1D equation as (Zhang et al. 2016):

$$\frac{\partial p(\tau,t)}{\partial t} - \frac{1}{w(\tau)}\frac{\partial}{\partial \tau}\left(w(\tau)\frac{\partial p(\tau,t)}{\partial \tau} \right) = 0 \tag{1.5}$$

where the w(τ) function is the first derivative of the drainage volume V_p with respect to the DTOF.

$$w(\tau) = \frac{dV_p(\tau)}{d\tau} \tag{1.6}$$

The original work by Zhang et al. (2016) also provided detailed steps on the fluid flow equation transformation from 3D to 1D. The final form of the single-phase flow in the DTOF coordinate can be expressed as:

$$\frac{\partial(\phi\rho)}{\partial t} = \frac{\phi_{init}}{w(\tau)}\frac{\partial}{\partial \tau}\left(w(\tau)\rho\frac{(\mu c_t)_{init}}{\mu}\frac{\partial p}{\partial \tau} \right) + \rho q \tag{1.7}$$

where ϕ is porosity, ρ is fluid density, μ is fluid viscosity, q is the sink/source term. By solving Eq. (1.7) in the DTOF coordinate, we can calculate the well and reservoir responses.

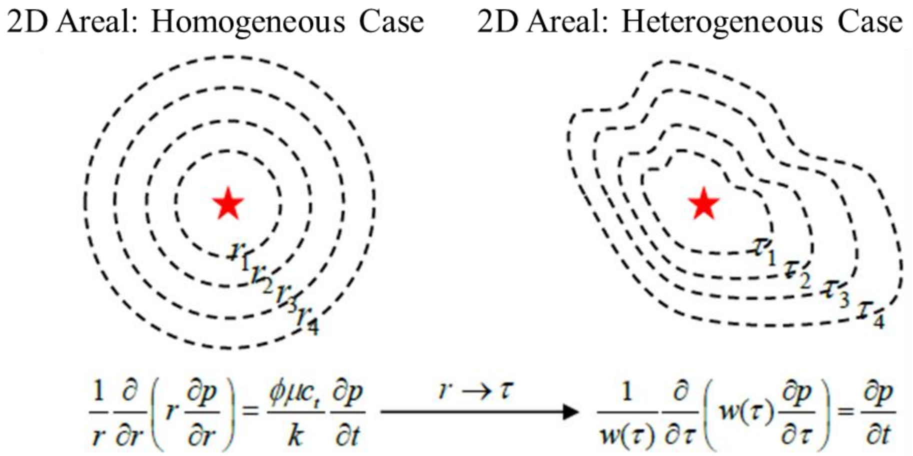

Figure 1.3 Analogy between the w(τ) formulation in heterogeneous reservoirs and the circular drainage volume in a homogeneous reservoir (reprinted from Zhang et al. 2016)

The FMM-based reservoir simulation workflow has already been extended to simulate complex physics in shale reservoirs. Fujita et al. (2016) first extended the FMM-based reservoir simulation workflow to a triple-continuum system. In this study, the DTOF were only calculated at the fracture system. Then the entire system was transformed to 1D with the nanopore and organic matter acting as the sink/source term. They also took into account multiple mass transfer processes such as the gas diffusion between the organic matter and nanopore and the Knudsen diffusion between the nanopore and fractures.

Iino et al. (2017) further extended the FMM-based reservoir simulation workflow to multiphase and multicomponent simulation. In this study, they validated the FMM-based workflow using multiple examples and performed a field-level history matching. This study demonstrated that the FMM-based reservoir simulation workflow can achieve the computation speed orders of magnitude faster while maintain the accuracy. In a later study, Iino and Datta-Gupta (2018) used the similar workflow for another application, the gas injection EOR optimization.

Some other contributions to the FMM-based reservoir simulation including Zhang and Zhu (2017) applied it to the temperature modeling and field level history matching using distributed temperature data. Yang et al. (2017) extended the FMM-based reservoir simulation workflow to unstructured grid system to simulate arbitrary fracture geometry. King et al. (2016) developed multiple analytical solutions based on the asymptotic solution and DTOF and compared them with numerous classical analytical solutions.

1.3 Dissertation Outline

In this dissertation, our focus is to utilize and extend the asymptotic solution to the diffusivity equation and FMM-based simulation to understand and characterize the complex fracture networks. First, we develop novel diagnostic plots for complex fracture networks characterization based on the asymptotic solution of the diffusivity equation. Then, we extend the FMM-based simulation to LGRs and EDFM to increase the computation efficiency and simulate the complex fracture networks. Finally, we apply the commercial fracture propagation simulator Mangrove® to a real field injection treatment pressure history matching to understand the impact of tighter cluster spacing on the geometry of fractures. The primary goals for each chapters are as follows:

In Chapter I, we introduce the background information and review the literature on the Fast Marching Method and FMM-based reservoir simulation.

In Chapter II, we develop the novel diagnostic plots for complex fracture networks characterization based on the asymptotic approach of the diffusivity equation. The w(τ) function serves as a diagnostic plot to detect the fracture geometry and flow regimes and the IRR plot is used to detect the fracture conductivity. We use multiple synthetic and field examples to validate the feasibility of the novel diagnostic plots.

In Chapter III, we extend the FMM-based simulation to LGRs using a novel gridding. We validate the accuracy and efficiency of the FMM-based simulation with LGRs using multiple examples. We investigate various discretization schemes for the transition between local and global domain in the FMM-based flow simulation.

In Chapter IV, we extend the FMM-based simulation to EDFM to simulate the complex fracture networks. We utilize a novel gridding to link the embedded discrete fractures and the matrix based on Delaunay triangulation. Multiple examples are shown to validate the accuracy and computational efficiency of this workflow.

In Chapter V, we investigate the impact of tighter cluster spacing on the hydraulic fractures using the Eagle Ford field data. The hydraulic fracture propagation simulator Mangrove® is used to generate the fracture patterns based on the completion data and injection treatment pressure. The impact of cluster spacing is examined through the calibrated fracture geometry and properties.

In Chapter VI, we make the conclusions of this dissertation and recommendations for future work.

CHAPTER II

RESERVOIR AND FRACTURE FLOW CHARACTERIZATION USING NOVEL DIAGNOSTIC PLOTS[*]

2.1 Chapter Summary

Multistage hydraulically fractured horizontal wells provide an effective means to exploit unconventional reservoirs. The current industry practice in the interpretation of field response often utilizes empirical decline curve analysis or pressure/rate transient analysis (PTA/RTA) for characterization of these reservoirs and fractures. These analytical tools are based on simplifying assumptions and do not provide a detailed description of the evolving reservoir drainage volume accessed from a well. The understanding of the transient drainage volume is essential for unconventional reservoir and fracture assessment and optimization.

In our previous study (Yang et al. 2015; Yang et al. 2016), we developed a "data-driven" methodology for the production rate and pressure analysis of shale gas and shale oil reservoirs. There are no underlying assumptions of fracture geometry, reservoir

---

[*] Part of this chapter is reprinted with permission from "Reservoir and Fracture Flow Characterization Using Novel Diagnostic Plots" by Xue et al. (2018), paper published in SPE Journal Preprint. Copyright [2018] Society of Petroleum Engineers.

[*] Part of this chapter is reprinted with permission from "Reservoir and Fracture Flow Characterization Using a Novel w(τ) Formulation" by Xue et al. (2016), paper URTEC-2440083-MS presented at the Unconventional Resources Technology Conference, 1-3 Aug., San Antonio, Texas, USA. Copyright [2016] URTEC.

homogeneity as well as flow regimes in the proposed method. This approach is based on the high frequency asymptotic solution of the diffusivity equation in heterogeneous reservoirs. It allows us to determine the well drainage volume, and the instantaneous recovery ratio (IRR), which is the ratio of the produced volume to the drainage volume, directly from the production data. In addition, a new $w(\tau)$ plot has been proposed to provide better insight into the depletion mechanisms and the fracture geometry.

In this chapter, we build upon our previous approach to propose a novel diagnostic tool for the interpretation of the characteristics of (potentially) complex fracture systems and drainage volume. We have utilized the $w(\tau)$ and IRR plots for the identification of characteristic signatures that imply complex fracture geometry, formation linear flow, partial reservoir completions, fracture interference and compaction effects during production. The $w(\tau)$ analysis gives us the fracture surface area and formation diffusivity whereas the IRR analysis provides additional information on fracture conductivity. Also, quantitative analysis is conducted using the novel $w(\tau)$ plot to interpret fracture interference time, formation permeability, total fracture surface area and stimulated reservoir volume (SRV).

The major advantages of this current approach are the model free analysis without assuming planar fractures, homogeneous formation properties, and specific flow regimes. In addition, the $w(\tau)$ plot captures high resolution flow patterns not observed in traditional PTA/RTA analysis. The analysis leads to a simple and intuitive understanding of the transient drainage volume and fracture conductivity. The results of the analysis are useful for hydraulic fracturing design optimization and matrix and fracture parameter estimation.

2.2 Background

Unconventional reservoirs such as shale oil and shale gas play a significant role in the US and the world energy market (Holditch 2013). For these low permeability reservoirs, long horizontal wells with multistage hydraulic fracturing have been proven to be an effective way to stimulate the formation in most cases. However, due to large uncertainty in fracture complexity and reservoir heterogeneity, the characterization of the fracture systems and the prediction of well performance are always of paramount interest.

Various analytical techniques are routinely applied to fracture characterization and well performance predictions. Most common amongst these are the decline curve analysis (Fetkovich 1980; Valko 2009; Lee and Sidle 2010) and PTA/RTA (Ilk et al. 2010; Song and Ehlig-Economides 2011). These analytical tools are based on simplified fracture and flow geometry and homogeneous reservoirs and thus, cannot properly characterize the evolution of the reservoir drainage volume from a well. Several recent studies focus on using numerical reservoir simulators to account for reservoir heterogeneity, complex fracture geometries, geomechanical effects and many other relevant physical processes (Cipolla et al. 2010a; Du et al. 2015; Sun and Schechter 2015; An et al. 2016). The disadvantage of this approach is the need for detailed well and reservoir models and the cost for the entire process, especially when high levels of grid refinement are used.

This chapter is organized as follows. We begin with a discussion of the methodology, including the $w(\tau)$ formulation and how to calculate the transient drainage volume, IRR and $w(\tau)$ from the production data. Next, we will use a single fracture example to explain how the $w(\tau)$ plot works as a diagnostic tool. Then we will use a variety of examples using horizontal well with multistage fractures to demonstrate the power and utility of the w(τ) plot compared to traditional RTA. Whereas w(τ) plot provides insights into the fracture complexity and fracture surface area, the IRR plot will be used as a supplementary plot for fracture conductivity comparison. Finally, we provide quantitative analysis using w(τ) plot to interpret fracture interference time, formation permeability, total fracture surface area and SRV. This will be followed by a field application, discussion and conclusions.

2.3 Methodology

Our previous studies have demonstrated the power and utility of the asymptotic analysis of the diffusivity equation for performance analysis of unconventional reservoirs. The asymptotic analysis leads to the Eikonal equation that describes the evolution of the drainage volume accounting for reservoir heterogeneity and complex fracture geometry. Using numerical solution of the Eikonal equation, we have also developed a comprehensive shale gas reservoir simulator for reservoir performance prediction (Fujita et al. 2016; Zhang et al. 2016). Instead, here we are focusing on calculating the well drainage volume, w(τ) and IRR directly from the well production data without resorting to geologic modeling and flow simulation. One common feature for both numerical and the current approach is the w(τ) function, which indicates how fast the drainage volume increases spatially. This w(τ) function can be used as a diagnostic plot and gives us more insight into reservoir and fracture flow geometry compared to the traditional PTA/RTA.

In this section, we will first review the w(τ) formulation and our methodology of calculating the drainage volume, w(τ) and IRR directly from the well production data.

2.3.1 Diffusivity Equation and the w(τ) Formulation

The detailed derivation of the asymptotic solution to the diffusivity equation in heterogeneous porous media is given by King et al. (2016) and Zhang et al. (2016). For a slightly compressible system, the diffusivity equation describing pressure transients in heterogeneous porous media can be expressed as:

$$\phi\left(x\right)\mu c_t\frac{\partial p(x,t)}{\partial t}-\nabla\cdot\left(k(x)\cdot\nabla p(x,t)\right)=0 \tag{2.1}$$

We may reduce the 3-D diffusivity equation, Eq. (2.1), to an equivalent 1-D diffusivity equation if we assume that the pressure gradients are aligned with the gradients, that is: $p(x,t)\approx p(\tau(x),t)$ and integrate the diffusivity equation along a streamtube from the well into the reservoir up to a τ contour, as shown in Figure 2.1.

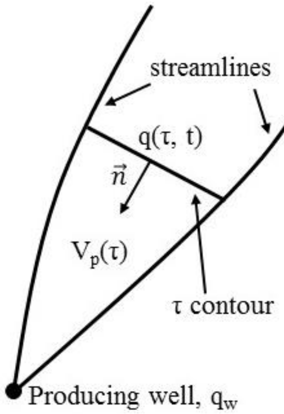

Figure 2.1 Streamtube originating from a producing well (reprinted from King et al. 2016)

The average pressure in the streamtube up to the τ contour is given by:

$$c_t V_p(\tau)\frac{\partial \overline{p}(\tau,t)}{\partial t} = -q_w + q(\tau,t) \tag{2.2}$$

If we consider a thin volume near the τ contour and integrate the diffusivity equation, Eq. (2.2) can be written as:

$$c_t \frac{\partial p(\tau,t)}{\partial t} = \frac{\partial q(\tau,t)}{\partial V_p(\tau)} = \frac{1}{w(\tau)}\frac{\partial q(\tau,t)}{\partial \tau} \tag{2.3}$$

where

$$w(\tau) = \frac{dV_p(\tau)}{d\tau} \tag{2.4}$$

The inwardly directed normal area is related to the gradient of the pore volume, as shown in Figure 2.1. The inwardly directed flux can then be written as:

$$q(\tau,t) = \vec{n}\cdot\vec{u} = \left(\frac{1}{\varphi}\frac{dV_p(\tau)}{d\tau}\nabla\tau\right)\bullet\left(\frac{1}{\mu}k\nabla\tau\frac{\partial p}{\partial t}\right) = c_t w(\tau)\frac{\partial p}{\partial \tau} \tag{2.5}$$

From Figure 2.1 and Eq. (2.5) we can clearly see that the w(τ) function is proportional to the cross-sectional area of the streamtube and is directly related to pore volume within the streamtube. Now we can substitute the flux equation into Eq. (2.3) to complete the derivation of the equivalent 1-D diffusivity equation.

$$\frac{\partial p(\tau,t)}{\partial t} - \frac{1}{w(\tau)}\frac{\partial}{\partial \tau}\left(w(\tau)\frac{\partial p(\tau,t)}{\partial \tau}\right) = 0 \tag{2.6}$$

As can be seen from Eq. (2.6), the spatial heterogeneity of the porosity and permeability has vanished from the diffusivity equation after using the w(τ) function.

2.3.2 Asymptotic Solutions to the Diffusivity Equation

We may obtain another form of the diffusivity equation in terms of the flux only (King et al. 2016).

$$\frac{\partial q(\tau,t)}{\partial t} - w(\tau)\frac{\partial}{\partial \tau}\left(\frac{1}{w(\tau)}\frac{\partial q(\tau,t)}{\partial \tau}\right) = 0 \tag{2.7}$$

To solve the diffusivity equation above, we need one initial condition and two boundary conditions. For a fixed rate drawdown in an infinite domain, these conditions are summarized in Table 2.1. The flux boundary condition at the wellbore is specified at $\tau=0$. This maybe a distance of $r=r_w$ for a finite wellbore radius and for the line source approximation as $r_w \to 0$.

Table 2.1 Initial and boundary conditions for the diffusivity equation for an infinite domain (reprinted with permission from Xue et al. 2016)

	$\tau(x)$	$p(\tau,t)$	$q(\tau,t)$
Initial: $t=0$	-	$p=p_i$	$q=0$
Wellbore: $r=r_w$	$\tau=0$	$c_t w(\tau)\frac{\partial p}{\partial \tau}=q_w$	$q=q_w$
Far Field: $\tau\to\infty$	-	$p\to p_i$	$q\to 0$

For the case of simple geometries in the line source approximation, $w(\tau)$ scales as a power law in τ such as $w(\tau) \sim \tau^n$ and $n \geq 0$. This captures all of the classical flow regimes in textbooks as well as the more interesting case of the diffusion on fractal geometry for a fractured reservoir (Barker 1988; John et al. 2003). A dimensional analysis shows that the flux may depend only on the dimensionless Boltzmann ratio of τ and t.

$$\xi = \frac{\tau^2}{4t} \tag{2.8}$$

Based on the Boltzmann variable, we may relate t and τ derivatives of the flux to simplify Eq. (2.7).

$$\frac{\partial q}{\partial \tau} = \frac{\tau}{2t}\frac{dq}{d\xi} \text{ and } \frac{\partial q}{\partial t} = -\frac{\tau^2}{4t^2}\frac{dq}{d\xi} = -\frac{\tau}{2t}\frac{\partial q}{\partial \tau} \tag{2.9}$$

After substituting Eq. (2.9) into Eq. (2.7), the equation can be written as:

$$\left(\frac{1}{w(\tau)}\frac{\partial q(\tau,t)}{\partial \tau}\right)^{-1}\frac{\partial}{\partial \tau}\left(\frac{1}{w(\tau)}\frac{\partial q(\tau,t)}{\partial \tau}\right) = -\frac{\tau}{2t} \tag{2.10}$$

This equation may be integrated explicitly:

$$\frac{1}{w(\tau)}\frac{\partial q(\tau,t)}{\partial \tau} = -\frac{q_w}{V_d(t)}e^{-\frac{\tau^2}{4t}} \tag{2.11}$$

This leads to the following expression for the pressure transient:

$$c_t\frac{\partial \Delta p(\tau,t)}{\partial t} = -\frac{1}{w(\tau)}\frac{\partial q(\tau,t)}{\partial \tau} = \frac{q_w}{V_d(t)}e^{-\frac{\tau^2}{4t}} \tag{2.12}$$

The flux solution can be obtained by an additional integration from a location in the reservoir to the far field boundary where q→0 as τ→∞.

$$q(\tau,t) = \frac{q_w}{V_d(t)}\int_{\tau'=\tau}^{\infty} d\tau'\cdot w(\tau')e^{-\frac{\tau'^2}{4t}} = \frac{q_w}{V_d(t)}\int_{\tau'=\tau}^{\infty} dV_p(\tau')e^{-\frac{\tau'^2}{4t}} \tag{2.13}$$

The drainage volume $V_d(t)$ can be determined from the boundary condition at τ=0.

$$V_d\left(t\right)=\int_0^\infty d\tau\cdot w\left(\tau\right)e^{-\frac{\tau^2}{4t}}=\int_0^\infty dV_p\left(\tau\right)e^{-\frac{\tau^2}{4t}} \qquad (2.14)$$

Eq. (2.14) is taken as the starting point of our drainage volume analysis for the general case of arbitrary w(τ).

2.3.3 Drainage Volume, IRR and w(τ) Calculation

Before calculating the drainage volume and Instantaneous Recovery Ratio (IRR) from the production data, let's first examine the qualitative aspects of this solution for the fixed rate draw down, as summarized in Figure 2.2 and Table 2.2. The Boltzmann variable, $\xi=\frac{\tau^2}{4t}$, controls the solution characteristics for both homogeneous and heterogeneous reservoirs and in arbitrary dimensions. Let's describe the characteristics of the solution, starting from the left of Figure 2.2 and the top of Table 2.2. For sufficiently small values, $\frac{\tau^2}{4t}<0.01$ then $\exp(-\frac{\tau^2}{4t})\approx 1$, and $\frac{\partial p}{\partial t}$ is independent of position. This is the pseudo steady state (PSS) solution. For values of $0.1<\frac{\tau^2}{4t}<4$ then $0.018<\exp(-\frac{\tau^2}{4t})<0.9$, and $\frac{\partial p}{\partial t}$ depends upon both τ and t and we have a clear pressure transient solution. Once we have sufficiently large values, $\frac{\tau^2}{4t}>4$ then $\exp(-\frac{\tau^2}{4t})<0.018$, which is essentially at initial conditions. Since we are in PSS near the well, we may define the drainage volume from production data, following the analysis of (Matthews et al. 1954). However, for the unconventional reservoirs we have examined, we have not seen the evidence of reaching the PSS limit corresponding to boundary dominated flow but instead stay in the transient region. Therefore, the drainage volume $V_d(t)$ provides a dynamic measure of how much of the reservoir pore volume has begun depletion.

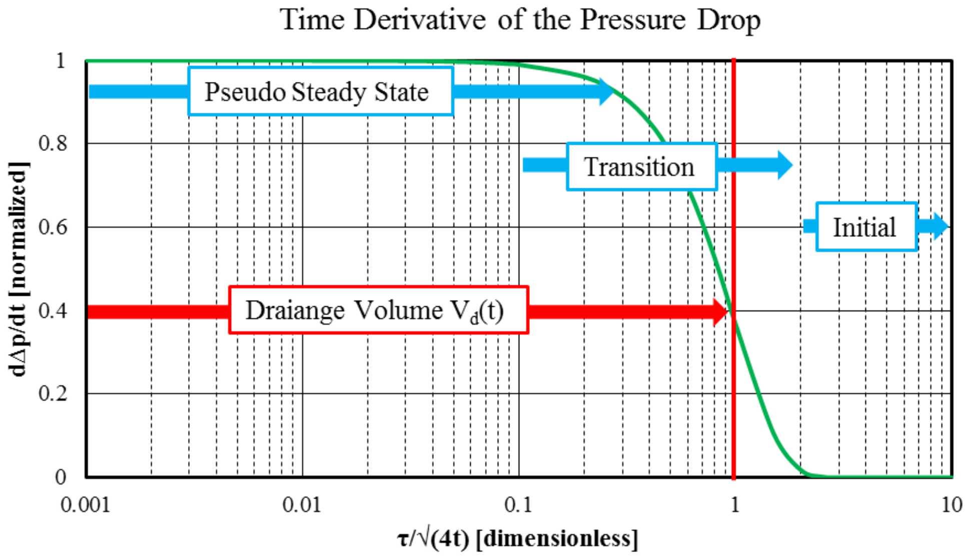

Figure 2.2 Spatial profile of the fixed rate draw-down solution to the asymptotic pressure approximation in terms of the time derivative of the pressure drop, normalized to its value at the well (τ=0) (reprinted from King et al. 2016)

Table 2.2 Characteristics of the asymptotic pressure solution for the fixed rate draw-down (reprinted with permission from Xue et al. 2016)

Solution	Exponential Range	Boltzmann Variable
Pseudo Steady State (PSS)	$\exp\left(-\frac{\tau^2}{4t}\right) > 0.99$	$\frac{\tau^2}{4t} < 0.01$
Approximate PSS	$0.9 < \exp\left(-\frac{\tau^2}{4t}\right) < 0.99$	$0.01 < \frac{\tau^2}{4t} < 0.1$
Transient	$0.018 < \exp\left(-\frac{\tau^2}{4t}\right) < 0.9$	$0.1 < \frac{\tau^2}{4t} < 4$
Near Initial	$\exp\left(-\frac{\tau^2}{4t}\right) < 0.018$	$\frac{\tau^2}{4t} > 4$

For the cases of simple geometry, we can directly determine τ, $V_p(\tau)$ and $w(\tau)$ from an analytical solution. For pressure transient analysis, we may directly determine the welltest derivative, $\Delta p'_{wf}$, defined as the logarithmic time derivative of the pressure drop at the wellbore (Bourdet et al. 1983). We can simply relate the drainage volume to the welltest derivative using Eq. (2.12).

$$\Delta p'_{wf}(t) = \frac{d\Delta p_{wf}}{d\ln t} = \frac{q_w t}{c_t V_d(t)} e^{-\frac{\tau_w^2}{4t}} = \frac{q_w t}{c_t V_d(t)} \tag{2.15}$$

This equation is extremely useful as we can directly calculate the welltest derivative in terms of the drainage volume and do not need to first solve for the pressure drop. If we do not have the reservoir and well model, we cannot determine τ, $V_p(\tau)$ and $w(\tau)$ directly. Instead, we can calculate the drainage volume using the pressure and rate data.

$$\frac{d\Delta p_{wf}}{dt} = \frac{q_w}{c_t V_d(t)} e^{-\frac{\tau_w^2}{4t}} = \frac{q_w}{c_t V_d(t)} \tag{2.16}$$

For unconventional reservoirs, following Winestock and Colpitts (1965), and Song and Ehlig-Economides (2011), we can use the rate normalized pressure (RNP) to calculate the drainage volume. This RNP approximation represents the production behavior that would be observed if the well were produced at a constant reference rate.

$$\frac{1}{V_d(t_e)} \approx c_t \frac{d}{dt_e}\left(\frac{\Delta p_{wf}(t_e)}{q_w(t_e)}\right) \tag{2.17}$$

where t_e is the material balance time defined as:

$$t_e = \frac{Q(t)}{q_w(t)} \tag{2.18}$$

To account for the reservoir depletion efficiency, we also defined the IRR function, which is the ratio of the cumulative production to the well drainage volume.

$$IRR(t_e) = \frac{Q(t_e)}{V_d(t_e)} \tag{2.19}$$

The drainage volume $V_d(t)$ and $w(\tau)$ can be related through Eq. (2.14). Considering $\exp(-\frac{\tau^2}{4t})$ as the kernel function, the above integral is a Fredholm integral of the first kind, and $w(\tau)$ is the function we are trying to determine. We invert for the $w(\tau)$ function using a piecewise constant representation. In Appendix A, we provide a detailed methodology to invert the $w(\tau)$ function from the drainage volume $V_d(t)$. Given pressure and rate data, the procedure involves: (a) converting given pressure to bottom hole pressure if the measured pressure is tubing head pressure or casing pressure (b) using Eq. (2.17) to calculate the drainage volume $V_d(t)$ (c) using Eq. (2.19) to calculate the instantaneous recovery ratio (IRR) (d) using Eq. (2.14) to link the drainage volume $V_d(t)$ with $w(\tau)$ function using the methodology provided in the next section. Like traditional PTA/RTA, this analysis is limited to a single well. Multi-well analysis is beyond the scope of the current study.

2.4 Applications: Results and Discussion

2.4.1 w(τ) as a Diagnostic Plot: A Single Infinite Conductivity Fracture

We start our analysis by using a simple example, a vertical well with single infinite conductivity fracture. This example will demonstrate the detailed steps of our workflow and also provide the analytical solution for τ, $V_d(t)$ and w(τ), from which we will clearly see why w(τ) can be used as a flow diagnostic. We start with the analytical solution of τ, $V_d(t)$ and w(τ). The graphical solution with an illustrative pressure contour is shown in Figure 2.3. τ(x) can be calculated directly by using the path of the fastest pressure propagation back to the well location, where τ=0. Along the fracture plane, the fastest route is perpendicular to the fracture surface and $\tau = \mathrm{r}/\sqrt{\alpha}$. Outside the fracture plane, the fastest route is to the fracture tip and $\tau = \mathrm{r}/\sqrt{\alpha}$. The fastest routes r are shown in Figure 2.3. The resulting drainage volume is a combination of linear and radial flow.

$$\tau = r/\sqrt{\alpha} \tag{2.20}$$

$$V_d = (4x_f r + \pi r^2)h\phi \tag{2.21}$$

$$w(\tau) = \frac{dV_p(\tau)}{d\tau} = (4\sqrt{\alpha}x_f + 2\pi\alpha\tau)h\phi \tag{2.22}$$

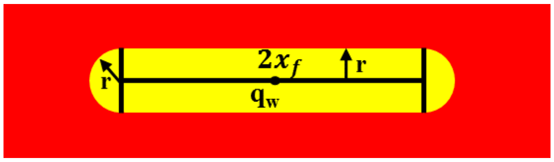

Figure 2.3 Graphical solution of τ, $V_d(t)$ and w(τ) for a single infinite conductivity fracture (reprinted with permission from Xue et al. 2018)

Table 2.3 Parameters used in the single infinite conductivity fracture example (reprinted with permission from Xue et al. 2018)

Parameter	Value
Reservoir size	2408×2400×100 ft^3
Initial pressure	5470 psi
Matrix porosity	0.046
Matrix permeability	0.0005 md
Hydraulic fracture porosity	0.3
Hydraulic fracture permeability	1000 md
Hydraulic fracture half-length	400 ft
Oil viscosity	0.2 cp
Oil compressibility	2.0×10^{-5} psi^{-1}
Formation volume factor	1.37 bbl/STB
Rock compressibility	1.0×10^{-5} psi^{-1}

To start with we demonstrate that RNP could give us a good approximation of drainage volume calculation for the fixed rate draw down solution discussed above. We construct a single infinite conductivity fracture numerical simulation model, which is shown in Figure 2.4. The fracture fully penetrates the reservoir height and a tartan grid is used in the direction perpendicular to the fracture surface. The parameters used in this example are given in Table 2.3. We simulate two cases: a constant bottomhole pressure constraint at 1000psi and a constant rate constraint at 2bbl/day respectively. A commercial reservoir simulator is used to simulate this synthetic case. Figure 2.5 shows the simulation results of the production rate under constant BHP constraint and BHP under constant rate constraint.

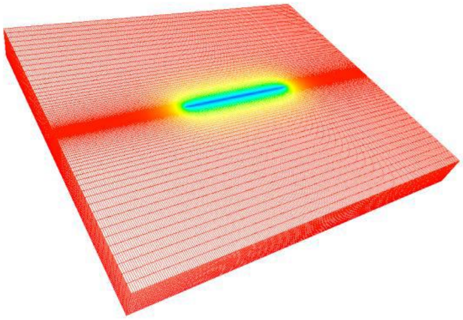

Figure 2.4 Single fracture on a tartan grid and its pressure distribution at 1000 days (reprinted with permission from Xue et al. 2018)

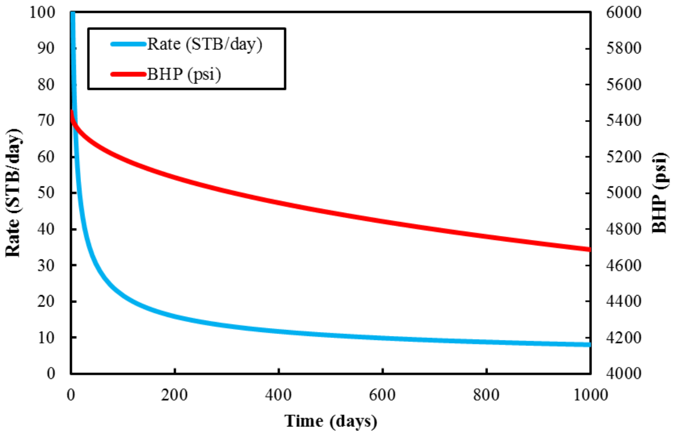

Figure 2.5 Production rate under BHP constraint and BHP under rate constraint for the single fracture model (reprinted with permission from Xue et al. 2018)

Our next step is to demonstrate RNP approximation could calculate similar drainage volume as the fixed rate draw down solution. In Figure 2.7(a), the drainage volume results obtained from the two methods are consistent with each other. Therefore, RNP is a reasonable approximation. The pressure contours at different flow regimes are given in Figure 2.6, followed by the $V_d(t)$, IRR and $w(\tau)$ results in Figure 2.7. In the following synthetic examples, constant BHP constraint with RNP approximation will be used.

The pressure contours in Figure 2.6 clearly illustrates linear flow at early time, followed by radial flow. At late time, it becomes boundary dominated PSS flow. From the analytical solution of w(τ) in Eq. (2.22), at the early time τ values are relatively small, $w(\tau)\approx 4\sqrt{\alpha}x_f h\phi = A\sqrt{\alpha}\phi$. Therefore in the w(τ) plot at early time, w(τ) is a constant, which indicates linear flow regimes. In addition, this early time w(τ) value is proportional to the fracture surface area. At intermediate time, the flow regime is dominated by radial flow, $w(\tau)\approx 2\pi\alpha\tau h\phi$. Therefore in the w(τ) plot at intermediate time, w(τ) increases linearly with τ having a unit slope. At late time the pressure front reaches the reservoir boundary and the drainage volume does not increase, which is boundary dominated PSS flow, and w(τ) approaches towards zero. The above analysis demonstrates w(τ) can be used as a diagnostic for flow regimes identification as well as for fracture surface area determination.

The IRR plot is drawn on semi-log axes to emphasize the early time behavior. The early time IRR value reaches a maximum when radial flow begins. Recall that IRR is the ratio of produced volume to drainage volume. The drainage volume increases slower than does the produced volume in the linear flow regime. On the contrary, in the radial flow regime, the drainage volume increases faster than does the produced volume. This phenomenon will also be seen in our multiple fracture cases. For late time boundary dominated PSS flow, the drainage volume no longer increases and the IRR will then increase monotonically with production.

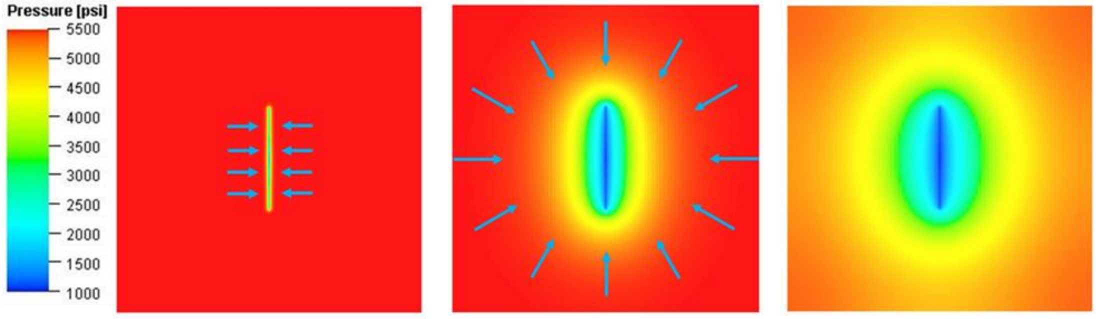

(a) (b) (c)

Figure 2.6 Pressure contours for single fracture model: (a) Early time linear flow (b) Intermediate time radial flow (c) Late time boundary dominated PSS flow (reprinted with permission from Xue et al. 2018)

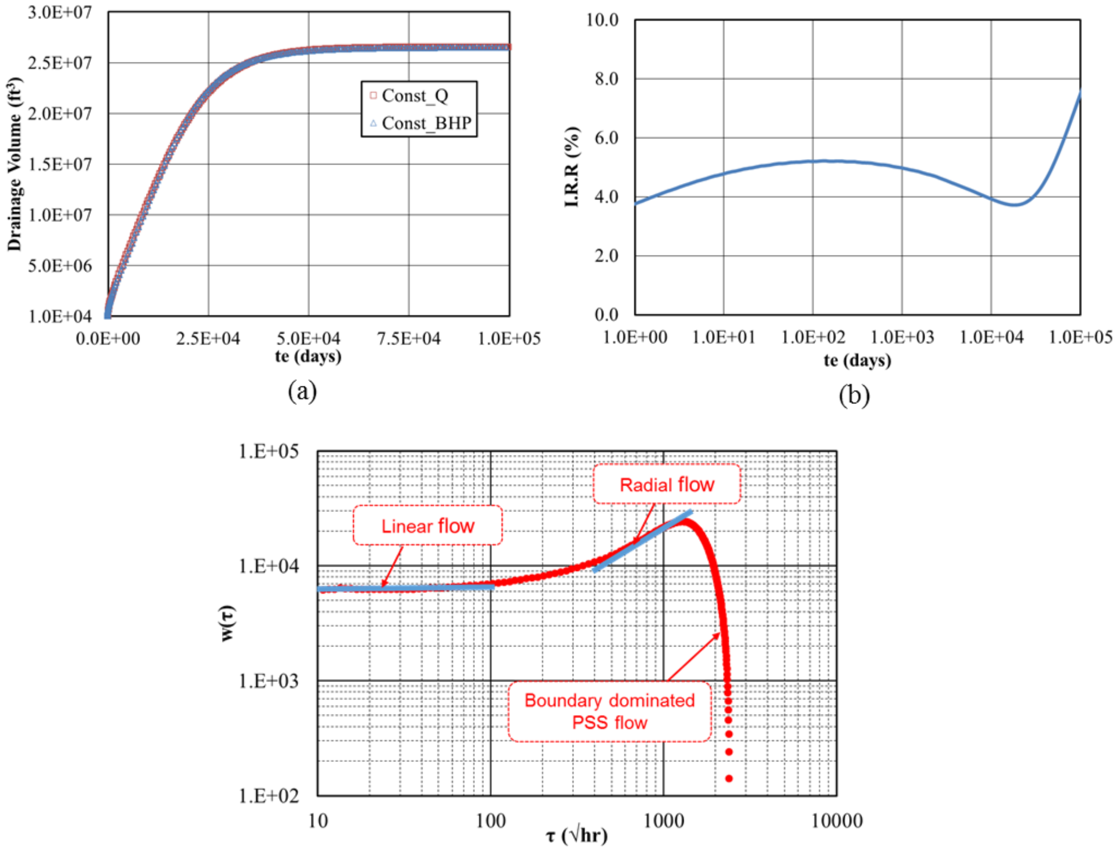

(a) (b)

(c)

Figure 2.7 Analysis results for single fracture model: (a) Drainage volume (b) IRR plot (c) w(τ) plot (reprinted with permission from Xue et al. 2018)

2.4.2 w(τ) as a Diagnostic Plot: Multiple Stage Fractures

We now focus on the application of our methodology to horizontal wells with multiple stages of fractures. For comparison purpose, the traditional rate-normalized pressure (RNP) diagnostic plot will also be shown here. Following Song and Ehlig-Economides (2011), we define RNP and RNP' as:

$$RNP = \frac{p_i - p_{wf}(t)}{q(t)} \tag{2.23}$$

$$RNP' = \frac{dRNP}{d \ln t_e} \tag{2.24}$$

where t_e is the material balance time defined in Eq. (2.18).

To construct the horizontal well with multiple stages of fractures, we first use a commercial fracture propagation simulator to generate the fractures. High resolution local PEBI grids are used to capture the complex fracture geometry and create the grid system. The reservoir with the complex fractures model is then simulated using a commercial finite volume reservoir simulator. The input parameters used for a typical shale reservoir are listed in Table 2.4 (Cipolla et al. 2010b). In Table 2.5, we show the fracture treatment data for the fracture propagation simulation. Unless otherwise noted, the parameters used in all the examples are identical. The fluid properties are the same as the single fracture case discussed above.

Table 2.4 Input parameters for typical shale reservoir (reprinted with permission from Xue et al. 2018)

Parameter	Value
Rock Type	Marcellus shale
Young's Modulus	3.88×106 psi
Poisson's Ratio	0.23
Min Horizontal Stress	5950 psi
Max Horizontal Stress	6250 psi
Overburden Stress	7705 psi
Matrix porosity	0.046
Matrix permeability	0.00005 md
Initial pressure	5000 psi
Unpropped Fracture Conductivity	0.3 mD.ft
Formation Grid Size	15×15×5 ft
Fracture Grid Size	0.5 ft

Table 2.5 Input parameters for fracturing treatment (reprinted with permission from Xue et al. 2018)

Parameter	Value
Injection Rate	60 bbl/min
Injection Fluid	Linear Gel or Slickwater
Fluid Volume	100000 gal
Proppant Concentration	3 ppa
Fluid Viscosity	Linear Gel 32 cP Slickwater 1.5 cP
Proppant Type	Jordan Unimin 30/50
Cluster Spacing	100 ft
No. of clusters per stage	4
No. of stage	3

We will begin our analysis with a simple example where the fractures fully penetrate the reservoir vertically. We will compare the traditional RNP diagnostic plot and w(τ) plot and again demonstrate that w(τ) plot can be used as a diagnostic. For this example, we know all the flow regimes and flow signatures, namely formation linear flow, fracture interference, radial flow and boundary dominated PSS flow. Since for the field applications we seldom see the radial flow and boundary dominated PSS flow, we will focus on the early time formation linear flow and fracture interference. Figure 2.8 gives the pressure contours at different flow regimes and Figure 2.9 shows the results of $V_d(t)$, IRR, $w(\tau)$, RNP and RNP'.

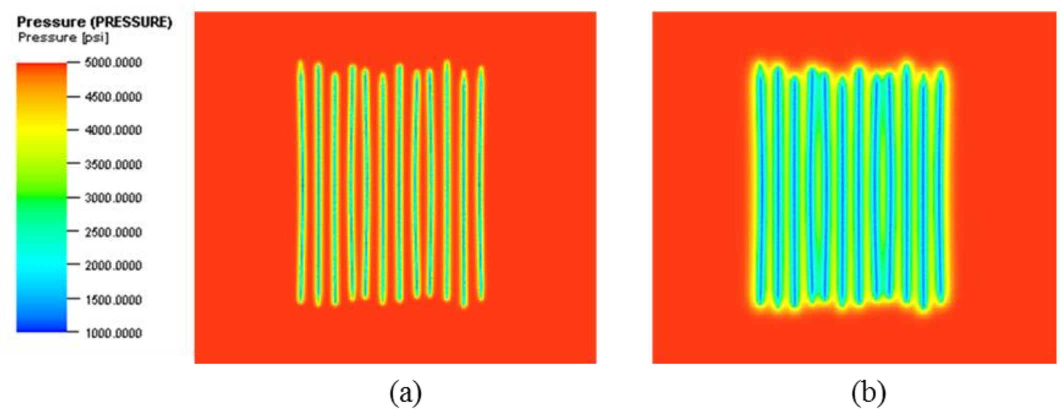

(a)

(b)

Figure 2.8 Pressure contours for full completion model: (a) Formation linear flow (b) Fracture interference (reprinted with permission from Xue et al. 2018)

The trend of the IRR plot is different from the single fracture case. At early time, IRR plot monotonically increases because we only have linear flow regime before fracture interference occurs. In the single fracture model, IRR decreases because the radial flow begins and the drainage volume increases more rapidly than does the produced volume. When fracture interference occurs, the drainage volume increases very slowly which causes the IRR plot to rapidly increase at late time.

Here we also compare the traditional RNP diagnostic plot with the $w(\tau)$ plot. First, at early time, we can see the ½ slope trend in the RNP derivative and the constant $w(\tau)$ value in the $w(\tau)$ plot, and both indicate the formation linear flow. At late time, the slope of the RNP derivative becomes unit slope, which is the signal of PSS flow. While in the w(τ) plot, the onset of fracture interference is indicated by w(τ) trends downward. Therefore, we can clearly identify each flow regimes in both RNP and w(τ) plot.

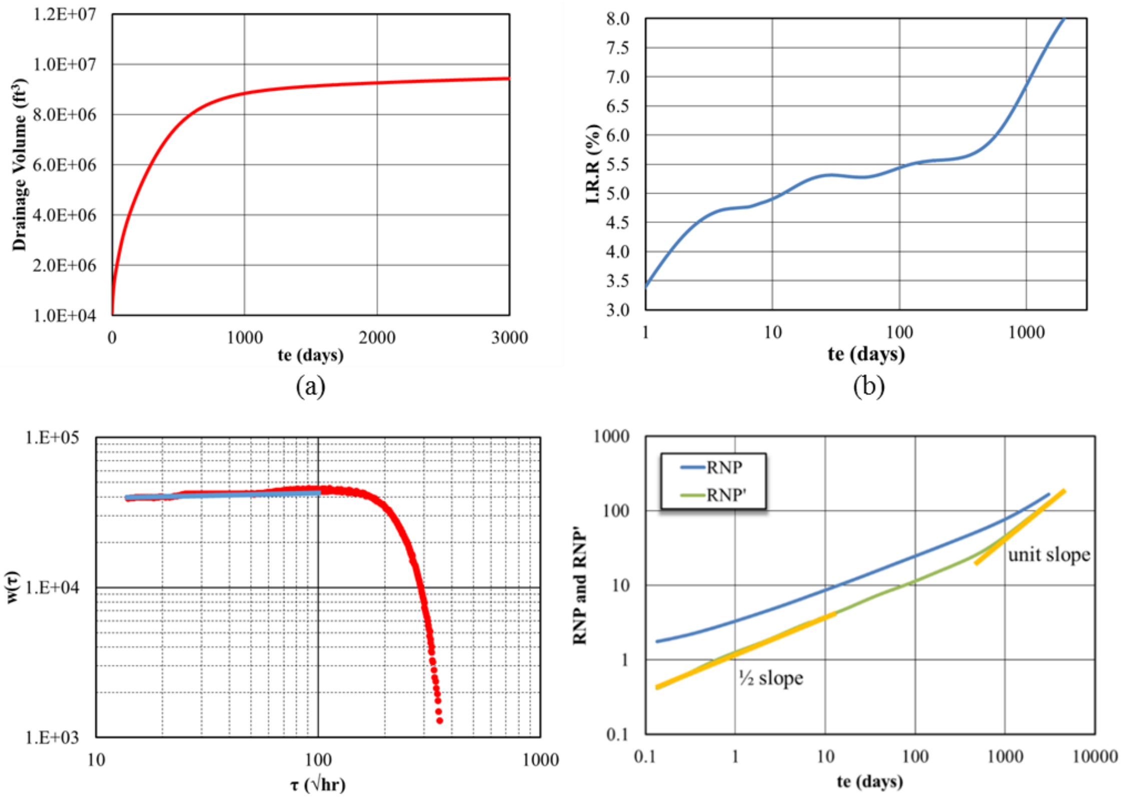

(a)

(b)

(c)

(d)

Figure 2.9 Analysis results for fully completed fracture model: (a) Drainage volume (b) IRR plot (c) w(τ) plot (d) RNP and RNP' plot (reprinted with permission from Xue et al. 2018)

In the second example, we show a complex case where the fractures only penetrate 50% of the reservoir in the vertical direction. During our fracture treatment process, fractures may initially penetrate the entire pay zone vertically. However, the proppant distribution is always non-uniform which may lead to the effective height of the fractures during production to be much smaller than fully completed. In order to reveal the flow regimes of this kind of fracture system, we show the pressure contours from the side view of the fracture plane in Figure 2.10. The pressure contour map shows the pressure front propagation, from which we can see the flow regimes. In Figure 2.11, we show the results of $V_d(t)$, IRR, $w(\tau)$, RNP and RNP'.

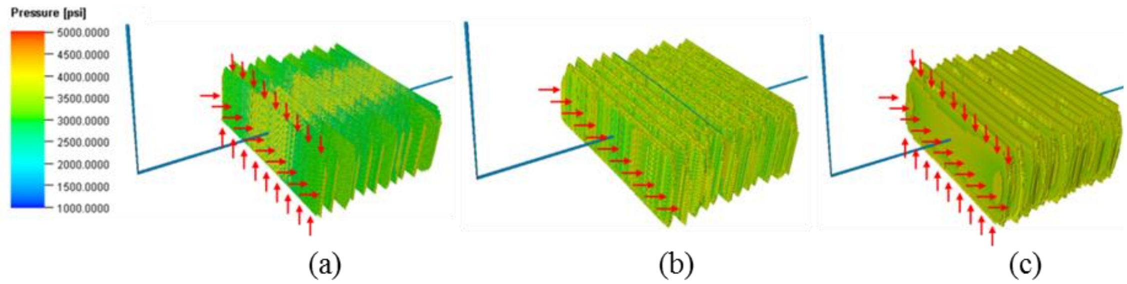

Figure 2.10 Pressure contours from the side view of the fracture plane (a) At 5 days: fracture flow (b) At 24 days: formation linear flow (c) At 253 days: partial completion (reprinted with permission from Xue et al. 2018)

Here we first compare the traditional RNP diagnostic plot with the $w(\tau)$ plot. The RNP diagnostic plot is almost identical with the case of full penetration. We can see from the RNP derivative, the ½ slope trend indicating the formation linear flow at early time and the unit slope trend indicating fracture interference at late time. However, the $w(\tau)$ plot changes significantly compared to the full penetration case. At early time, before the constant $w(\tau)$ is reached, there is an upward trend. This is because at early time, besides the linear flow perpendicular to the fracture surfaces, there is also some radial flow effect at the top and bottom edges of the fracture. This phenomenon can be seen in Figure 2.10 (a). We describe this behavior as fracture flow. After the fracture flow, the linear flow normal to the fracture surfaces becomes the dominant flow and $w(\tau)$ stays constant. This is the formation linear flow period. In the intermediate time $w(\tau)$ has an upward trend again. This is because the radial flow at the top and bottom of the fractures becomes significant again compared to the formation linear flow (see Figure 2.10 (c)). This flow regime is a combination of formation linear flow perpendicular to the fracture surfaces and radial flow at the top and bottom edges of the fractures. We describe this flow regime as partial completion effect. Finally, at late time, we can see the onset of fracture interference. Therefore, for partially completed multistage fractured horizontal well, the four flow regimes are fracture flow, formation linear flow, partial completion and fracture interference. Clearly, for this situation the $w(\tau)$ plot gives us more information than the traditional RNP plot. The trend of the IRR plot is also different from the full completion case. At intermediate time, IRR plot goes downward before fracture interference. This is because of the radial flow at the top and bottom edges of the fractures and hence, the drainage volume increases more rapidly than the produced volume.

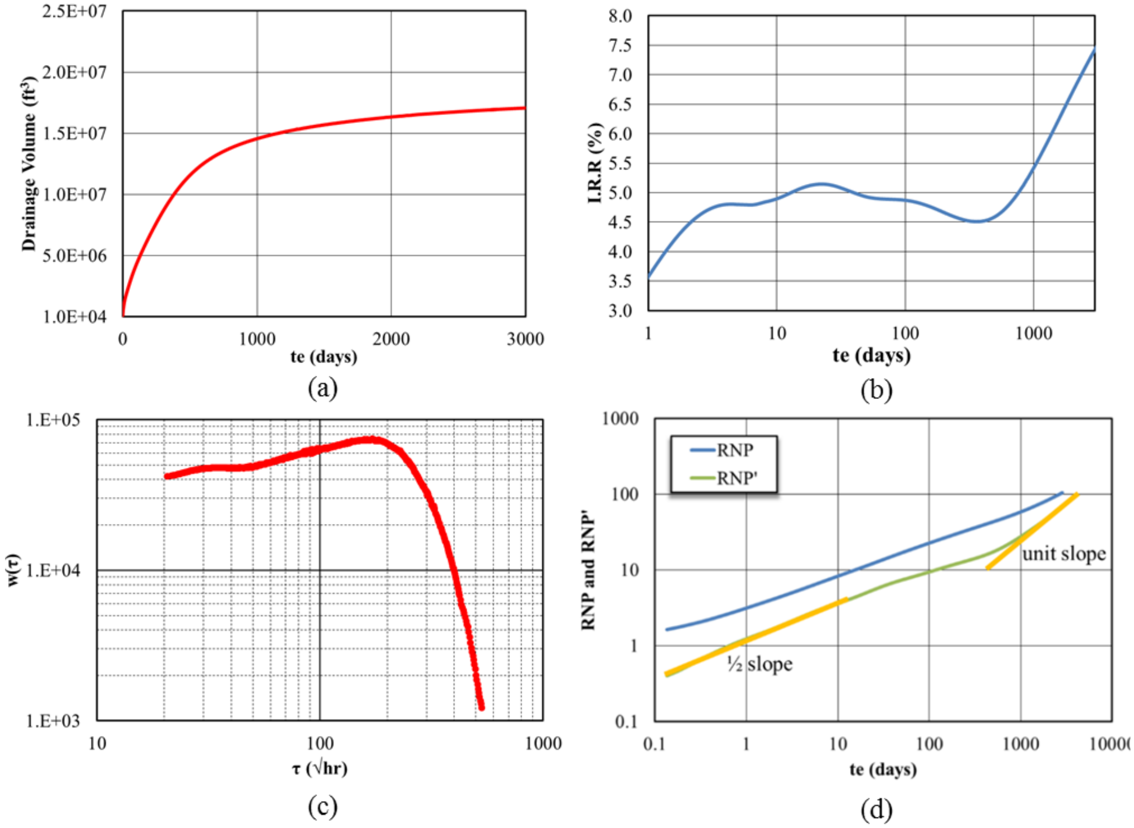

(a)

(b)

(c)

(d)

Figure 2.11 Analysis results for 50% partial completion model: (a) Drainage volume (b) IRR curve (c) w(τ) plot (d) RNP and RNP' plot (reprinted with permission from Xue et al. 2018)

We also conducted a sensitivity study to see the influence of different percentage of partial completion on $V_d(t)$, IRR and w(τ) plot, which is given in Figure 2.12. From the drainage volume calculations, we can see that with increasing percentage of partial completion, the drainage volume increases as well. This is reasonable because more radial flow happens at the top and bottom of the fractures. For the same reason, we can see larger downward trend in the IRR plot at intermediate time. Similarly in the w(τ) plot, we get larger upward trend. Above analysis demonstrates that w(τ) plot can be used as a diagnostic plot and can give us more detailed information about flow regimes than the traditional RNP plot.

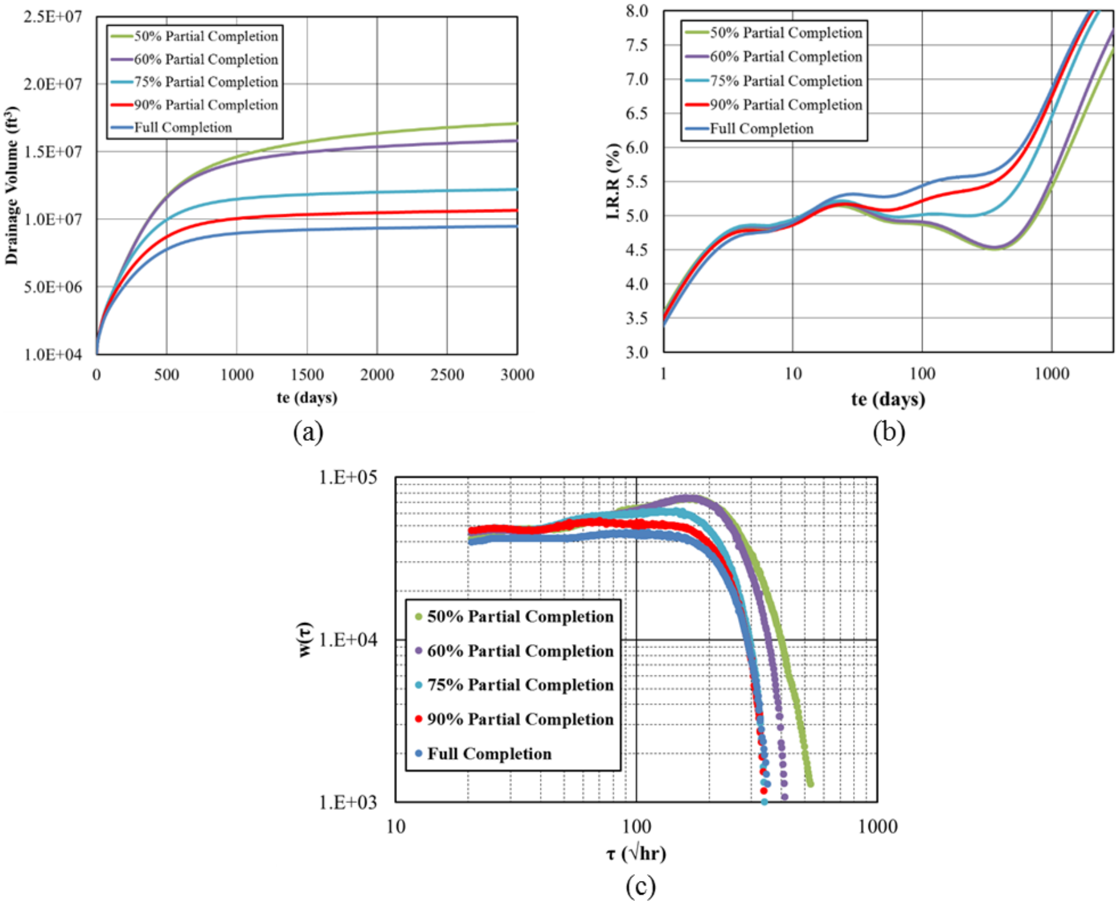

(a)

(b)

(c)

Figure 2.12 Sensitivity study of different percentage of partial completion (a) Drainage volume (b) IRR curve (c) w(τ) plot (reprinted with permission from Xue et al. 2018)

2.4.3 Characterization of Influential Parameters for w(τ) and IRR

We will now apply the w(τ) as a diagnostic plot to a series of examples. In these examples, we will see that w(τ) not only identifies the flow regimes but also gives us other information such as the fracture surface area in complex fracture system. In addition, IRR gives us information related to fracture conductivity and fracture compaction. During the fracturing treatment, because of the non-uniform distribution of the proppant, partial completion effects may exist. In our simulation, we choose to use 75% partial completion as the base case in which we can see some influence of partial completion on $w(\tau)$ and IRR, while exploring other sensitivities.

2.4.3.1 Impact of Fracture Surface Area

In order to show that the $w(\tau)$ plot can be used as an indicator of fracture surface area, we carry out a sensitivity study by changing the fracture half length. We use the fracturing treatment input listed in Table 2.5 as the base case and half the amount of the fracturing fluid (50000 gal) and the same proppant concentration (3 ppa) to generate a model with shorter fracture half-length and similar fracture conductivity. Figure 2.13 compares the pressure contours after 3 years of production and Figure 2.14 shows $V_d(t)$, IRR and $w(\tau)$ plot. As can be seen from the $w(\tau)$ plot, both long and short fractures cases have similar trend but long fracture case has obviously higher $w(\tau)$ value before fracture inference because of larger fracture surface area. This indicates that $w(\tau)$ value at early and intermediate time can be used as a signal for fracture surface area. As shown in the IRR plot, although the two cases have different drainage volume, IRR plots are almost identical, which reflects the influential parameter for the IRR plot is not fracture surface area. In the following section, we will see that the fracture conductivity and fracture compaction are the main influential parameters for the IRR plot.

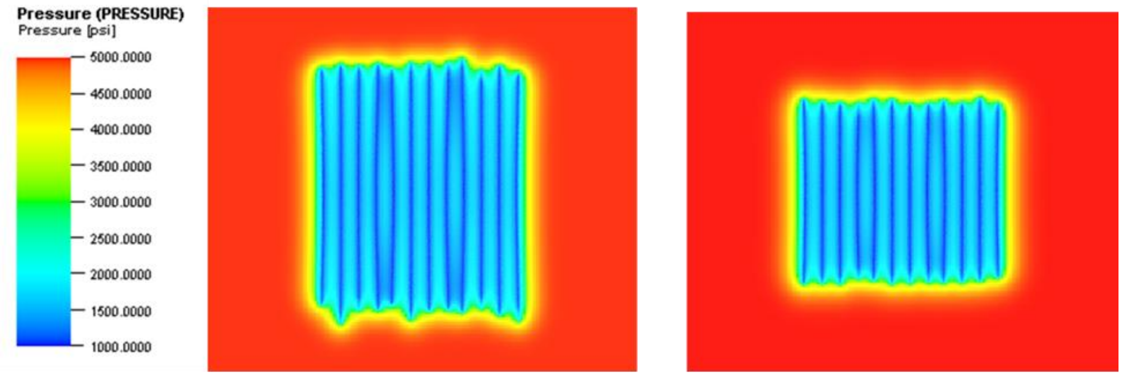

(a) (b)

Figure 2.13 Pressure contours after 3 years production (a) Long fractures (average x_f =734 ft) (b) Short fractures (average x_f=515 ft) (reprinted with permission from Xue et al. 2018)

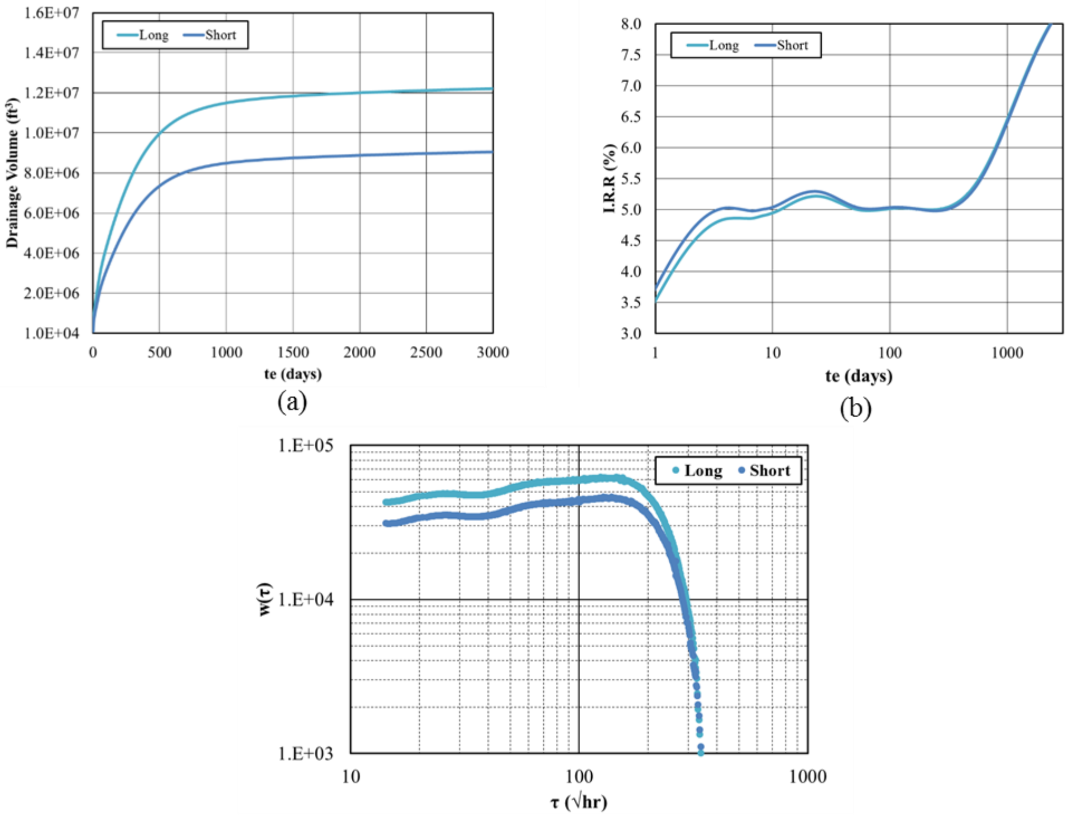

(a) (b) (c)

Figure 2.14 Comparison of fracture surface area: (a) Drainage volume (b) IRR plot (c) w(τ) plot (reprinted with permission from Xue et al. 2018)

2.4.3.2 Impact of Fracture Cluster Spacing

To investigate the sensitivity of cluster spacing, we change the cluster spacing from 100ft (base case) to both 70ft and 150ft. Figure 2.15 shows the pressure contours after 3 years of production and Figure 2.16 shows $V_d(t)$, IRR and $w(\tau)$ plot. As can be seen from Figure 2.15, as the cluster spacing becomes smaller, the reservoir depletes faster. In addition, from the $w(\tau)$ plot in Figure 2.16, different cluster spacing have similar trend of $w(\tau)$ plot. However, with smaller cluster spacing, the onset of fracture interference becomes earlier. Therefore, like the traditional RNP plot, $w(\tau)$ plot can give us the precise signal of fracture interference. In addition, from the IRR plot, we can also see the onset of fracture interference as the IRR plot suddenly goes up. However, we recommend to use the $w(\tau)$ plot here as it is more sensitive than the IRR plot.

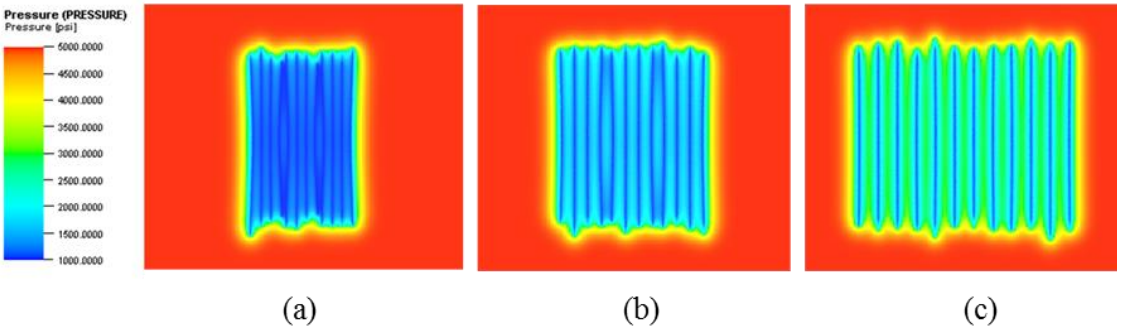

Figure 2.15 Pressure contours after 3 years production (a) Cluster spacing=70ft (b) Cluster spacing=100ft (c) Cluster spacing=150ft (reprinted with permission from Xue et al. 2018)

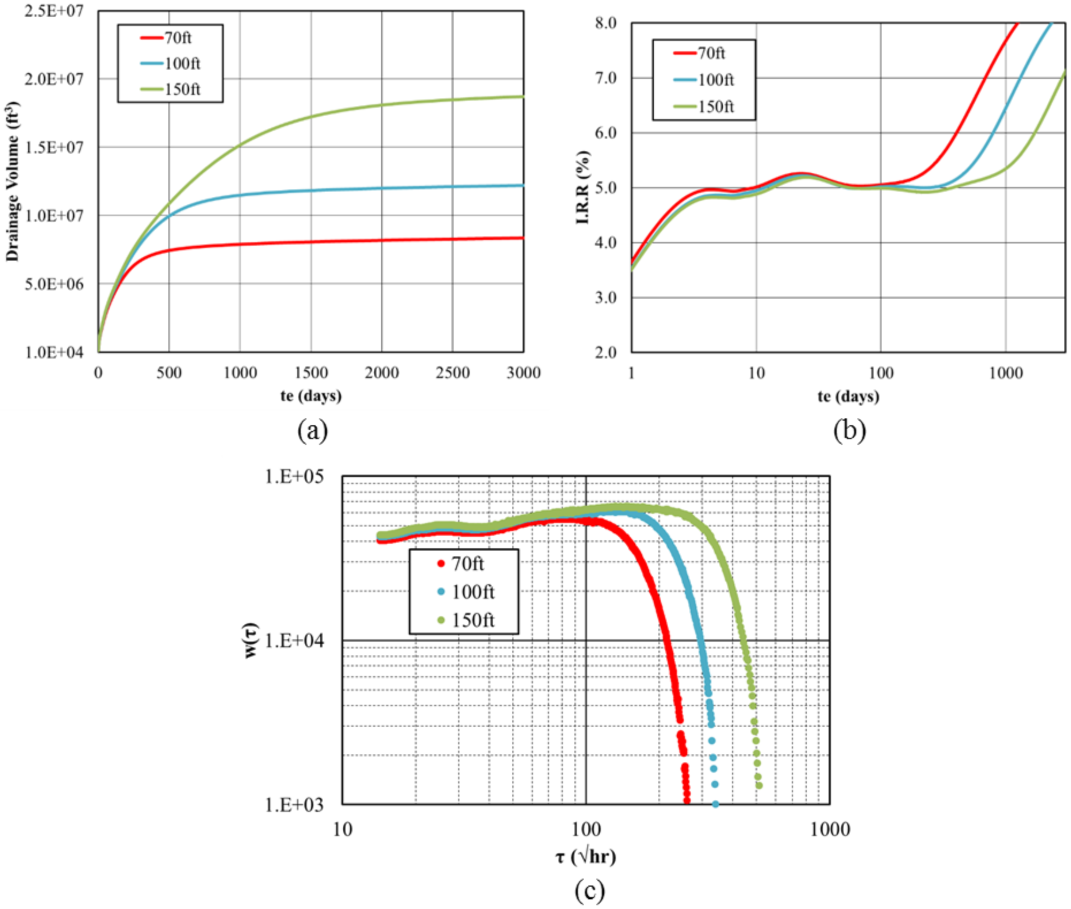

Figure 2.16 Comparison of fracture cluster spacing: (a) Drainage volume (b) IRR plot (c) w(τ) plot (reprinted with permission from Xue et al. 2018)

2.4.3.3 Impact of Fracture Conductivity

In this section, we focus on the IRR plot. We will see that with similar drainage volume and w(τ) plot, IRR plot could give us the information of fracture conductivity and fracture compaction. To investigate the sensitivity of fracture conductivity, we change the proppant concentration from 1 ppa to 4 ppa with 3 ppa as the base case. When we change the proppant concentration from 1 ppa to 4 ppa, the average fracture half-length changes from 807ft to 723ft. This is because when we use large proppant concentration, the fracture width will increase, which lead to shorter fracture half-length. We consider four scenarios that have similar fracture surface area. Figure 2.17 shows the results of $V_d(t)$, IRR and w(τ) for this four scenarios. The results of drainage volume and w(τ) proves our assumption that the four scenarios have similar fracture surface area since they have similar drainage volume and similar w(τ) plot. The main difference is the IRR plot. With the increase of proppant concentration, the IRR plot at early time significantly increases. The reason is that with similar drainage volume, higher fracture conductivity tends to produce more which increases the IRR plot at early time. Therefore, with similar drainage volume, IRR plot at early time is a good indicator of fracture conductivity.

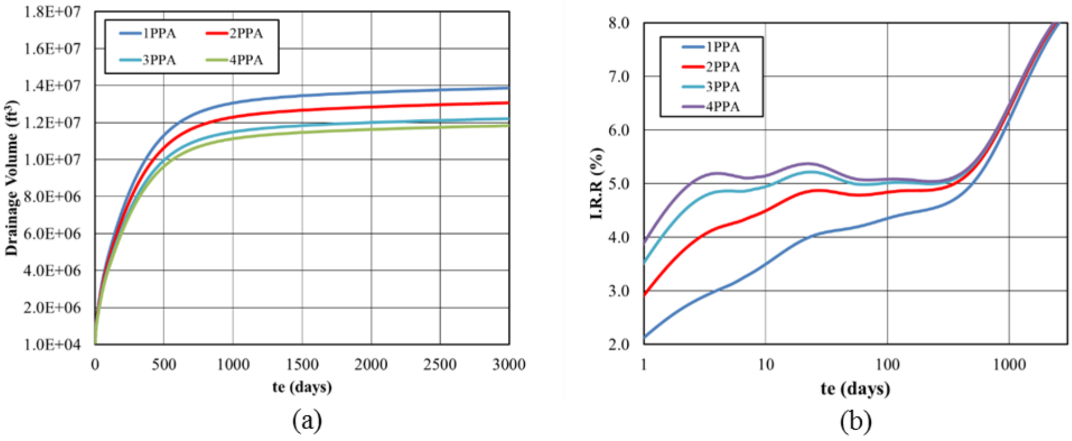

Figure 2.17 Comparison of fracture conductivity: (a) Drainage volume (b) IRR plot (c) w(τ) plot (reprinted with permission from Xue et al. 2018)

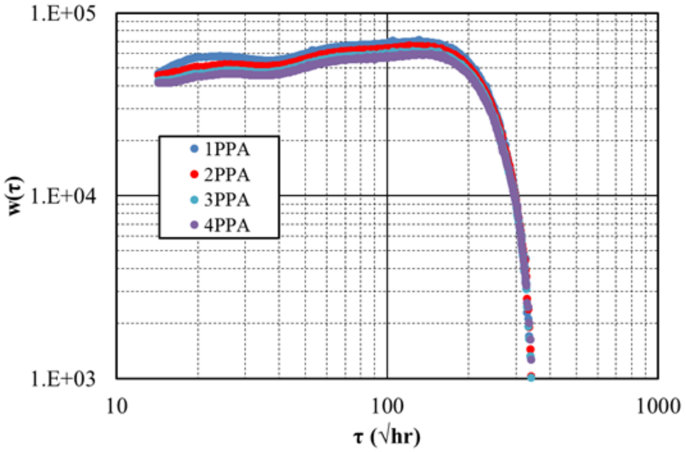

(c)

Figure 2.17 continued

2.4.3.4 Impact of Fracture Complexity

In order to further validate the applicability of the diagnostic plots in complex fracture conditions, we investigate the influence of stress anisotropy (the difference between maximum and minimum horizontal stress) on $V_d(t)$, IRR and w(τ). Figure 2.18 shows the pressure contours after 3 years of production and Figure 2.19 shows the corresponding $V_d(t)$, IRR and w(τ) plot. As the stress anisotropy reduces from 200 to 0 psi, the fracture shape becomes highly complex. As can be seen from Figure 2.18(b), some shorter middle fractures intersect with the outer longer fractures, significantly reducing the total fracture surface area. As a result, the drainage volume and w(τ) value dramatically decrease because of smaller fracture surface area. From the w(τ) plot in Figure 2.19, we can still see the four flow regimes, fracture flow, formation linear flow, partial completion and fracture interference. The fracture interference happens more gradually than the large stress anisotropy case because of the fracture complexity.

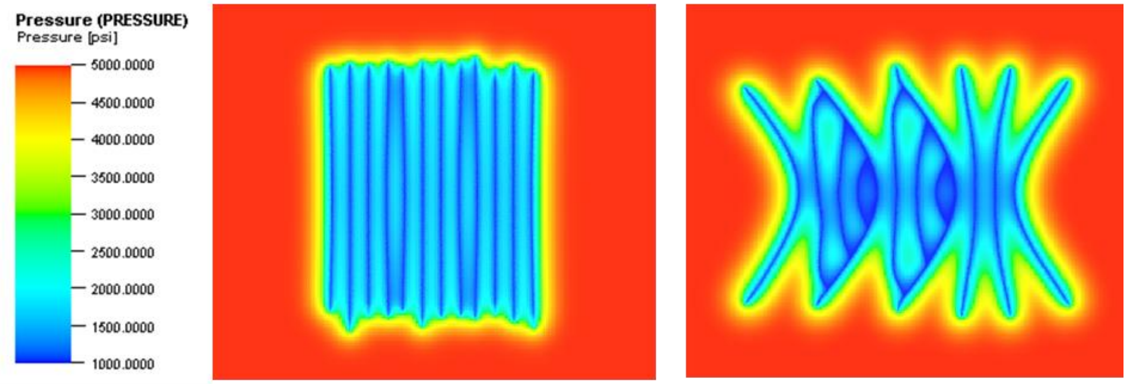

(a) (b)

Figure 2.18 Pressure contours after 3 years production (a) Stress anisotropy=200spi (b) Stress anisotropy=0spi (reprinted with permission from Xue et al. 2018)

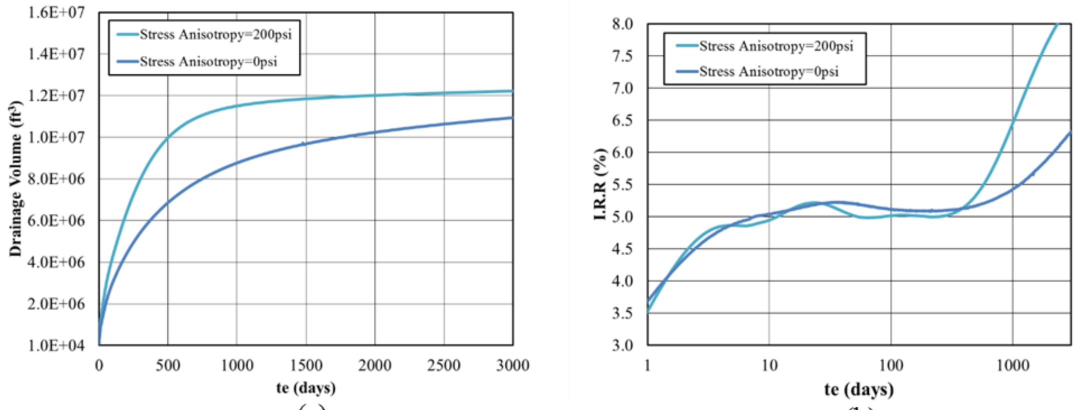

(a) (b)

Figure 2.19 Comparison of stress anisotropy: (a) Drainage volume (b) IRR plot (c) w(τ) plot (reprinted with permission from Xue et al. 2018)

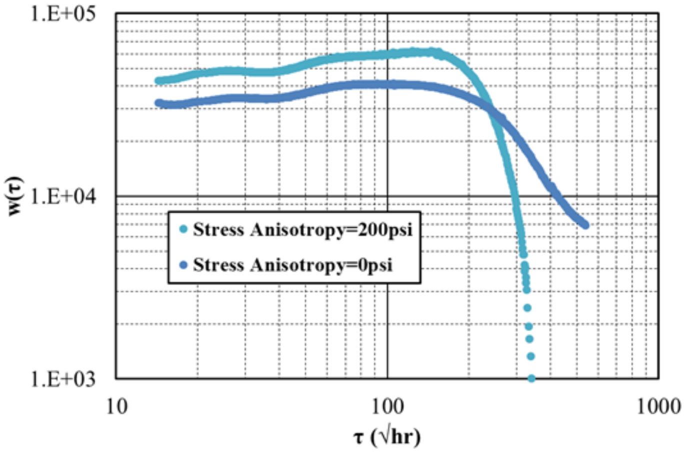

(c)

Figure 2.19 continued

2.4.3.5 Impact of Fracture Compaction

The effective fracture conductivity is related to the performance of proppant pack under certain reservoir conditions. Guidelines for proppant selection tend to choose proppant with high proppant strength to withstand closure stress and avoid crushing or embedment. In order to simulate the fracture compaction effect on the proppant pack, we use an experimental compaction data for the proppant Jordan Unimin 30/50, which relates the closure stress with the proppant permeability as given in Figure 2.20. During our simulation, Table 2.6 is used to convert the closure stress to a series of transmissibility multipliers to account for the proppant deterioration. The real transmissibility multipliers are directly from the experimental data while strong case considers more severe proppant deterioration.

In Figure 2.21 we show the results of $V_d(t)$, IRR and $w(\tau)$ for three scenarios. As observed from the plots, the three scenarios have identical drainage volume and $w(\tau)$ plot since they have the same fracture geometry. The interesting part is the IRR plot. The real case only have slight deterioration when the pressure drop is small. Therefore, at early time the real case only have small difference compared with no fracture compaction case. As for the strong compaction case, we see significant difference at early time since we have strong deterioration from the beginning of the production. However, there is no big difference for the three scenarios at late time after the fracture interference begins. Accordingly, the IRR plot at early time before fracture interference could give us the information of fracture compaction due to proppant deterioration.

Table 2.6 Transmissibility multipliers for proppant deterioration simulation (reprinted with permission from Xue et al. 2018)

Reservoir Pressure (psi)	Transmissibility multiplier (real)	Transmissibility multiplier (strong)
4368	1	0.6
3824	0.99	0.59
3279	0.96	0.56
2735	0.92	0.52
2191	0.89	0.49
1647	0.83	0.83
1103	0.76	0.36
559	0.69	0.29
14.7	0.62	0.22

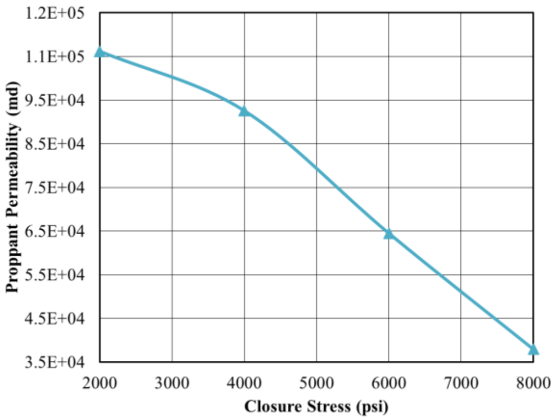

Figure 2.20 Proppant deterioration with closure stress (reprinted with permission from Xue et al. 2018)

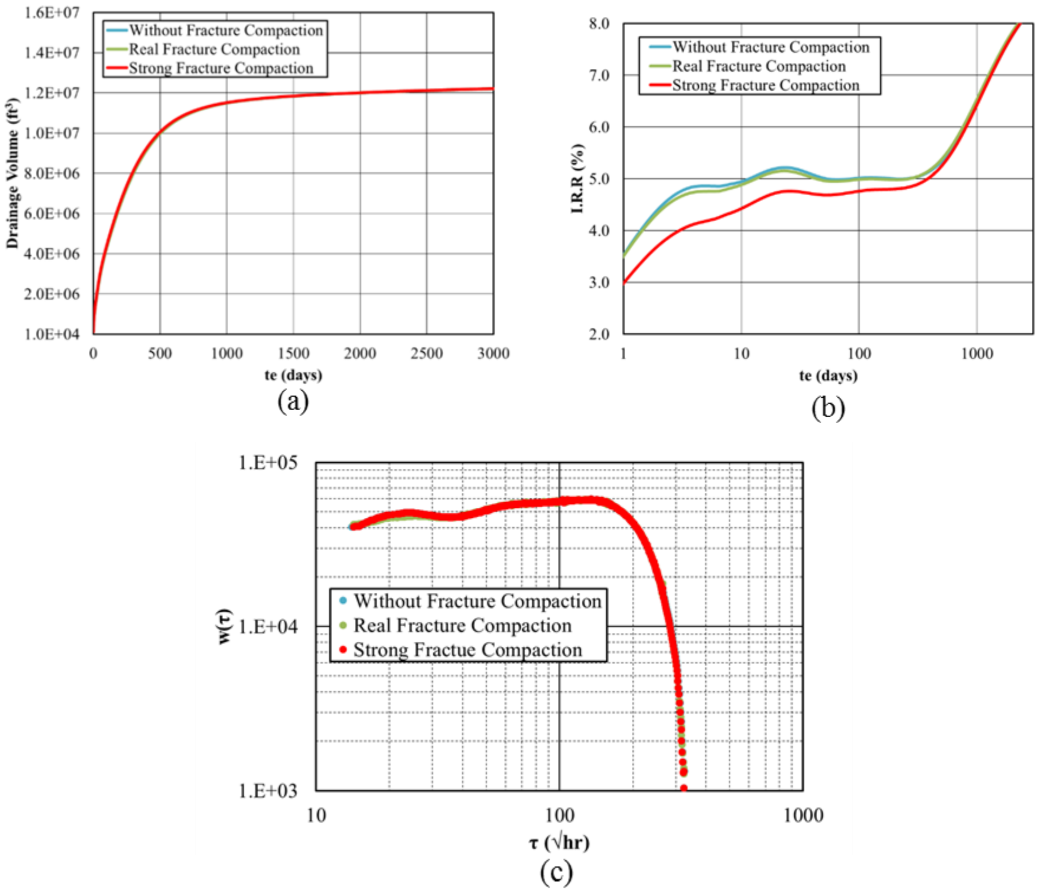

Figure 2.21 Comparison of fracture compaction: (a) Drainage volume (b) IRR plot (c) w(τ) plot (reprinted with permission from Xue et al. 2018)

2.4.4 Quantitative Analysis using the w(τ) Plot

In this section, we demonstrate the feasibility of using the w(τ) plot for quantitative analysis of formation permeability, total fracture surface area and stimulated reservoir volume (SRV). We first use a synthetic case to validate our calculations followed by a field application. For validation purpose, we build a simulation model with known fracture geometry and fluid properties shown in Table 2.7.

Table 2.7 Reservoir and fluid parameters for quantitative analysis (reprinted with permission from Xue et al. 2018)

Parameter	Value
Cluster Spacing	100 ft
Fracture Number	12
Fracture Half Length	300 ft
Formation Thickness	100 ft
Matrix Porosity	0.05
Matrix Permeability	0.0001 md
Initial Pressure	5000 psi
Fluid Viscosity	1 cp
Total Compressibility	4.0E-6 1/psi

Step 1: Fracture Interference τ and Formation Permeability

Our first step is to determine the fracture interference τ and formation permeability using the w(τ) plot. We have already demonstrated that w(τ) plot can identify fracture interference from Figure 2.16. Figure 2.22 shows the schematic diagram of fracture interference. The yellow pillbox mimics the drainage volume of a single fracture. The fracture interference begins when the two pillboxes meet each other. Therefore, we can relate the fracture interference τ_{FI} with fracture cluster spacing x_s as:

$$\tau_{FI} = \frac{x_s}{2\sqrt{\alpha}} \tag{2.25}$$

where

$$\alpha = \frac{k}{\phi \mu c_t} \tag{2.26}$$

The formation permeability can now be calculated knowing the fluid viscosity and total compressibility.

$$k = \frac{x_s^2}{4\tau_{FI}^2} \phi \mu c_t \tag{2.27}$$

Figure 2.23 shows the pressure contour after 3 years of production and Figure 2.24 gives the drainage volume, IRR and w(τ) plot. From the w(τ) plot, we can pick up the fracture interference at $\tau_{FI} = 137.7\sqrt{hr}$. Substituting this value into Eq. (2.27), we can calculate the formation permeability k=0.0001md, which equals to the formation permeability in Table 2.7.

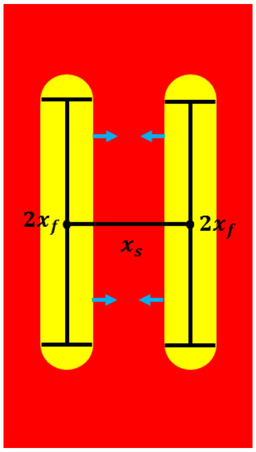

Figure 2.22 Schematic diagram of fracture interference using the pillbox model (reprinted with permission from Xue et al. 2018)

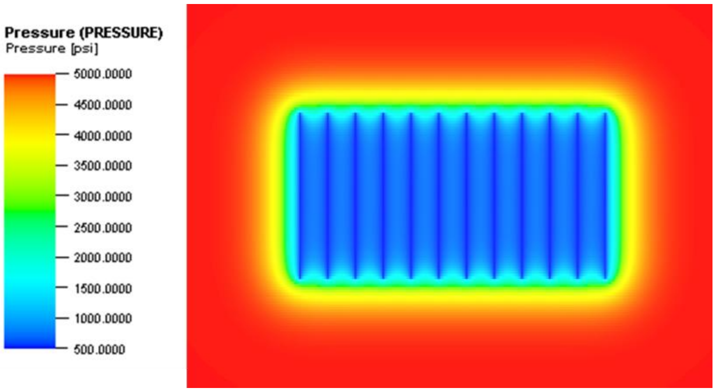

Figure 2.23 Pressure contour after 3 years production (reprinted with permission from Xue et al. 2018)

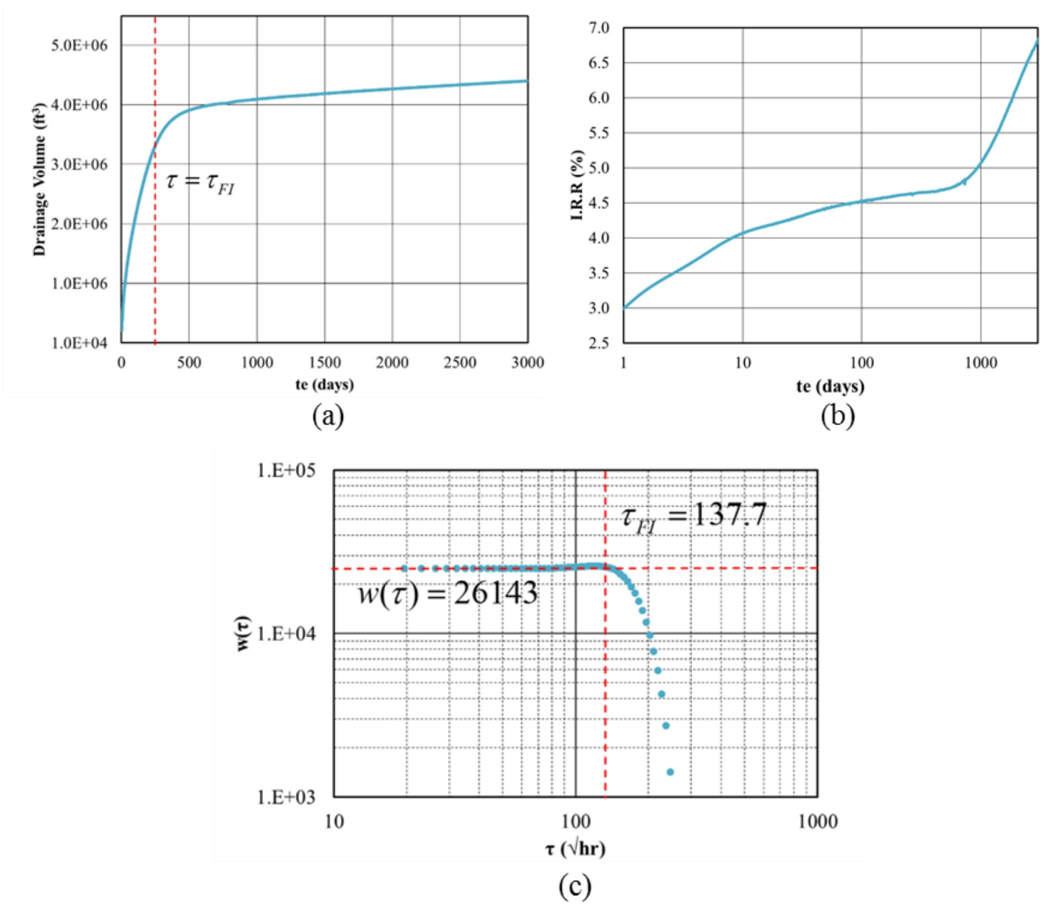

(a)

(b)

(c)

Figure 2.24 Quantitative analysis: (a) Drainage volume (b) IRR plot (c) w(τ) plot (reprinted with permission from Xue et al. 2018)

Step 2: Total Fracture Surface Area

From Eq. (2.22), during the formation linear flow, the w(τ) is constant and represents a combination of total fracture surface area, diffusivity and porosity.

$$w(\tau) = A_f \sqrt{\alpha}\phi \tag{2.28}$$

where

$$A_f = \sum_{i=1}^{n} 4 \times x_{fi} \times h_{fi} \tag{2.29}$$

$$A_f = \frac{w(\tau)}{\sqrt{\alpha}\phi} \tag{2.30}$$

From the w(τ) plot, we can pick up the w(τ) value at the formation linear flow regime w(τ)=26143 $ft^3/\sqrt{}hr$. Substituting this value into Eq. (2.30), we can calculate the total fracture surface area A_f=1440000 ft^2, which equals to the total fracture surface area in Table 2.7.

Step 3: Stimulated Reservoir Volume (SRV)

We first use the fracture interference $\tau_{FI} = 137.7\sqrt{hr}$ to get the drainage volume from the drainage volume plot in Figure 2.24(a). Since $\tau_{FI} = 137.7\sqrt{hr}$, we can calculate the corresponding time t=197.5days using the relation $t = \frac{\tau^2}{4}$ (Xie et al. 2015a). From Figure 2.24 (a), the drainage volume at 197.5days equals to 3.06×10^6. Following Song and Ehlig-Economides (2011), the SRV volume is given by:

$$V_{SRV} = \phi L h (2x_f + \frac{x_s}{2}) \tag{2.31}$$

where L is the horizontal well length, h is the formation thickness, x_f is the fracture half-length and x_s is the cluster spacing. In our calculation, we use the drainage volume at the fracture interference plus the distance the pressure penetrates beyond the fracture tips, which is:

$$V_{SRV} = V_{FI} + \phi Lh \frac{x_s}{2} \tag{2.32}$$

Using Eq. (2.32), our estimated SRV volume equals to $3.06\times10^6+2.75\times10^5=3.34\times10^6$ ft^3. The result from Eq. (2.31) equals to 3.58×10^6 ft^3. The proposed methodology gives us similar estimated SRV volume compared with traditional analysis but does not rely on specific fracture geometry. The estimated SRV volume is obtained directly from the drainage volume plot.

2.4.4 Field Applications

In this section, we apply our methodology to a series of Eagle Ford and Wolfcamp shale oil wells to calculate $V_d(t)$, IRR and $w(\tau)$. For the Eagle Ford wells, the depth is about 11,000 ft, with initial reservoir pressure of 8100 psi and temperature of 270 ^{o}F. The average porosity is 8.2% and the permeability is in the range of 100-20000 nd. For the field applications, we follow the same procedure as the synthetic cases. We fit the pressure data with respect to cumulative production and the production rate with respect to time to get the overall trend of pressure and production rate.

Figure 2.25 shows the results of $V_d(t)$, IRR and $w(\tau)$ for five wells. Wells 7A and 18A belong to Wolfcamp shale while wells 10H-12H belong to Eagle Ford shale. The drainage volume evolution shows a similar trend for the five wells. The drainage volume rapidly increases at early time and then stabilizes at late time. Comparing the drainage volume of the two fields, the wells in Wolfcamp show significant larger drainage volume than Eagle Ford wells. The w(τ) plot also shows different trends for the two fields. For the Eagle Ford shale wells, at early time, the w(τ) value is constant or has a small upward trend, which indicates the formation linear flow or a combination of formation linear flow and partial completion effect. At late time, the w(τ) plot gradually decreases indicating the onset of fracture interference. For the Wolfcamp shale wells, the w(τ) value dramatically increases at early time followed by sharp decline at late time. The dramatic increase indicates a strong partial completion effect. Also, the larger w(τ) value indicates higher fracture surface area. Comparing the w(τ) plot of the wells in Eagle Ford, we can conclude that well 10H has the largest fracture surface area because of the largest w(τ) value at early time before fracture interference. The IRR plot of the five wells monotonically increases with time, which indicates continual increase in depletion efficiency.

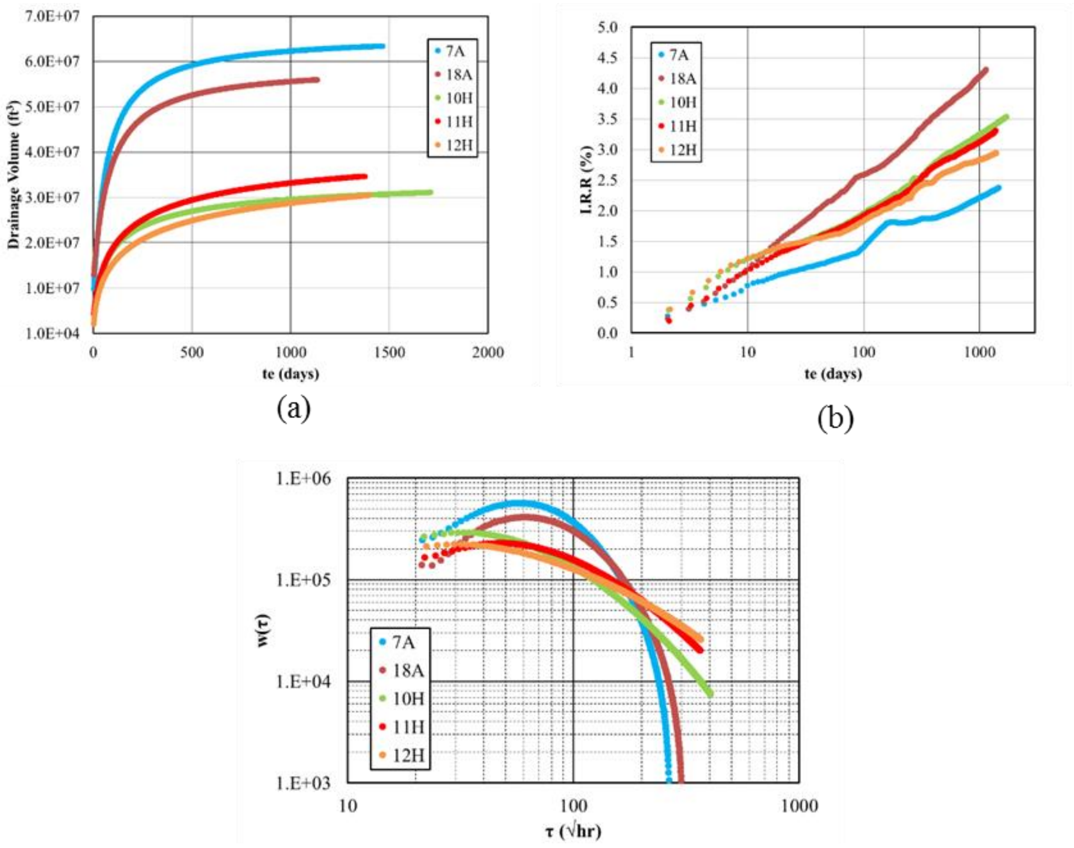

(a)

(b)

(c)

Figure 2.25 Field applications of shale oil wells: (a) Drainage volume (b) IRR plot (c) w(τ) plot (reprinted with permission from Xue et al. 2018)

Figure 2.26 compares two diagnostic plots for well 18A: our proposed method and the RNP analysis. From the w(τ) plot, we can clearly see a strong partial completion effect at early times. But from the RNP plot we can only see the ½ slope line, which is the formation linear flow. This demonstrates the higher resolution flow diagnostics from our w(τ) plot. Using a porosity of 10 %, viscosity of 0.78 cp, total compressibility of 3×10^{-5} 1/psi, cluster spacing of 40 ft, and the formation thickness of 350 ft, we can use Eq. (2.27) to estimate the formation permeability equal to 840 nd. Then using Eq. (2.30) and (2.32), we can estimate the total fracture surface area A_f=4490000 ft2 and the SRV volume $V_{SRV}=3.27\times10^7$ ft^3.

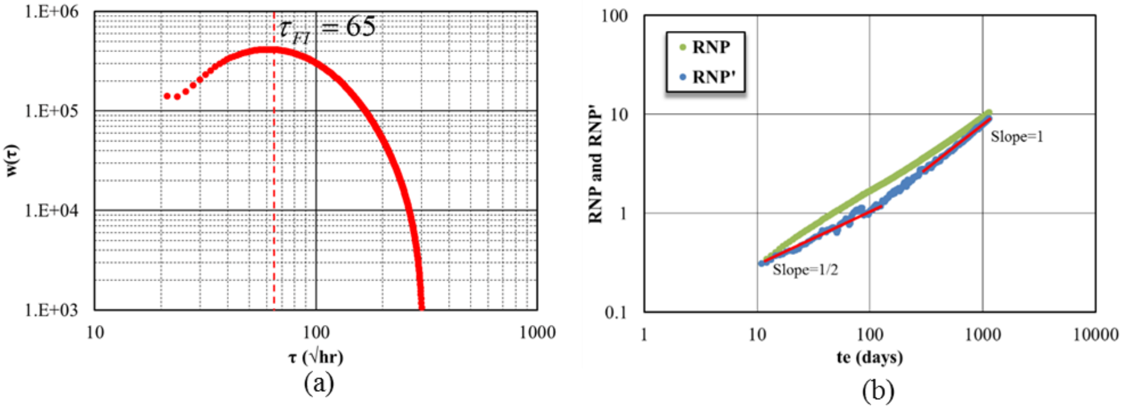

Figure 2.26 Comparison of the diagnostic plots for well 18A (a) w(τ) plot (b) RNP and RNP' plot (reprinted with permission from Xue et al. 2018)

2.4 Conclusions

In this chapter, we propose a novel diagnostic approach to interpret the flow characteristics in complex fracture systems. Using fracture propagation modeling together with reservoir simulation, complex fracture systems under different completion and reservoir conditions are analyzed using production and pressure response. Applications to field cases of Eagle Ford and Wolfcamp shale oil wells demonstrate the practical feasibility of our approach. Some key conclusions for this paper are summarized as follows:

- We demonstrate that the w(τ) plot provides more information of flow patterns compared to the traditional RNP diagnostic plot. The constant w(τ) indicates formation linear flow. When w(τ) increases linearly with τ with unit slope, it indicates radial flow. When w(τ) increases linearly with τ with less than unit slope, it indicates fracture flow at early time or partial completion at intermediate time. Finally, when w(τ) trends downward, it indicates boundary dominated PSS flow or fracture interference.

- w(τ) value at early and intermediate time gives information about fracture surface area. With similar diffusivity, larger w(τ) value at early and intermediate time indicates larger fracture surface area.
- IRR plot at early and intermediate time gives the information about fracture conductivity and fracture compaction. With similar drainage volume and w(τ) plot, larger IRR value at early and intermediate time indicates larger fracture conductivity.
- We demonstrate the feasibility of using w(τ) plot to do a quantitative analysis of formation permeability, total fracture surface area and stimulated reservoir volume (SRV). The synthetic model validates the quantitative analysis results. The advantage of this new methodology is the ease of analysis and its generality as we do not rely on simple fracture geometry.

CHAPTER III

MODELING HYDRAULICALLY FRACTURED SHALE WELLS USING THE FAST MARCHING METHOD WITH LOCAL GRID REFINEMENTS (LGRS)

3.1 Chapter Summary

Recently the Fast Marching Method (FMM) based flow simulation has shown great promise for rapid modeling of unconventional oil and gas reservoirs. Currently, the application of FMM-based simulation has been limited to the use of tartan grid to model the hydraulic fractures (HFs). The use of tartan grids adversely impacts the computational efficiency, particularly for field-scale applications with hundreds of HFs. This chapter is aimed at extending the FMM-based simulation to incorporate local grid refinements (LGRs) to simulate HFs and validating the accuracy and efficiency of the methodology.

The FMM-based simulation is extended to LGRs. This requires novel gridding through introduction of triangles (in 2D) and tetrahedrons (in 2.5D) to link the local and global domain and solution of the Eikonal equation in unstructured grids to compute the 'diffusive time of flight'. The FMM-based flow simulation reduces 3D simulation to an equivalent 1D simulation using the 'diffusive time of flight (DTOF)' as a spatial coordinate. The 1D simulation can be carried out using standard finite-difference method leading to orders of magnitude savings in computation time compared to full 3D simulation for high-resolution models.

We first validate the accuracy and computational efficiency of the FMM-based simulation with LGRs by comparing with tartan grids. The results show good agreements

and the FMM-based simulation with LGRs shows significant improvement in computational efficiency. Then, we apply the FMM based simulation with LGRs to a multi-stage hydraulically fractured horizontal well with multiphase flow case to demonstrate the practical feasibility of our proposed approach. After that, we investigate various discretization schemes for the transition between local and global domain in the FMM-based flow simulation. The results are used to identify optimal gridding schemes to maintain accuracy while improving computational efficiency.

This is the first study to apply the FMM-based flow simulation with LGRs. The three main contributions of the proposed methodology are: (i) unique mesh generation schemes to link fracture and matrix flow domains (ii) diffusive time of flight calculations in locally refined grids (iii) sensitivity studies to identify optimal discretization schemes for the FMM-based simulation.

3.2 Background

From the reservoir simulation point of view, the most popular techniques to simulate the hydraulic fracture networks are local grid refinements (LGRs), discrete fracture model (DFM) and embedded discrete fracture model (EDFM). The LGR method is the most common one because of its simplicity and efficiency. In this method, we use locally refined grids to explicitly represent the main hydraulic fractures. The stimulated reservoir volume (SRV) regions are used to represent the corresponding complex fracture networks surrounding the main hydraulic fractures (Mayerhofer et al. 2010). However, the limitation of the LGR method is that the main hydraulic fractures are aligned with the underlying grid system, which cannot simulate arbitrary fracture geometry. DFM is another method to simulate the hydraulic fracture networks. This method directly generates the unstructured grid based on the fracture geometry, which can simulate arbitrary fracture geometry without simplification (Karimi-Fard and Firoozabadi 2001; Karimi-Fard et al. 2004; Mi et al. 2016). However, this method can be computationally burdensome and impractical for history matching and optimization at the field level.

The FMM-based simulation has already shown its strong capability to handle field scale unconventional reservoir analysis (Iino et al. 2017; Iino and Datta-Gupta 2018). This method is based on the high frequency approximation of the asymptotic solution to the diffusivity equation, which results in the Eikonal Equation (Vasco et al. 2000). The Eikonal equation can be efficiently solved by a front tracking algorithm called Fast Marching Method (Sethian 1996, 1999). By solving the Eikonal equation, we can get the diffusive time of flight (DTOF), which is a generalization of the ‘radius of investigation’ (Datta-Gupta et al. 2011). Zhang et al. (2016) first proposed to use DTOF as a spatial coordinate to transform the 3D model to a corresponding 1D model and solve the 1D equation numerically. Following this idea, we incorporated complex physics such as compositional simulation into the FMM-based simulation (Iino and Datta-Gupta 2018). However, our previous work was based on tartan grid model, which limits the computation speed and cannot handle complex facture networks. Yang et al. (2017) extended the FMM-based simulation to the unstructured grid systems. In this chapter, we will further extend the FMM-based simulation to LGRs.

This chapter is organized as follows. We begin with an overview of the FMM-based simulation, including the equations and the workflow to transform the model from 3D to 1D. Next, we will show the details of the FMM-based simulation with LGRs, including mesh generation and validation. In addition, we will review the local Eikonal equation solver based on Eulerian discretization from our previous study. Finally, we will discuss different gridding schemes and their accuracy and efficiency.

3.3 Methodology

3.3.1 Overall Workflow of FMM-based Simulation

The overall workflow of the FMM-based simulation is shown in Figure 3.1. The FMM-based simulation consists of six steps. First, we calculate the multi-phase diffusivity on each grid block. Second, using the multi-phase diffusivity as an input parameter, we run the FMM to calculate the DTOF on each grid block. Third, we accumulate pore volume using DTOF as a spatial coordinate and then discretize the cumulative pore volume in terms of the DTOF. Fifth, we calculate the $w(\tau)$ function, which is the first derivative of the cumulative pore volume with respect to the DTOF. After getting the $w(\tau)$ function, we use it to calculate all the 1D parameters such as transmissibility, pore volume, and well index. Finally, we build the 1D model and run the simulation on the 1D model to get the well response. Following this workflow, we transform the original 3D model into an equivalent 1D model. Since we solve the 1D equation instead of 3D, the computation can speed up orders of magnitude faster compared with the original 3D model.

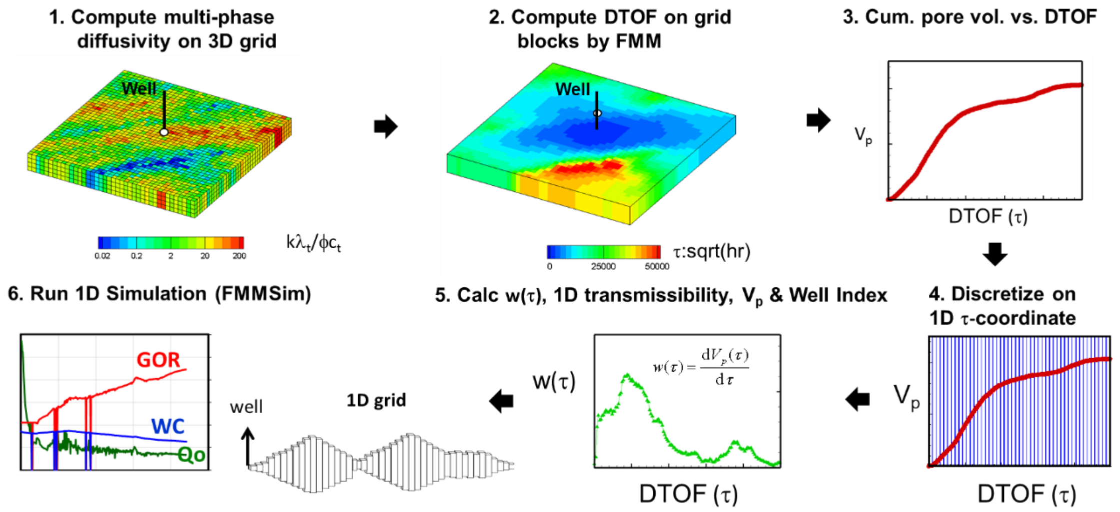

Figure 3.1 Overall workflow of FMM-based simulation

3.3.2 Extension of the FMM-based Simulation to LGRs

In this section, we discuss three important parts of our proposed methodology. First, we introduce the grid generation of the LGR. This requires novel gridding through introduction of triangles (in 2D) and tetrahedrons (in 2.5D) to link the local and global domain. Second, we review the local Eikonal equation solver based on the Eulerian discretization of triangle grid (in 2D) and tetrahedron grid (in 2.5D). Third, we validate our proposed methodology using FMM with tartan grid from previous study and finite difference simulation.

3.3.2.1 LGRs Grid Generation

The grid generation consists of three steps. First, based on the location of the hydraulic fractures, we generate the normal LGRs and the matrix grid. Second, we construct the 2D triangles at global and local domain. Here, we need special treatment to handle the connections between global and local domain. Third, we build the 2.5D grid based on the 2D triangles by assembling multiple layers and allowing vertical thickness variation.

In Figure 3.2, we give an example to describe step one of the LGRs grid generation. Figure 3.2(a) shows an entire reservoir view. Our example is a 1000ft×1000ft reservoir with one horizontal well and one hydraulic fracture. Figure 3.2(b) is a zoom in to Figure 3.2(a) and we use a 5×3 LGR to represent the hydraulic fracture. Here 5×3 LGR means 5 local cells in the x direction and 3 local cells in the y direction inside one global cell. The inner cells in the x direction are used to represent the hydraulic fracture. This step is the same as the normal LGR gridding in finite difference simulation.

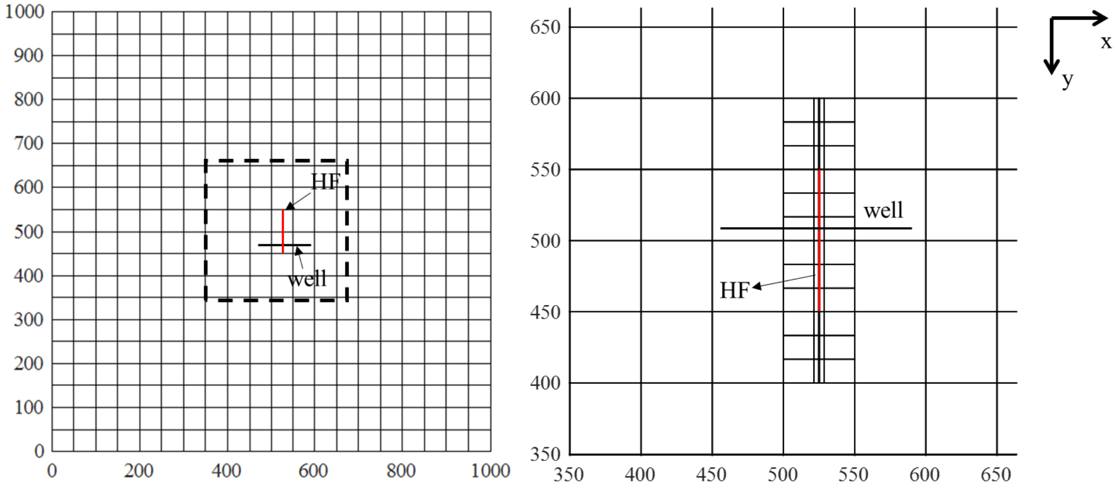

(a) (b)

Figure 3.2 LGRs grid generation (a) Entire reservoir view (b) Zoom in at fracture location with 5×3 LGR to represent hydraulic fracture

Figure 3.3 shows step two of the LGRs grid generation. After generating the cells in global and local domain, we construct the triangular cells for the local Eikonal solver. We can either use same or different resolution in global and local domain. In this example, we use different resolution. In the global domain, we use a 5 points scheme and generate 4 triangles within one original cell, for example cell 'a' in Figure 3.3. In the local domain, we use a 9 points scheme and generate 8 triangles within one original cell, as in cell 'b' in Figure 3.3. We need a special treatment for the global cells next to the LGR regions. Since the cells in global and local domain have different resolution, we need to add additional triangles to link between the high-resolution LGR regions and the center point of the low-resolution matrix region, as in cell 'c' in Figure 3.3. In this way, we can accurately update the DTOF from the high-resolution LGR regions to the low-resolution matrix region.

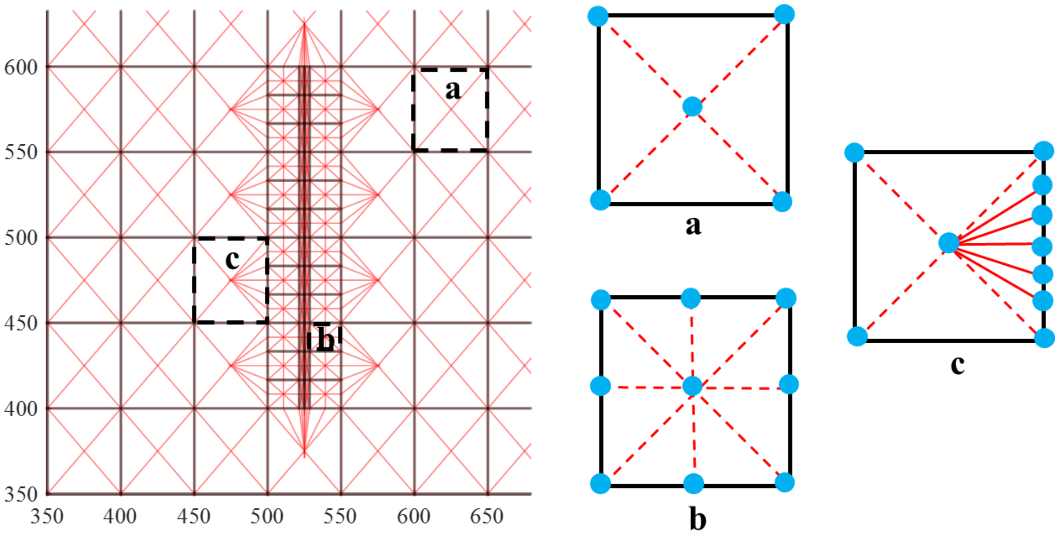

Figure 3.3 2D triangle grid generation at global and local domain

After generating the 2D triangular grid, we can easily extend the entire system to 2.5D grid. Based on the input vertical thickness, every 2D triangle can be extended to several 2.5D triangular prisms allowing different layer thickness. In Figure 3.4(a), we show the 2.5D grid result following the previous step. In Figure 3.4(b), we illustrate a triangular prism generated using triangle ABC. The 2.5D triangular prisms are the basic computation unit of the DTOF calculation.

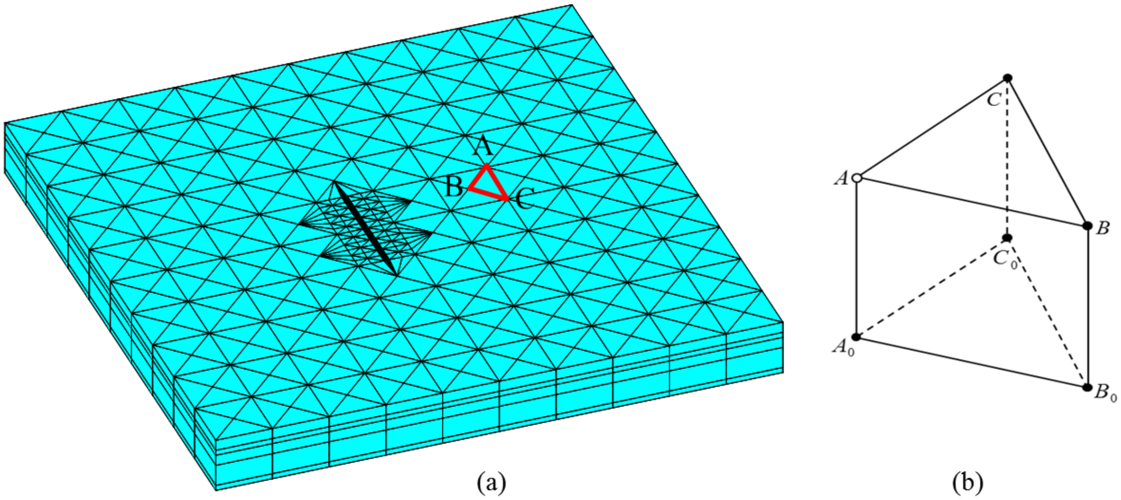

(a) (b)

Figure 3.4 2.5D grid generation (a) Entire reservoir view (b) Triangular prism

3.3.2.2 Local Eikonal Solver based on Eulerian Discretization

In our previous study, we described the local Eikonal solver in detail (Yang et al. 2017). For completeness, we review the local Eikonal solver based on Eulerian discretization used in this study. The 2.5D triangular prisms are the basic unit to update the DTOF. Within each triangular prism, updating the DTOF at a particular node is based on calculating the DTOF at several “virtual tetrahedrons”. For example, to update the

DTOF at point A in Figure 3.4 (b) based on the known values of the surrounding nodes, we consider the "virtual tetrahedrons" $ABCA_0$, $ABCB_0$, $ABCC_0$, and $AA_0B_0C_0$ to compute four DTOFs and pick up the minimum DTOF value among them. In Figure 3.5, we illustrate the local Eikonal solver based on 3, 2 and 1 known data points denoted as $\{\tau_i\}$ and $\overrightarrow{d_i}$ is the displacement vector from unknown to the known data points. Typically, we encounter fewer than 3 known data points situation at the initiation of the pressure front propagation. The filled circles are known τ values. The blue arrow denotes the gradient of τ and the red arrow indicates the characteristic direction. We check the causality condition of the Eikonal solver by ensuring the characteristic direction is within the volume or face delineated by the data points.

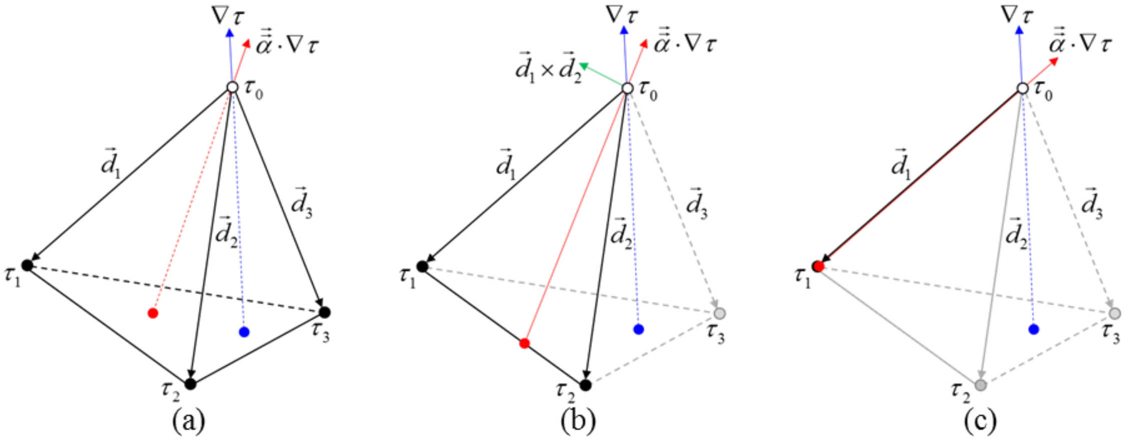

Figure 3.5 Local Eikonal solver based on Eulerian discretization (a) 3 data points (b) 2 data points (c) 1 data point

Starting from the 3 known data points situation, we first project the gradient of onto the displacement vector directions and get the following equations:

$$\tau_i - \tau_0 = \overrightarrow{d_i} \bullet \nabla \tau \qquad i = 1,\ 2,\ 3 \qquad (3.1)$$

The gradient of τ can be further expressed in terms of unit vectors, $\overrightarrow{\sigma_i}$:

$$\nabla \tau = \sum_{i=1}^{3} \overrightarrow{\sigma_i} (\tau_i - \tau_0) \qquad (3.2)$$

where

$$\vec{\sigma}_1 = \frac{\vec{d}_2 \times \vec{d}_3}{\vec{d}_1 \cdot \left(\vec{d}_2 \times \vec{d}_3 \right)} \text{ and cyclic} \qquad (3.3)$$

Substituting Eq. (3.2) into the Eikonal Equation, we can get the following equation:

$$\sum_{i=1}^{3} \overrightarrow{\sigma_i} (\tau_i - \tau_0) \bullet \overset{\rightrightarrows}{\alpha} \bullet \sum_{j=1}^{3} \overrightarrow{\sigma_j} (\tau_j - \tau_0) = 1 \qquad (3.4)$$

We can further rewrite it in the following final form, which is a quadratic equation with τ_0 as the unknown parameter.

$$1 = \sum_{ij=1}^{3} \left(\overrightarrow{\sigma_i} \bullet \overset{\rightrightarrows}{\alpha} \bullet \overrightarrow{\sigma_j} \right) \left(\tau_0 - \tau_i \right) \left(\tau_0 - \tau_j \right) \qquad (3.5)$$

By solving the quadratic Eq. (3.5), we obtain the unknown τ_0. The DTOF only updates when Eq. (3.5) has a solution and satisfies the causality condition. For the 3 known data points situation, the characteristic direction should be confined within the "virtual tetrahedron". To check the causality condition, we solve the parameters a_i after obtaining the unknown τ_0:

$$-\overset{\rightrightarrows}{\alpha} \bullet \nabla \tau = \sum_{j=1}^{3} a_i \overrightarrow{d_i} \qquad (3.6)$$

$$a_i = -\overrightarrow{\sigma_i} \bullet \overset{\Rightarrow}{\alpha} \bullet \nabla \tau = \sum_{j=1}^{3} \left(\tau_0 - \tau_i \right) \left(\overrightarrow{\sigma_i} \bullet \overset{\Rightarrow}{\alpha} \bullet \overrightarrow{\sigma_j} \right) \tag{3.7}$$

The causality condition is satisfied when all of the coefficients are nonnegative $a_i \geq 0$ (Sethian and Vladimirsky 2000). When the causality condition is not satisfied, we formulate the local solver based upon the information from the three edges $\tau_1\tau_2$, $\tau_2\tau_3$ and $\tau_1\tau_3$, as in Figure 3.5(b). We solve the unknown τ_0 from the three edges and pick up the solution that does not violate the causality condition and gives the minimum τ_0. This situation also arises when only 2 points are known data points, which often happens at the beginning of the pressure front calculation. In this situation, Eq. (3.5) cannot be directly solved. Instead, we add another equation based on the causality condition, which is the characteristic direction should be confined within the plane, as in Figure 3.5(b).

$$\left(\overrightarrow{d_i} \times \overrightarrow{d_j} \right) \bullet \overset{\Rightarrow}{\alpha} \bullet \nabla \tau = 0 \tag{3.8}$$

Again, the causality condition is checked using Eq. (3.7), but only for two points. If the causality condition is not satisfied for all the three edges, we come to the 1 known data point situation, as in Figure 3.5(c). We solve the unknown τ_0 directly from the three points τ_1, τ_2, τ_3 and pick up the minimum solution. In this situation, causality condition is automatically satisfied. This situation also happens when only 1 point is known data point.

3.3.2.3 Workflow Validation

In this section, we validate the LGR workflow with a 3D homogeneous example. In this example, we use one hydraulic fracture with a vertical well. The fracture is fully penetrated the reservoir with the fracture conductivity of 500 md.ft. In Figure 3.6, we show the 3D view of this synthetic example and the Table 3.1 gives the input parameters to build this model. The reservoir is initially undersaturated with initial GOR of 1521 SCF/STB and the bubble point pressure at 4351 psi. The well is under BHP control of 1000 psi.

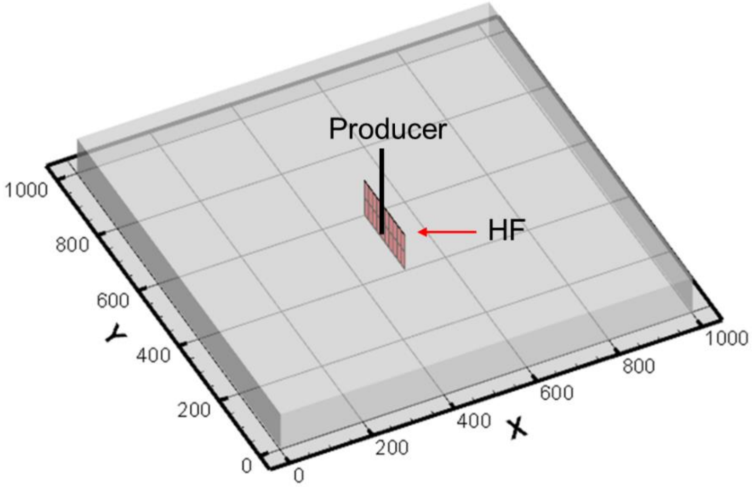

Figure 3.6 3D view of the homogeneous model with one hydraulic fracture

Table 3.1 Reservoir input of the homogeneous model with one hydraulic fracture

Parameter	Value
Reservoir size	$1000\times1000\times100$ ft^3
Initial pressure	6000 psi
Matrix porosity	0.12
Matrix permeability	0.001 md
Rock compressibility(p_{init})	1.0×10^{-6} psi^{-1}
HF porosity	0.25
HF conductivity	500 md.ft
HF height	100 ft
HF half-length	100 ft

Our validation starts from the DTOF contours comparison in Figure 3.7. In this example, we use the 5×1 LGR to represent the hydraulic fracture, which is shown in Figure 3.7(a). Figure 3.7(b) gives the DTOF map using the LGR workflow. Figure 3.7(c) gives the result using tartan grids (Iino et al. 2017) and Figure 3.7(d) shows the tartan grid generated using the LGR workflow. From Figure 3.7, different methods give very similar DTOF contour. We further compare the $w(\tau)$ function calculated using different methods. As can be seen from the 1D fluid flow, the $w(\tau)$ function directly controls the fluid flow in the 1D coordinate. In other words, the accuracy of the $w(\tau)$ function to a large extent determines the simulation results. This is the reason we use the accuracy of the $w(\tau)$ function as a criteria to validate our proposed method. Figure 3.8 shows the $w(\tau)$ function calculated using different methods. From this plot, we can see a good agreement between the new LGR method and the tartan grid method, which validates the proposed method.

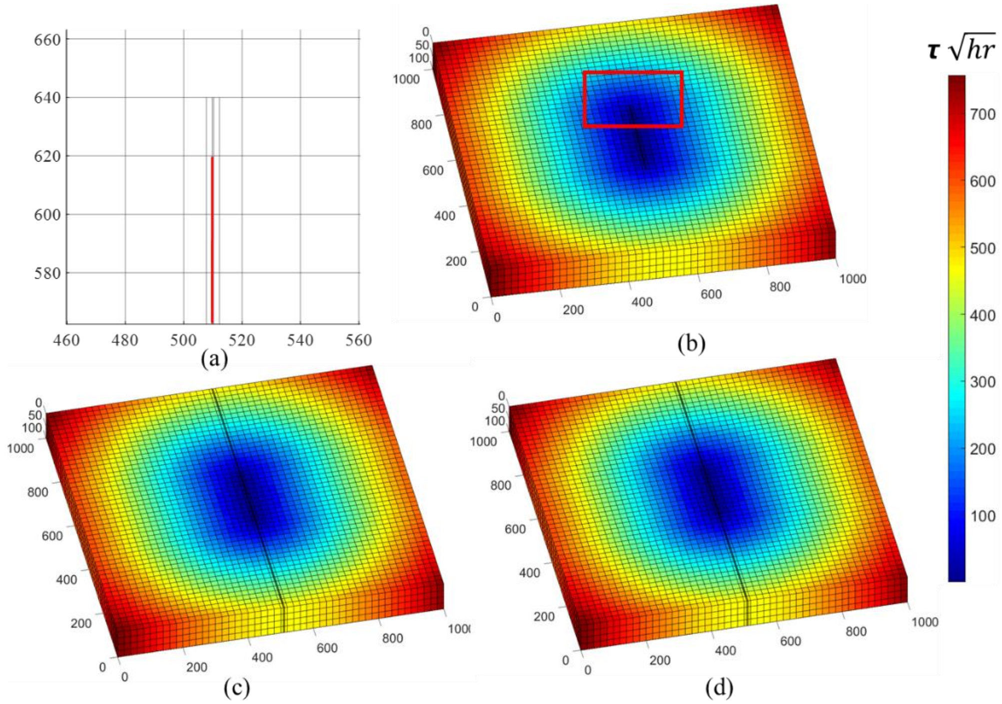

Figure 3.7 Calculated DTOF map (a) Zoom in of the LGR region (b) LGR method (c) Tartan grid method using previous study (d) Tartan grid generated by LGR method

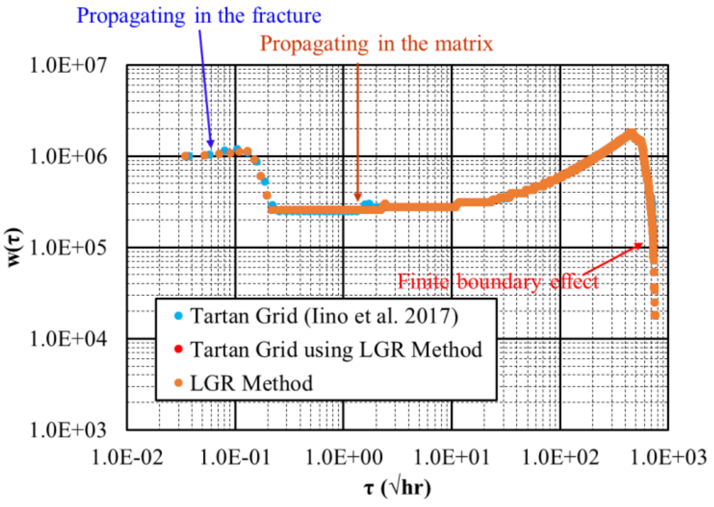

Figure 3.8 w(τ) function generated using different methods

In addition, the w(τ) function quantitatively represents the surface area of the pressure front and different flow regimes. From Figure 3.8, we can identify multiple flow regimes. In the early time, we can see the pressure propagation inside the fracture, followed by the formation linear flow. At the late time, we can see the finite boundary effect after the pressure front reaches the reservoir boundary. Figure 3.9 gives the cumulative production comparison between different methods. Here, we compare the FMM results with tartan grid method, LGR method with the finite difference simulation result. From Figure 3.9, the results of the tartan grid method coincide with the LGR method and only have less than 2% error compared with the finite difference simulation result.

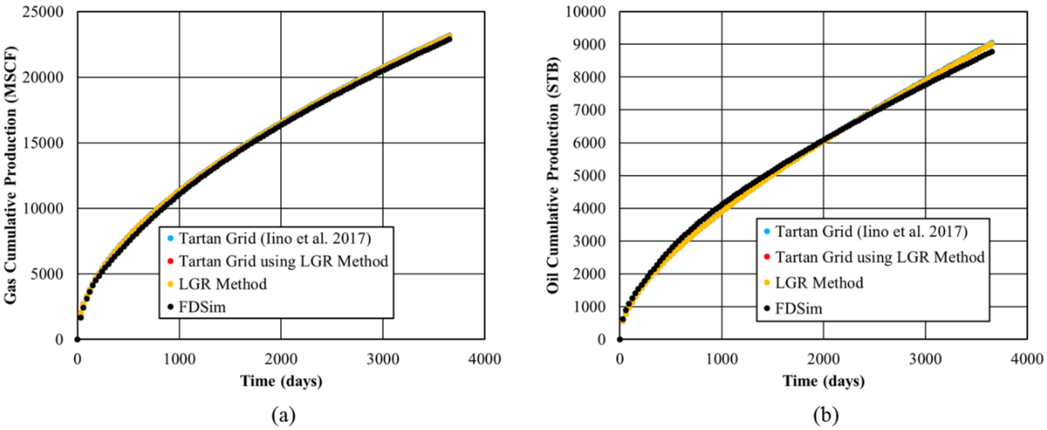

Figure 3.9 Production comparison using different methods (a) Gas cumulative production (b) Oil cumulative production

3.3.2.4 FMM Grid Discretization

The 2.5D triangular prisms are the basic unit to update the DTOF. From Figure 3.10, the 2D 5 points scheme can be generalized to 15 points scheme in 3D. The 2D 9 points scheme can be generalized to 27 points scheme in 3D. The 3D 27 points scheme is the discretization scheme we used in our previous study (Iino et al. 2017; Iino and Datta-Gupta 2018). In this study, we test different discretization schemes of the new LGR method under different circumstances.

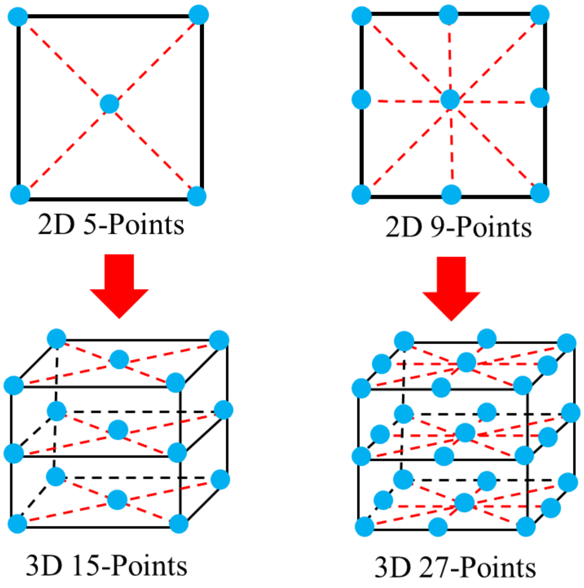

Figure 3.10 Schematic diagram of FMM grid discretization

The first test model is a homogeneous reservoir with 10 hydraulic fractures. Figure 3.11 shows the 3D view of the reservoir and Table 3.2 provides the input parameters of this model. The fluid model is same as the first example. We use the tartan grid 27 points scheme as our reference result. The test schemes are LGR 27 points scheme, LGR 27 points scheme at the hydraulic fracture regions & 15 points scheme at the matrix region, and LGR 15 points scheme. In this model, we use 5×1 LGR to represent the hydraulic fractures.

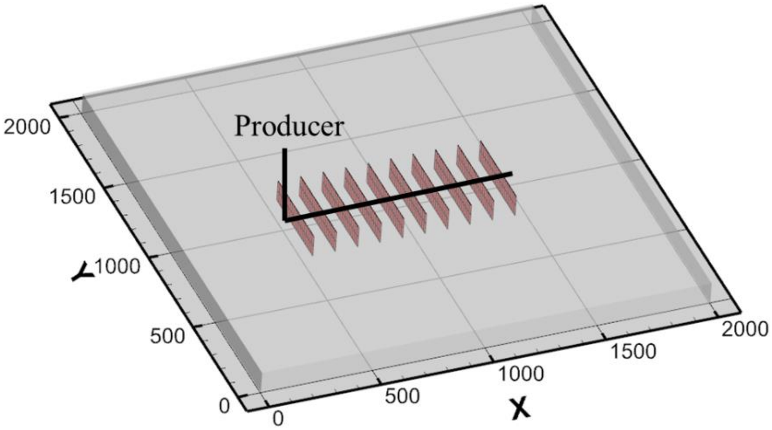

Figure 3.11 3D view of the homogeneous model with 10 hydraulic fractures

Table 3.2 Reservoir input of the homogeneous model with 10 hydraulic fractures

Parameter	Value
Reservoir size	2000×2000×100 ft^3
Initial pressure	6000 psi
Matrix porosity	0.1
Matrix permeability	0.0001 md
Rock compressibility(p_{init})	1.0×10^{-6} psi^{-1}
HF porosity	0.25
HF conductivity	500 md.ft
HF height	100 ft
HF half-length	200 ft
HF spacing	100 ft

In Figure 3.13, we first compare the w(τ) function of each discretization scheme. As we mentioned before, the w(τ) function directly controls the 1D simulation result, which serves as one criteria for the comparison. From Figure 3.13(b), all discretization schemes give very similar w(τ) function and we can clearly see the different flow regimes. The first flow regime is the pressure front propagation inside the fractures, followed by the formation linear flow and fracture interference. At the late time, we can identify the pseudo-radial flow and the boundary dominant flow at the end. To further compare the accuracy of the w(τ) function, we calculate the w(τ) function relative error defined as:

$$\mathrm{Re}\,lative\ Error\left(\%\right)=\frac{\left\|w\left(\tau\right)-w\left(\tau\right)_{ref}\right\|_1}{\left\|w\left(\tau\right)\right\|_1} \tag{3.9}$$

From Figure 3.13(c), we can clearly see the relative error of the w(τ) function increases with fewer points in the discretization scheme. However, even for the LGR 15 points scheme, the relative error is less than 0.5%. This is the reason when we compare the production profile of different discretization schemes in Figure 3.14 the results are almost identical.

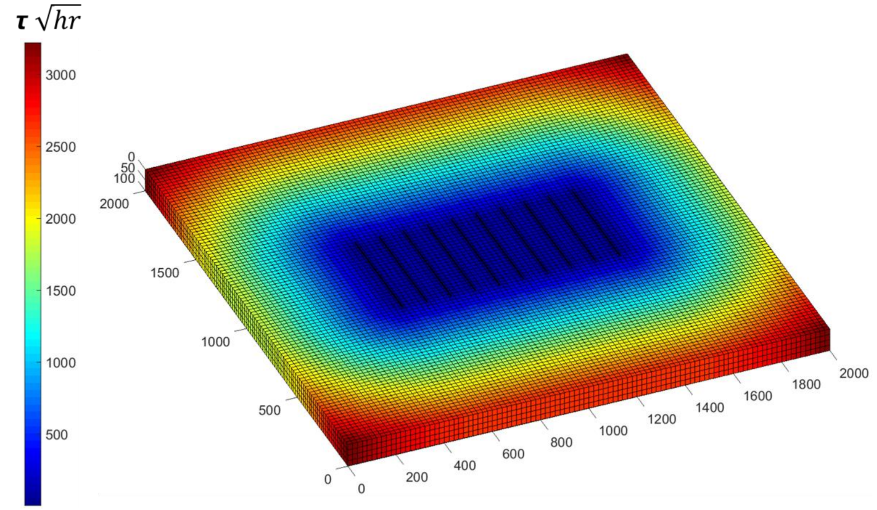

Figure 3.12 DTOF contour using LGR 27 points scheme

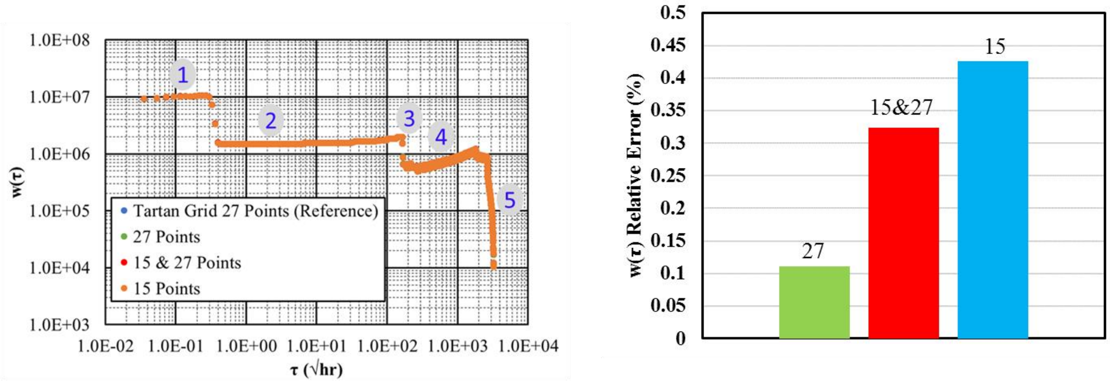

(a)

(b)

Figure 3.13 w(τ) function comparison of different discretization scheme (a) w(τ) function (b) w(τ) function relative error

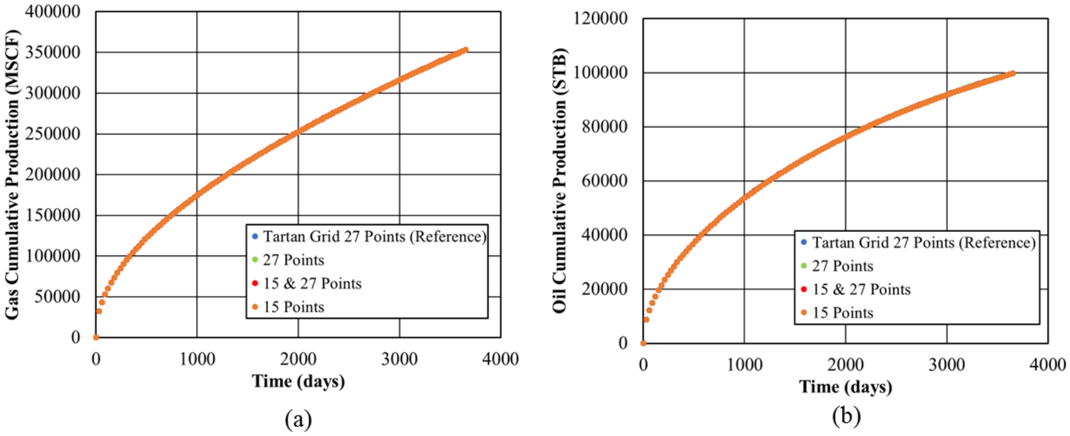

Figure 3.14 Production comparison of different discretization schemes (a) Gas cumulative production (b) Oil cumulative production

The next test models are heterogeneous reservoirs with 10 hydraulic fractures. Here we use the Dykstra-Parsons coefficient (V_{DP}) to respresent the reservoir heterogeneity (Dykstra and Parsons 1950; Jensen et al. 2000). V_{DP} is a dimensionless coefficient, which is defined as:

$$V_{DP} = \frac{k_{50} - k_{84.1}}{k_{50}} \tag{3.10}$$

where k_{50} is the median permeability and $k_{84.1}$ is the permeability at one standard deviation of the permeability distribution. The V_{DP} ranges from 0 to 1. The V_{DP} of a homogeneous reservoir is 0 and the V_{DP} of a highly heterogeneous reservoir is 1. Most reservoirs have V_{DP} between 0.4 and 0.9. To further compare the accuracy of different discretization schemes, we construct 3 heterogeneous reservoirs with V_{DP} equal to 0.4, 0.6, and 0.8. The permeability fields are given in Figure 3.15. Other input parameters are same as the homogeneous model in Table 3.2.

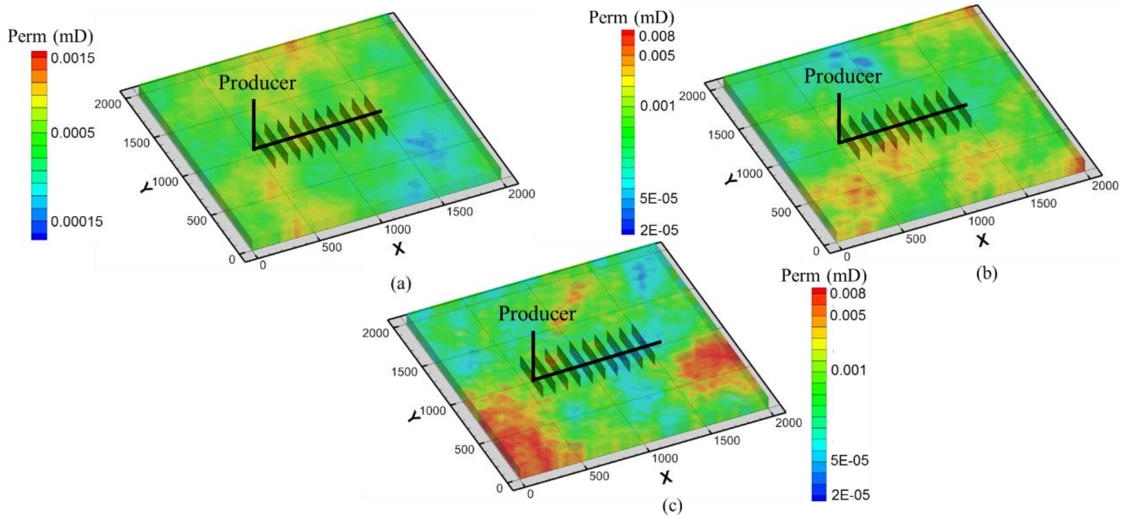

Figure 3.15 Permeability field of the heterogeneous models (a) V_{DP}=0.4 (b) V_{DP}=0.6 (c) V_{DP}=0.8

In Figure 3.16, we show the DTOF contours for the different V_{DP} values. From the results, the reservoir heterogeneity has significant impact on the DTOF. With increasing V_{DP} value, the DTOF contours become more twisted because of the reservoir heterogeneity.

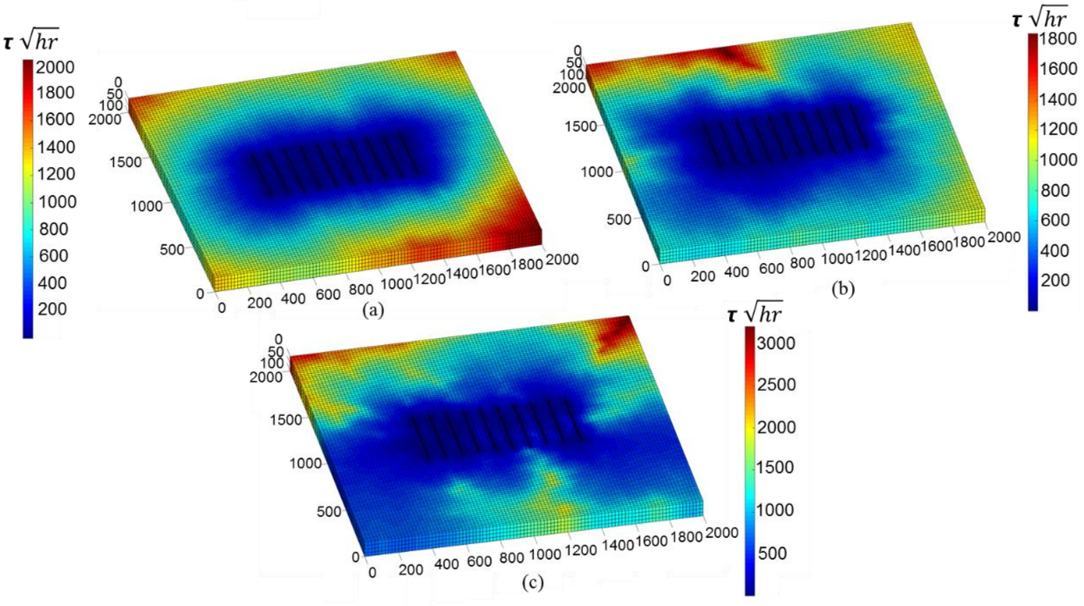

Figure 3.16 DTOF contour using LGR 27 points scheme (a) V_{DP}=0.4 (b) V_{DP}=0.6 (c) V_{DP}=0.8

Figure 3.17 provides the accuracy of different discretization schemes for different V_{DP} values. We use relative error of w(τ) function and cumulative oil production as two criteria. As before, we use tartan grid 27 points scheme as the reference result. From Figure 3.17, the LGR 27 points scheme gives very small relative error of w(τ) function and negligible cumulative production relative error even at the high V_{DP} scenario. This result again demonstrates the accuracy of the LGR workflow. For LGR 15&27 points scheme and LGR 15 points scheme, only at very high V_{DP} scenario we can see the discrepancy on the w(τ) function and cumulative production. At low V_{DP} scenario, the lower resolution discretization schemes also give reasonable results. Therefore, we can clearly see the tradeoff between accuracy and efficiency here. When the V_{DP} value is low, LGR 15&27

points scheme or LGR 15 points scheme can give us reasonable results. When the V_{DP} value is high, it is better to turn to the high-resolution discretization scheme.

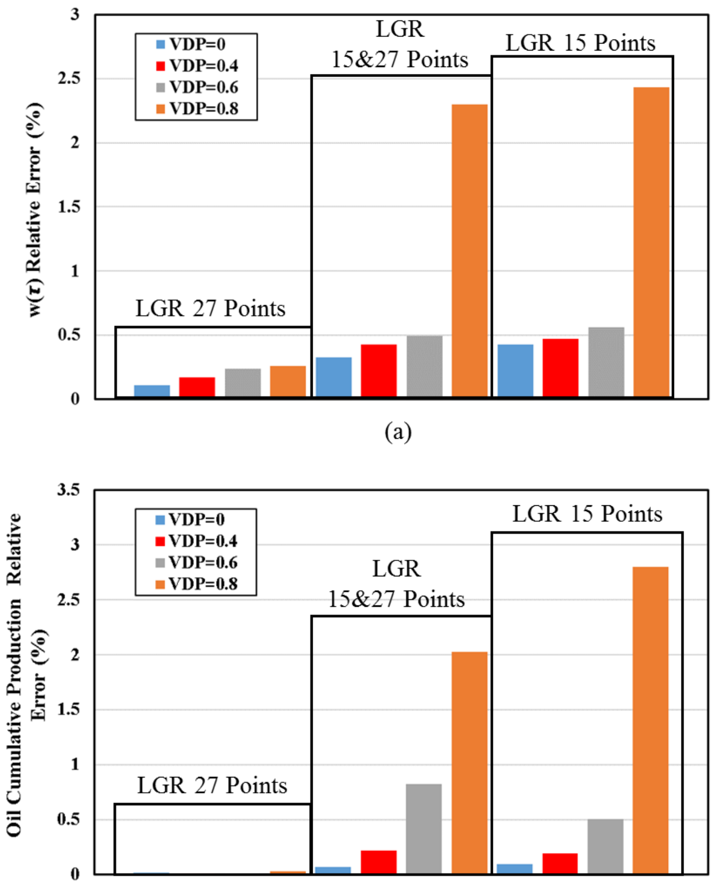

(a)

(b)

Figure 3.17 Comparison of different discretization schemes under different V_{DP} values (a) w(τ) function relative error (b) Oil cumulative production relative error at 10 years

3.3.2.5 Computational Efficiency

Computational efficiency of the LGR method is also studied. Figure 3.18 shows the CPU time and speedup ratio of different discretization schemes vs. number of hydraulic fractures. With the increasing of number of hydraulic fractures, the CPU time of the LGR method slightly goes up while the CPU time for tartan grid method dramatically increases. This again demonstrates the advantage of the LGR method. This phenomenon can also be seen from the speedup ratio. In addition, as expected the speedup ratios of LGR 15 points scheme or LGR 15&27 points scheme are larger than LGR 27 points. The reason can be found in Table 3.3. For 27 points scheme, there are 8 unknowns per cell while for 15 points scheme, the number is down to 4.

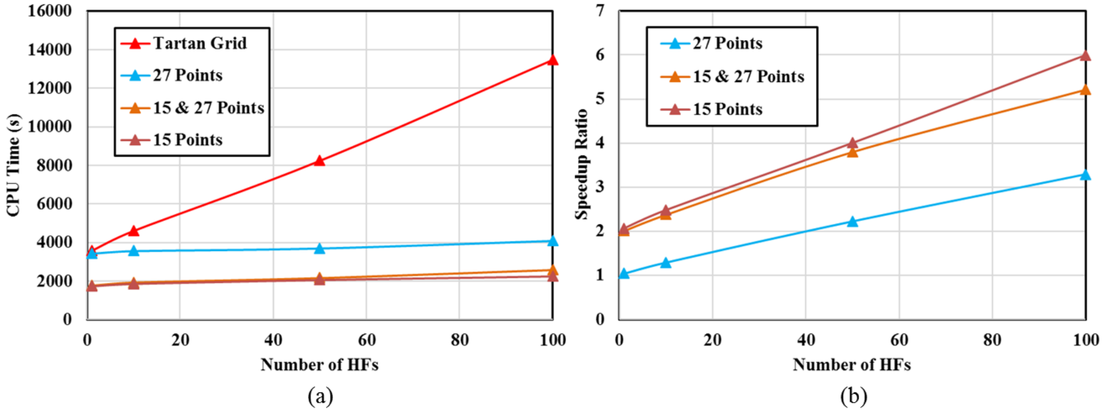

(a) (b)

Figure 3.18 Comparison of CPU time (a) and Speedup ratio (b) of different discretization schemes

Table 3.3 Unknowns per cell of different discretization schemes

Scheme	Unknowns per cell
27 Points	Cell center: 1 Face center: $\frac{1}{2}\times 6$ Edge center: $\frac{1}{4}\times 12$ Vertex: $\frac{1}{8}\times 8$ Total: 8
15 Points	Cell center: 1 Face center: $\frac{1}{2}\times 2$ Edge center: $\frac{1}{4}\times 4$ Vertex: $\frac{1}{8}\times 8$ Total: 4

3.4 Conclusions

In this chapter, we extend the FMM-based simulation to local grid refinements. We discuss the entire workflow in detail, including the grid generation, local Eikonal solver and 1D simulation. We use different models to validate the workflow. In addition, we test different discretization schemes and compare their efficiencies and accuracies. Some key conclusions from this paper are summarized as follows:

- We demonstrate the feasibility of the FMM-based simulation with LGRs. This workflow gives the same resolution as the tartan grid method. However, it leads to significantly faster computation time, especially in the presence of large number of hydraulic fractures.
- Different discretization schemes are tested for matrix and fracture domains. When the V_{DP} value is low, hybrid LGR 15&27 points scheme or lower resolution LGR

15 points scheme can give us reasonable results. When the V_{DP} value is high, it is recommended to use high-resolution 27 points discretization scheme.

CHAPTER IV

MODELING HYDRAULICALLY FRACTURED SHALE WELLS USING THE FAST MARCHING METHOD WITH EMBEDDED DISCRETE FRACTURE MODEL (EDFM)

4.1 Chapter Summary

Nowadays, the industrial trend of hydraulic fracturing is to generate complex fracture networks. This can be achieved by reducing the cluster spacing while increasing the fluid and proppant usage. In addition, many unconventional reservoirs contain existing natural fractures. The interactions between the hydraulic fractures and the natural fractures could also induce the complex fracture networks. In this chapter, we focus on extending the FMM-based simulation to incorporate embedded discrete fracture model (EDFM) to simulate the complex fracture networks.

Similar to the LGRs workflow in Chapter III, FMM with EDFM workflow also requires novel gridding to link the embedded discrete fractures and the matrix using Delaunay triangulation. The 'diffusive time of flight' is calculated based on Eulerian discretization in unstructured grids. Using the 'diffusive time of flight (DTOF)' as a spatial coordinate, the FMM-based flow simulation reduces 3D complex fracture networks simulation to an equivalent 1D simulation.

We first validate the accuracy of the FMM-based simulation with EDFM by comparing with tartan grids and EDFM with finite difference simulation. The FMM-based simulation with EDFM shows good agreement with other methods. Then, we apply the

FMM-based simulation with EDFM to a multi-stage horizontal well and compare with FMM with unstructured grid. The hydraulic fractures are intersecting with several natural fractures. The FMM with EDFM can simulate arbitrary fracture patterns without simplification and shows good accuracy and efficiency compared with FMM with unstructured grid.

This study demonstrates the feasibility of the FMM-based simulation with EDFM for simulating complex fracture networks. The contributions of this study are: (i) utilizing Delaunay triangulation to link the embedded discrete fractures and the matrix domain (ii) diffusive time of flight calculations in the two domains using the unstructured grid framework.

4.2 Background

EDFM approach has drawn significant attention in recent years because of its feasibility to handle complex hydraulic fracture networks with relatively good efficiency. This method was first proposed by Li and Lee (2008). Recently, many researchers have used this method to do further application at the field scale level (Moinfar et al. 2014; Du et al. 2017; Yu et al. 2018) and also proposed some modified equations to improve the original EDFM approach (Jiang and Younis 2016; Ren et al. 2017; Yang et al. 2018; Xue et al. 2019). The main idea of EDFM approach is to maintain the underlying matrix grid and use additional grid blocks to represent the fractures. The non-neighboring connections (NNC) are used to connect between the matrix grid and the corresponding fractures.

In Chapter III, we proposed the FMM-based simulation with LGRs. However, this method cannot simulate arbitrary fracture patterns. In this chapter, we extend the FMM-based simulation with EDFM to simulate complex fracture networks. This chapter is organized as follows. We begin with the details of the FMM-based simulation with EDFM, including mesh generation and validation with tartan grid method. Further, we will discuss the comparison of FMM-based simulation with EDFM and unstructured grid.

4.3 Methodology

4.3.1 EDFM Grid Generation

The EDFM grid generation consists of three steps. First, based on the location of the hydraulic fractures, we determine the intersection points between matrix-fracture as well as fracture-fracture. Second, within each matrix cell with fractures, we generate local triangles based on the intersection points using Delaunay triangulation. Special treatment is needed for the matrix cell next to the fracture tips. Third, we build the 2.5D grid based on the 2D triangles by assembling multiple layers and allowing for vertical thickness variation.

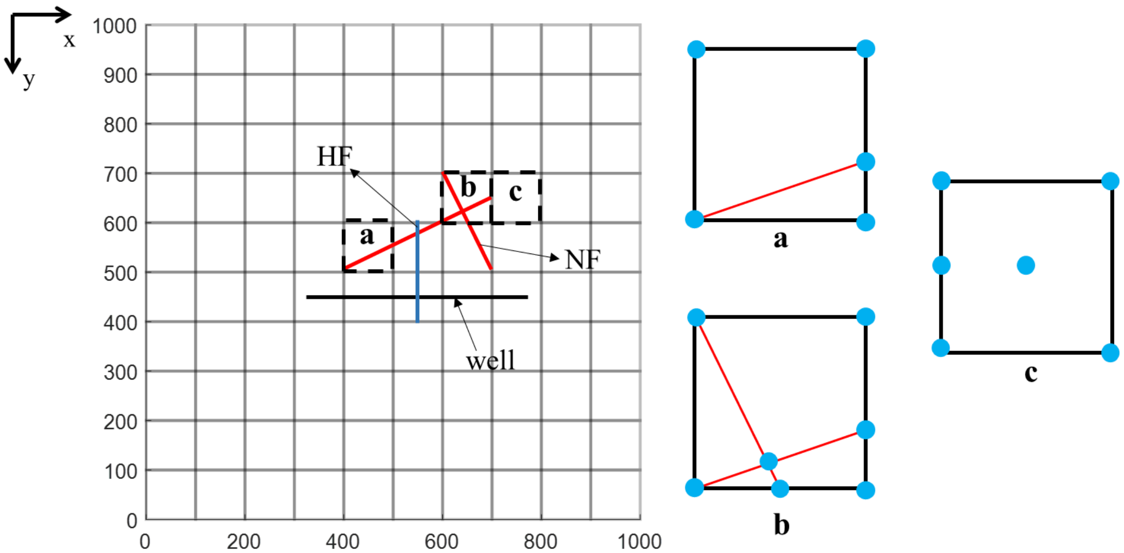

Figure 4.1 EDFM grid generation: Identify the intersection points between matrix-fracture and fracture-fracture

The first step of the EDFM grid generation is to identify the intersection points between matrix-fracture and fracture-fracture. These intersection points serve as the basis to further generate the 2D triangles. In Figure 4.1, we show an example of a 1000ft×1000ft reservoir with 1 hydraulic fracture and 2 natural fractures. Since we need to update the DTOF at the corner points of the matrix cell as well as the intersection points between matrix-fracture and fracture-fracture, these points are identified as blue dots in Figure 4.1. Special treatment is needed for the matrix cell next to the fracture tips, such as cell ‘c’ in Figure 4.1. Although there are no fractures inside this cell, we have to account for the fracture tips by adding one blue dot at the edge of the cell. For the matrix cell without fractures, we use the 5 points discretization scheme. Hence, an additional blue dot is added at the center point of cell ‘c’.

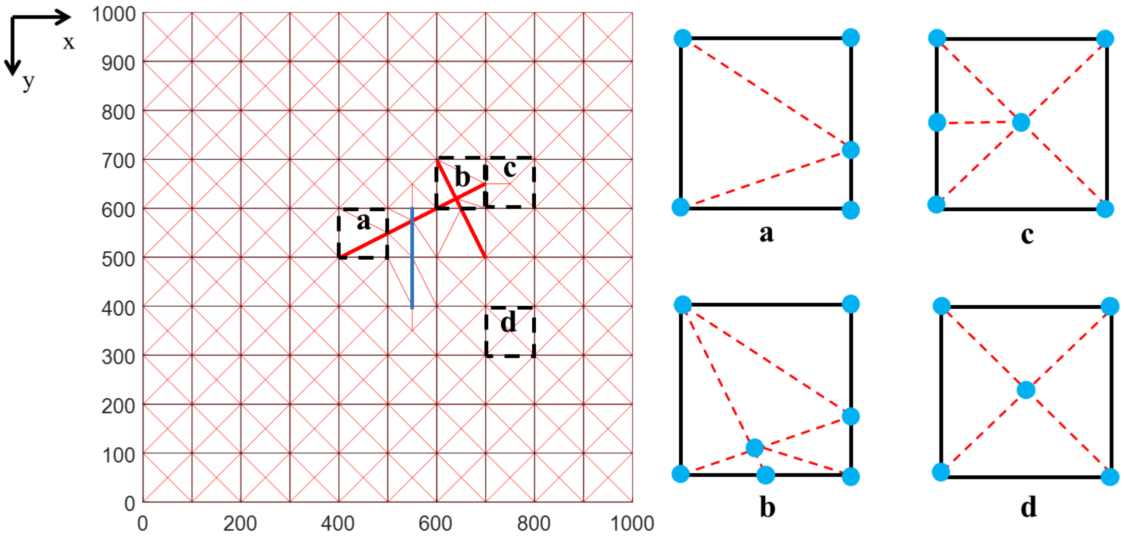

Figure 4.2 EDFM grid generation: 2D triangles generated using Delaunay triangulation

The second step is to generate the 2D triangles based on the intersection points from step one. Here, the Delaunay triangulation is adopted to generate the 2D triangles (Ruppert 1995; Shewchuk 1996). For the matrix cell without fractures, we use 5 points discretization scheme.

The third step is same as the LGRs grid generation. We build the 2.5D grid based on the 2D triangles. Figure 4.3 shows the final 2.5D grid of this example. For the DTOF calculation, we still use the local Eikonal solver based on Eulerian discretization as discussed before. The difference is that the fracture cells are embedded in the matrix as high conductive paths for pressure propagation and we solve the DTOF inside the fractures using 1D approximation. The DTOF in the matrix follows the same procedure as the LGR method.

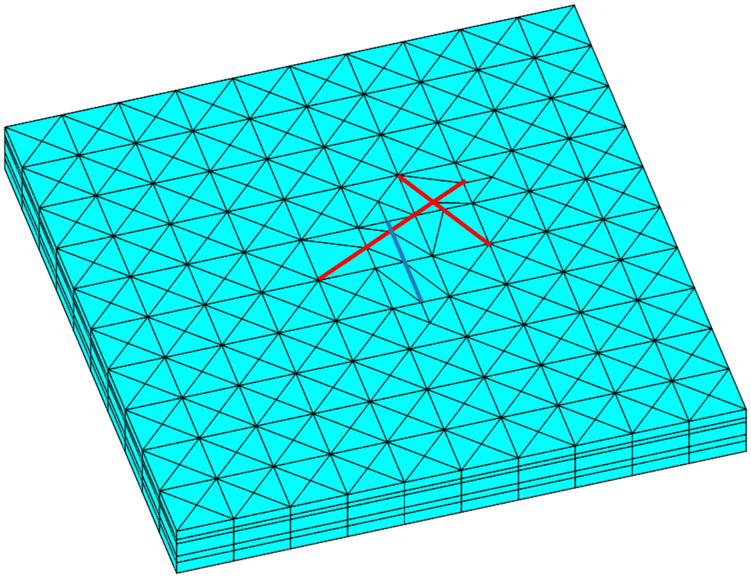

Figure 4.3 EDFM grid generation: 2.5D grid generation

4.3.2 Workflow Validation

We begin the validation using a simple example. This model has 1 hydraulic fracture and 2 natural fractures intersecting each other. The hydraulic fracture’s conductivity is 500 md.ft while the natural fracture’s conductivity is 2 md.ft. The producer is completed at the middle of the hydraulic fractures. Figure 4.4 gives the 3D view of this model and Table 4.1 shows the parameters to generate this model. Since the fractures are aligned with the grid system, we can use tartan grid method as our reference result.

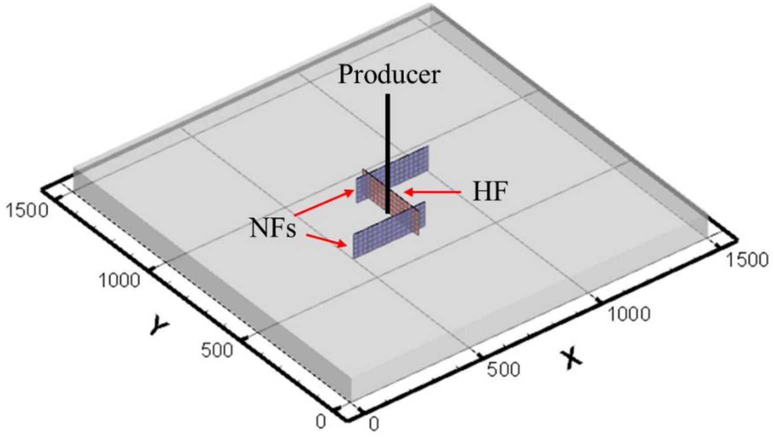

Figure 4.4 3D view of the synthetic model with 1 hydraulic fracture and 2 natural fractures

Table 4.1 Reservoir input of the model with 1 hydraulic fracture and 2 natural fractures

Parameter	Value
Reservoir size	1500×1500×100 ft^3
Initial pressure	6000 psi
Matrix porosity	0.12
Matrix permeability	0.001 md
Rock compressibility(p_{init})	1.0×10^{-6} psi^{-1}
HF porosity	0.25
HF conductivity	500 md.ft
HF height	100 ft
HF half-length	150 ft
NF conductivity	2 md.ft

The DTOF contours comparison is given in Figure 4.5 and the w(τ) functions are compared in Figure 4.6. From the w(τ) plot, the FMM with EDFM and FMM with tartan grid give similar w(τ) results, which demonstrate the accuracy of the FMM with EDFM workflow. From the w(τ) plot, we can readily identify different flow regimes. We can find the early time fracture flow and formation linear flow as well as the late time radial flow and boundary dominant flow. Figure 4.7 provides the production comparison of different methods. Here, we compare the tartan grid and EDFM using finite difference simulation with tartan grid and EDFM using FMM. From the results, the FMM-based methods provide good match with the finite difference based methods. For the CPU time comparison, which is shown in Figure 4.8, we can see that the FMM with EDFM is faster compared to the tartan grid simulation.

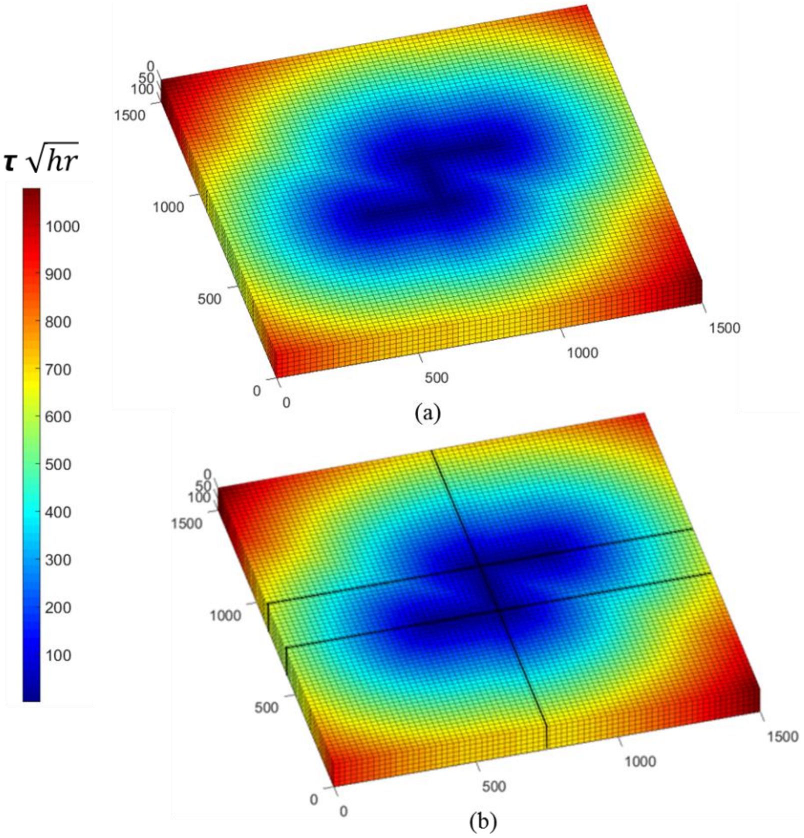

Figure 4.5 Validation of the FMM with EDFM: (a) DTOF contour from EDFM (b) DTOF contour from tartan grid

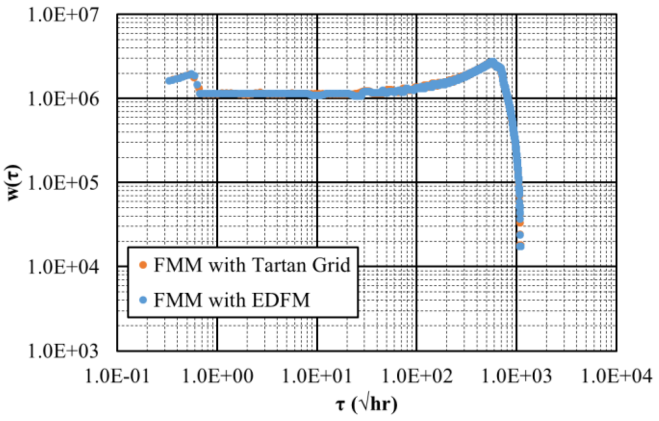

Figure 4.6 w(τ) function comparison

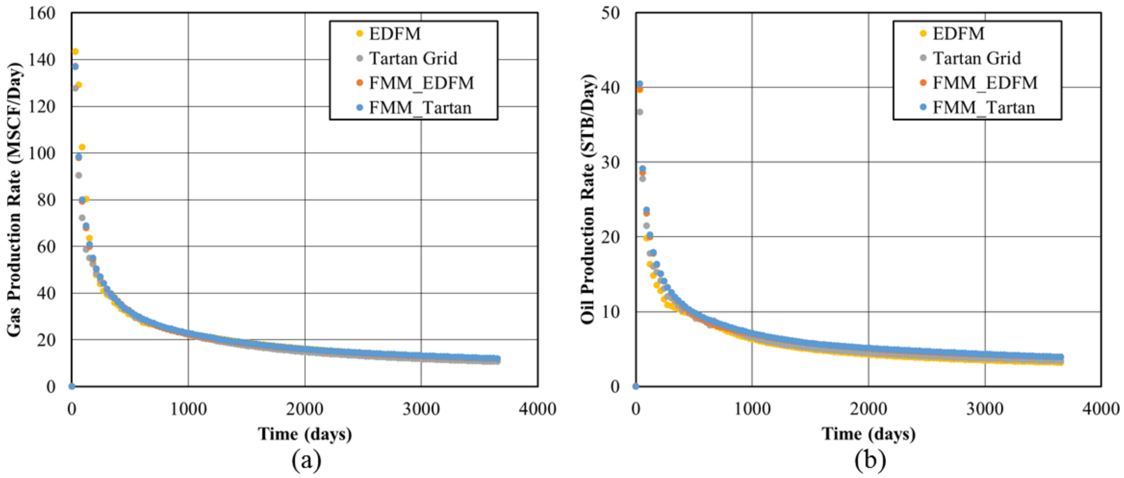

Figure 4.7 Comparison of production profile of different methods (a) Gas production rate (b) Oil production rate

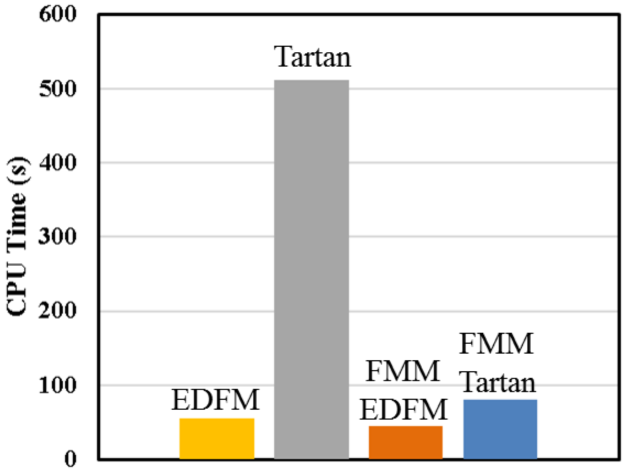

Figure 4.8 Comparison of CPU time of different methods

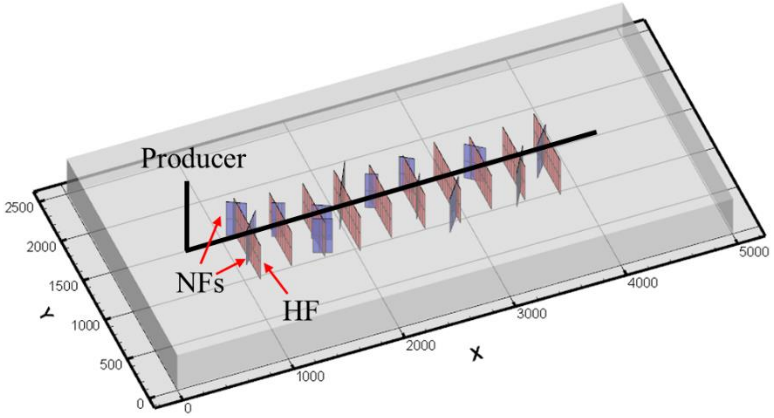

Figure 4.9 3D view of the synthetic model with 10 hydraulic fracture and multiple natural fractures

The second validation case contains 10 hydraulic fractures with multiple natural fractures intersecting each other. We still use 500 md.ft for the hydraulic fracture's conductivity and 2 md.ft for the natural fracture's conductivity. The fluid model is single-phase gas. The horizontal producer is completed at all the hydraulic fractures. The 3D view of this example is given in Figure 4.9 and the input parameters are shown in Table 4.2.

Table 4.2 Reservoir input of the model with 10 hydraulic fractures with multiple natural fractures

Parameter	Value
Reservoir size	5000×2500×100 ft^3
Initial pressure	4000 psi
Matrix porosity	0.046
Matrix permeability	0.0001 md
Rock compressibility(p_{init})	1.0×10^{-6} psi^{-1}
HF porosity	0.25
HF conductivity	500 md.ft
HF height	250, 300 ft
HF half-length	150 ft
NF conductivity	2 md.ft

Figure 4.10 compares the 2D triangles grid generated by the unstructured grid method with the EDFM method. Here, we can clearly see the advantage of the EDFM method. At the fracture locations, the unstructured grid method generates multiple tiny cells to capture the fracture geometry. For the EDFM method, we use the simple straight lines to represent the hydraulic fractures and the triangles to connect between fracture and matrix.

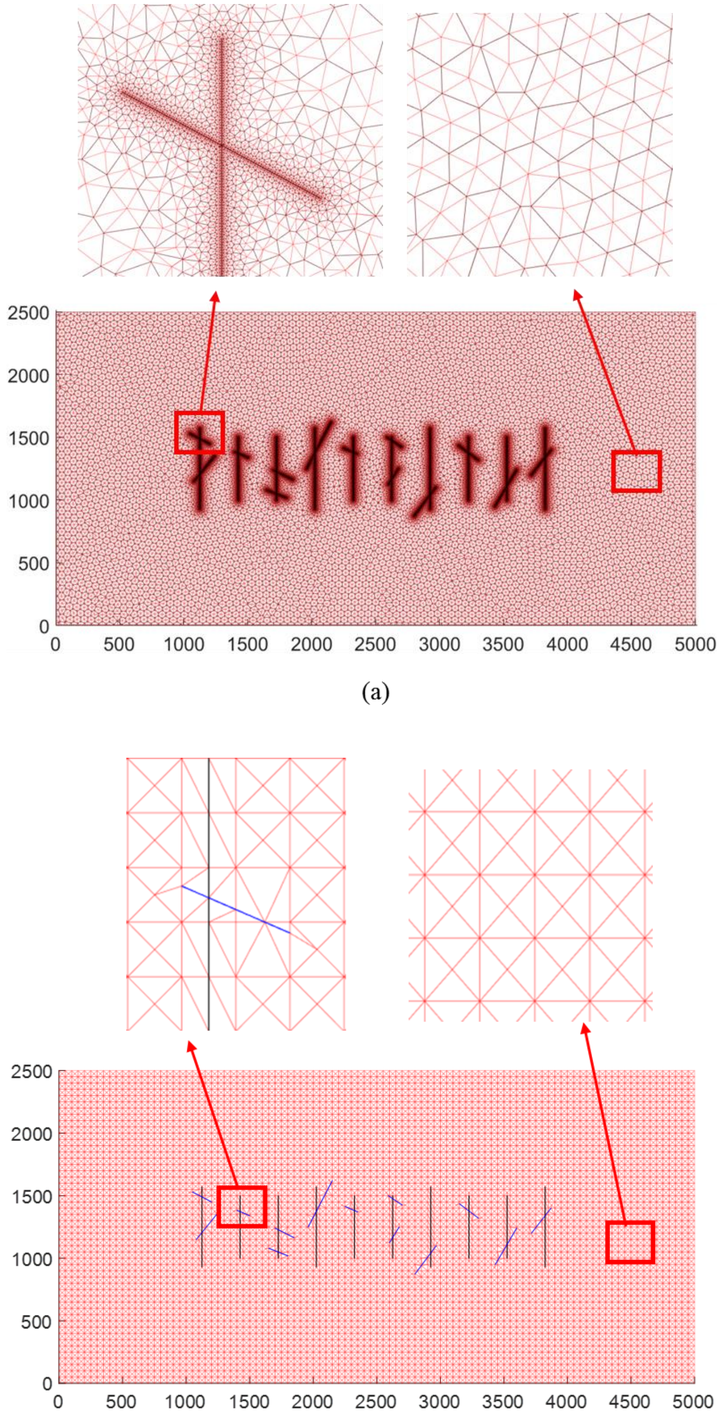

(a)

(b)

Figure 4.10 2D triangles grid generation (a) Unstructured grid method (b) EDFM method

In Figure 4.11, we further compare the two methods. Figure 4.11(a) shows the CPU time to generate the grid of this case. The EDFM method is an order of magnitude faster than the unstructured grid method. Since multiple tiny cells are generated by the unstructured grid method, the cell number of EDFM method is much smaller than the unstructured grid method, which is shown in Figure 4.11(b). For this reason, the EDFM method uses much shorter time than the unstructured grid method for the DTOF calculation, which is illustrated in Figure 4.11(c).

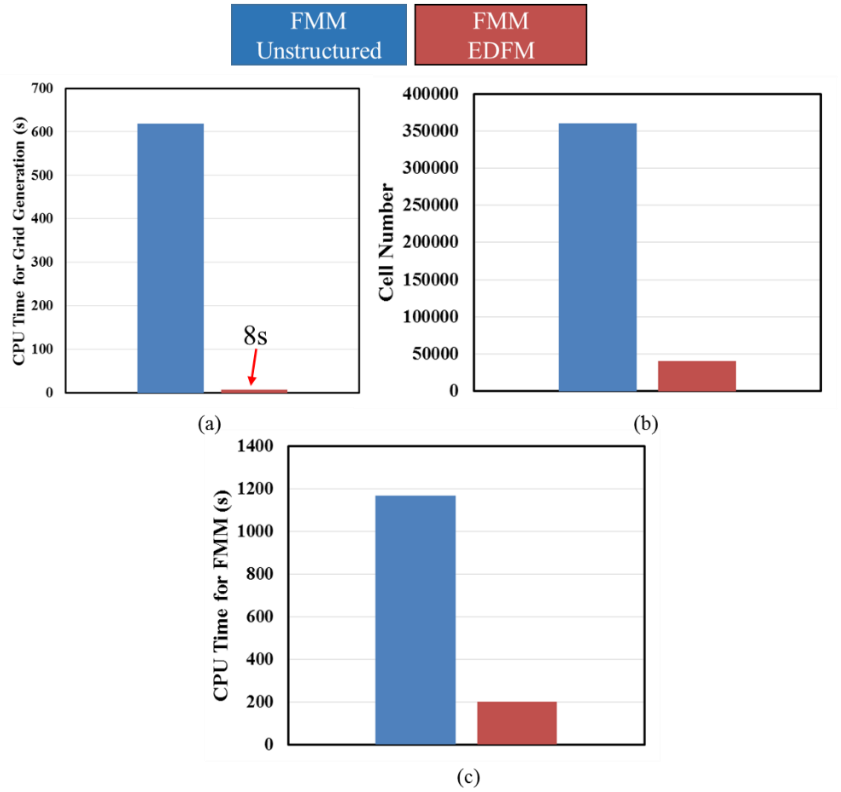

Figure 4.11 Comparison of FMM with unstructured grid and FMM with EDFM (a) CPU time for grid generation (b) Cell number (c) CPU time for FMM calculation

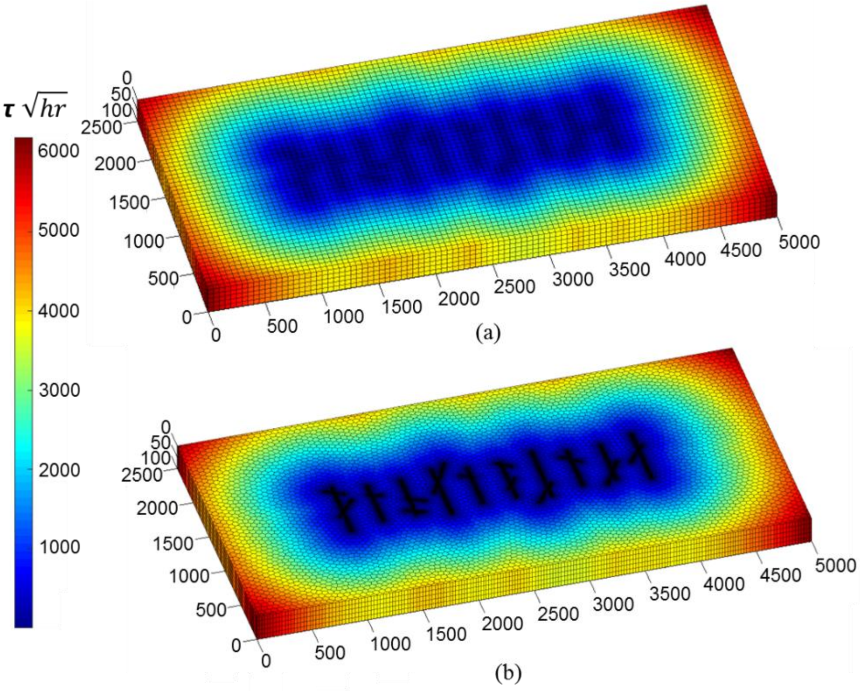

Figure 4.12 DTOF comparison (a) FMM with EDFM (b) FMM with unstructured grid

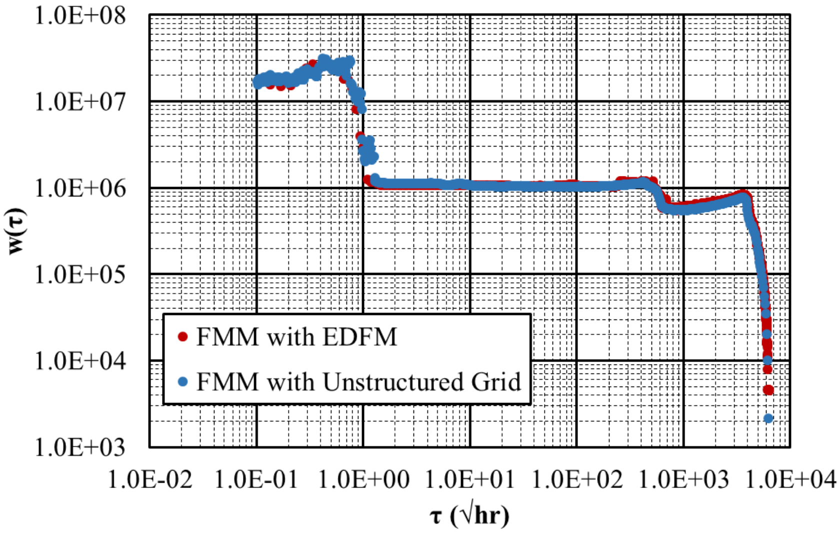

Figure 4.13 w(τ) function comparison

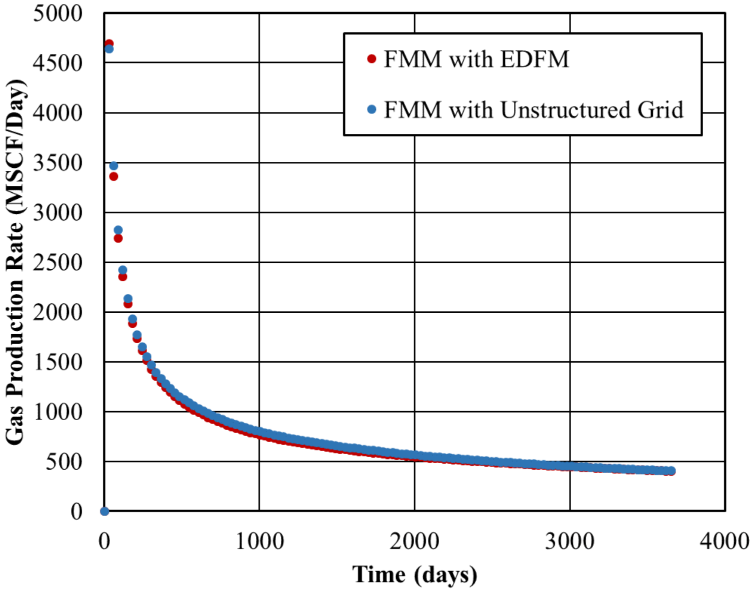

Figure 4.14 Comparison of gas production profile of different methods

In Figure 4.12 and Figure 4.13, we compare the DTOF and w(τ) function calculated using the two methods. Figure 4.12(a) and (b) give the DTOF contours calculated by the EDFM and unstructured grid method. From the plots, we can see a good agreement of the two methods. Figure 4.13 further compares the w(τ) function. Again, the two methods obtain very similar w(τ) function and capture all the different flow regimes. Finally, Figure 4.14 shows the 1D-simulation results using the two methods. Because we have very similar w(τ) function, the gas production rates are also very close to each other.

4.4 Conclusions

In this chapter, we extend the FMM-based simulation to embedded discrete fracture model. We discuss the entire workflow in detail and use different models to validate the workflow. This workflow can simulate arbitrary and complex fracture geometries. This workflow has similar resolution as the unstructured grid method but it is more efficient in terms of grid generation and DTOF calculations.

CHAPTER V

UNDERSTAND THE IMPACT OF TIGHTER CLUSTER SPACING ON FRACTURE DESIGNS USING THE EAGLE FORD FIELD DATA

5.1 Chapter Summary

One of the challenges in completing unconventional wells is determining the optimal cluster spacing. The spacing between perforation clusters influences the geometry of hydraulic fractures, drainage volume, production rates, and ultimate recovery of a well. This chapter aims to explain why the wells with tighter cluster spacing outperform others in Eagle Ford by calibrating the fracture geometry and properties using field injection data.

The Eagle Ford injection and production data are from two horizontal wells completed side by side. This chapter identifies the fracture geometry and properties by history matching the field injection treatment pressure using Mangrove®. The impact of cluster spacing is examined through the calibrated fracture geometry and properties. The calibrated models suggest that most of the fractures are planar in Eagle Ford. The well with wider cluster spacing tends to develop longer fractures. However, the well with tighter cluster spacing has more complex fracture networks resulting in better production performance.

This study demonstrates the feasibility of the Mangrove® on the field scale application for injection treatment pressure history matching. The calibrated fracture geometries with Eagle Ford field data can help explain the performance variation using different cluster spacing within the same reservoir. As future work, we need to history match the production data to further calibrate the fracture properties and compare the two wells.

5.2 Background

Recently, the trend of optimal hydraulic fracturing design in the industry has been reducing the cluster spacing while increasing the fluid and proppant usage. However, it is still a challenging task for characterizing the fracture networks after hydraulic fracturing to understand this phenomenon, especially at the field level.

Much research has been conducted to characterize the fracture networks and optimize the cluster spacing. On the geomechanics side, many efforts have been made to simulate and control the stress shadow effect (Kresse et al. 2012; Zhou, Z. et al. 2016; Wu et al. 2017; Tang et al. 2018a). This effect is extremely important under the tighter cluster spacing condition and it is believed to be the cause of low fracture efficiency. The stress shadow effect is induced by the stress field change from the existing hydraulic fractures. The stress field change can lead to deviation or even abortion of the nearby hydraulic fractures (Roussel et al. 2012; Simpson et al. 2016). Therefore, it is important to minimize the cluster spacing while controlling the stress shadow effects. Another negative effect for the hydraulic fracturing is the bedding effect, which limited the fracture height growth (Tang and Wu 2018b; Tang et al. 2019). It is also important to minimize the cluster spacing while finding the optimum completion position to avoid the bedding layers.

On the reservoir simulation side, some researchers focus on combining the geomechanics simulation with reservoir simulation to characterize the fracture networks and optimize the cluster spacing (Suarez and Pichon 2016; Xiong et al. 2018). This workflow often involves several steps, including generating the fracture network using geomechanics simulation, history matching production data to calibrate the fracture properties and further optimizing the cumulative production or net present value (NPV). Although this comprehensive workflow can well calibrate the fracture properties and optimize the cluster spacing, it is very challenging to conduct the entire workflow where thousands of simulations are required for the calibration and optimization process.

In this chapter, we conduct a manual history matching of the field injection treatment pressure to generate multiple realizations of fracture network using Mangrove® as the forward simulator. Then we compare the fracture geometries to explain the performance variation using different cluster spacing within the same reservoir.

5.3 Field Application: Fracture Characterization and History Matching

In this section, we begin the primary focus of this chapter, which is fracture characterization and history matching of two Eagle Ford wells to understand the impact of tighter cluster spacing on the fractures. We begin with the field data description, followed by the fracture geometry calibration using Mangrove® and manual history matching to generate three realizations of fracture geometry. Finally, we evaluate the fracture models to analyze the impact of tighter cluster spacing on the fractures.

5.3.1 Wells and Reservoir Description

The geologic model used in this study contains 4 different formations: Austin Chalk, Upper Eagle Ford, Lower Eagle Ford and Buda. Two horizontal wells are completed side by side in the lower Eagle Ford formation. The well spacing is 1200 ft, which is large enough to prevent the fracture interactions between wells. In Figure 5.1, we show the schematic diagram of the two wells locations and the reservoir. We use the layer cake model for the permeability, where each formation has a constant value. Other properties such as Young's modulus, porosity and Poisson's ratio are heterogeneous across the reservoir. In Figure 5.2, we show the 3D view of each property and summarize the property ranges in Table 5.1.

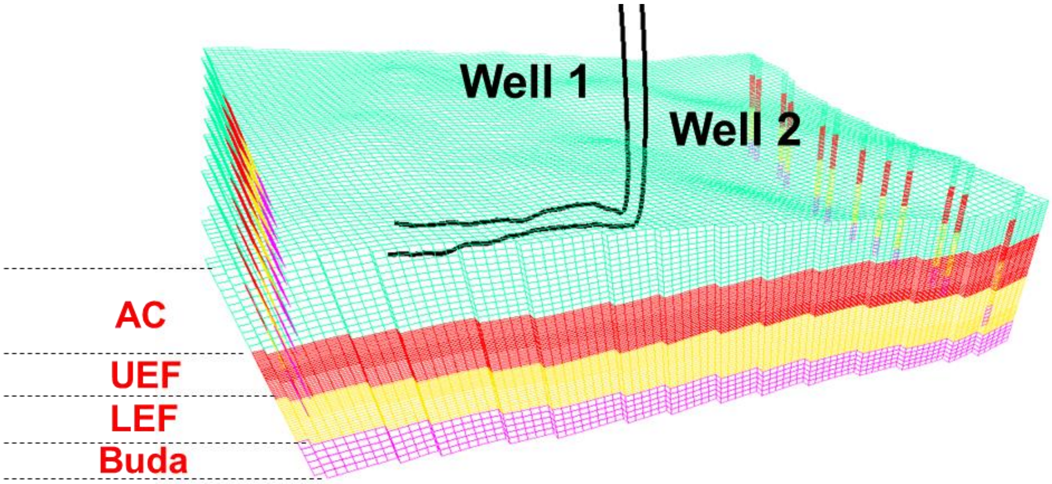

Figure 5.1 Schematic diagram of the wells location and reservoir

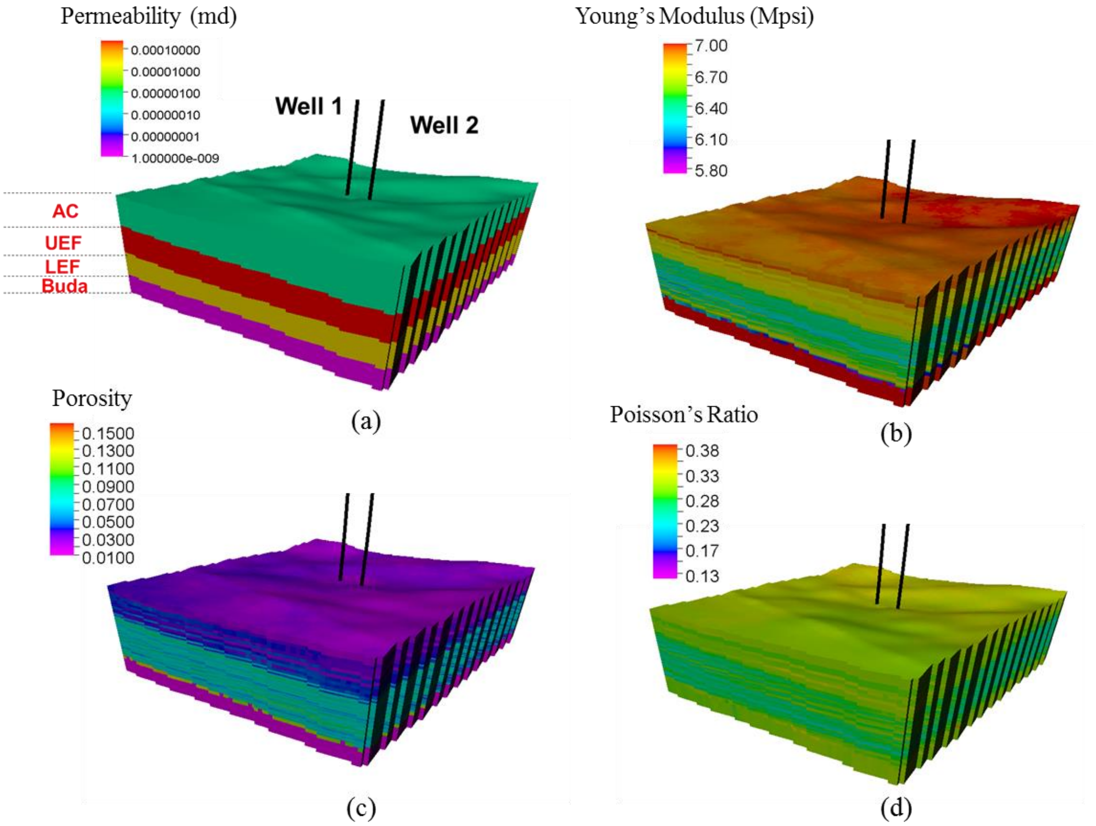

(a) (b) (c) (d)

Figure 5.2 Reservoir properties of the model (a) Permeability (b) Young's Modulus (c) Porosity (d) Poisson's Ratio

Table 5.1 Property ranges in different formations

Property	Austin Chalk	Upper Eagle Ford	Lower Eagle Ford	Buda
Permeability (nd)	0.5	230	30	0.001
Porosity	0.01-0.05	0.01-0.09	0.01-0.11	0.01-0.16
Young's Modulus (Mpsi)	6.58-7.03	5.99-6.87	6.09-6.91	5.75-7.13
Poisson's Ratio	0.27-0.34	0.21-0.34	0.21-0.31	0.12-0.38

In Table 5.2, we summarize the two wells completion information. From Table 5.2, we can clearly see that well 2 has a much tighter cluster spacing than well 1. The total numbers of perforations per cluster are the same for both wells. The two wells use the same type of fracturing fluid and proppant but with different weight or volume. This is a unique field pilot test to investigate the influence of tighter cluster spacing on the fractures and well performance.

Table 5.2 Two wells completion data

Well Name	Well 1	Well 2
Cluster Spacing (ft)	50	20
Cluster Count per Stage	5	10
No. of Stages	26	31
No. of Perfs per Cluster	6	3
Mass of Proppant (lb)	10,000,000	13,000,000
Type of Proppant	100 Mesh, 40/70 White	100 Mesh, 40/70 White
Volume of Fluid (bbl)	150,000	350,000
Type of Frac Fluid	Slickwater, HCl 7.5, 8# vis-link	Slickwater, HCl 7.5, 8# vis-link

5.3.2 Two-Well Production Data

The three-phase production and the bottomhole pressure data are available for one year. In Figure 5.3, we provide the production data of the two wells. From the plot, we can clearly see that well 2 has better performance than well 1 in terms of oil and gas production. The two wells both have high water production at the early time from the flow back fluids.

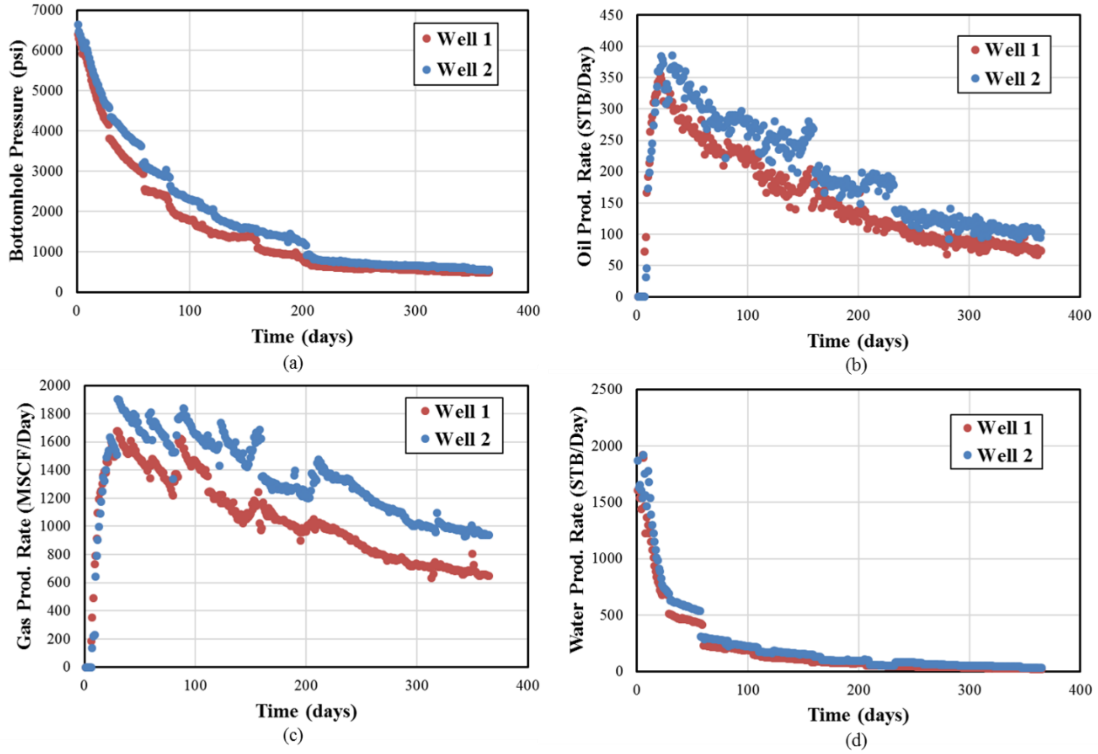

Figure 5.3 Two wells production data (a) Bottomhole pressure (b) Oil production rate (c) Gas production rate (d) Water production rate

5.3.3 Fracture Geometry Calibration using Injection Treatment Pressure

In this section, we perform the manual history matching of the injection treatment pressure to calibrate the fracture geometry. We use the Mangrove® as the forward simulator. We first conduct a sensitivity study to identify the heavy hitters, which will be altered to match the observed injection treatment pressure. In Table 5.3, we show the base case input. All these properties are typical Eagle Ford values provided by the operator. We can see a relatively large stress anisotropy between S_{Hmax} and S_{Hmin}, which is the reason the fractures in the Eagle Ford formation are relatively straight and planar.

Table 5.3 Fracture propagation base case input

Parameter	Value
Minimum Horizontal Stress	0.85 psi/ft
Stress Anisotropy (S_{Hmax}/S_{Hmin})	1.4
Leak-off Coefficient	7.5e-4 ft/min^1/2
Fracture Height H_f	450 ft
Young's Modulus	Spatially Heterogeneous
Poisson's Ratio	Spatially Heterogeneous

The injection treatment pressure misfit is calculated using the following equation:

$$obj = \log\left(\sum_{j=1}^{2}\sqrt{\sum_{i=1}^{Ntime}(ITP_{i,j}^{obs} - ITP_{i,j}^{cal})^2}\right) \tag{5.1}$$

Here, N_{time} is the total number of pressure data observation times, *ITP* is the injection treatment pressure, the superscript *obs* indicates the observed data, and the superscript *cal* indicates the calculated value from the simulation.

Figure 5.4 shows the calculated sensitivity of the injection treatment pressure misfit to different parameters. From the plot, the most sensitive parameters are the fracture height and the leak off coefficient multiplier, followed by the minimum horizontal stress gradient. For the manual history matching process, we only alter the fracture height and the leak off coefficient multiplier since they are the heavy hitters from the sensitivity studies and the minimum horizontal stress gradient has much smaller uncertainty than the fracture height and leak off coefficient multiplier.

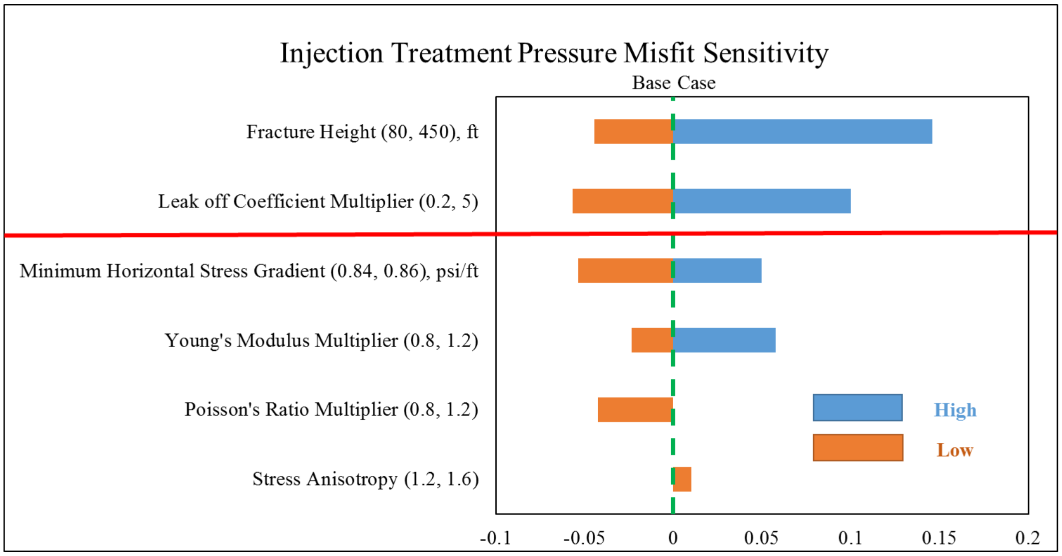

Figure 5.4 Injection treatment pressure sensitivity

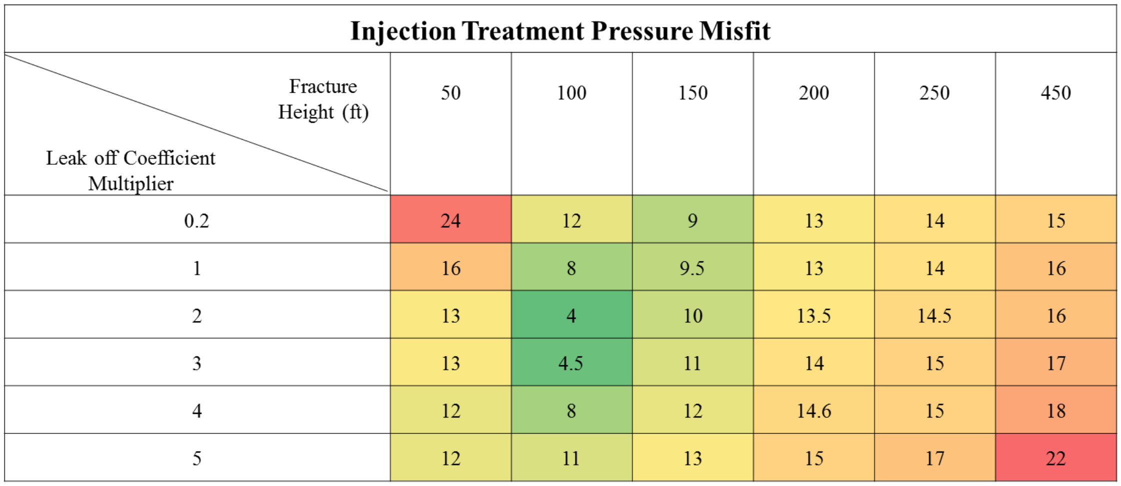

Injection Treatment Pressure Misfit

Fracture Height (ft) / Leak off Coefficient Multiplier	50	100	150	200	250	450
0.2	24	12	9	13	14	15
1	16	8	9.5	13	14	16
2	13	4	10	13.5	14.5	16
3	13	4.5	11	14	15	17
4	12	8	12	14.6	15	18
5	12	11	13	15	17	22

Figure 5.5 Manual history matching matrix

Figure 5.5 gives the manual history matching matrix of the injection treatment pressure misfit. Using this matrix plot, we can easily identify the parameter ranges of the fracture height and the leak off coefficient multiplier to achieve a relatively low misfit value. From this plot, we can see that the fracture height should be around 100ft and the leak off coefficient multiplier should be between 2 and 3, which is the dark green region in this plot. Within the parameter ranges of the fracture height and the leak off coefficient multiplier, we conduct the fine-tuning of the two parameters to further decrease the misfit value. In Figure 5.6, we show the initial results of the injection treatment pressure for well 1 and 2 where we can identify a huge discrepancy between observation and simulation results. In Figure 5.7, we illustrate the final matched results of the two wells. We finally generate 3 fracture models with fracture heights equal to 80, 100 and 120ft with different leak-off coefficient multipliers, which are shown in Figure 5.8. From the results, most of the fractures are planar in Eagle Ford due to large stress anisotropy. The well with wider cluster spacing develops longer fractures in all of the three scenarios. However, the well with tighter cluster spacing has more complex fracture networks. This result can also be seen in the w(τ) plot, which is shown in Figure 5.9. Since well 2 has more complex fracture networks, it has higher w(τ) value, which indicates larger fracture surface area.

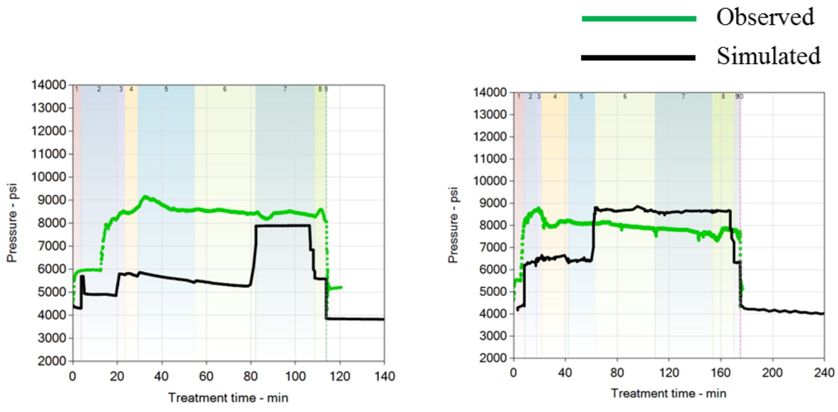

(a) (b)

Figure 5.6 Initial results of the injection treatment pressure (a) Well 1 (b) Well 2

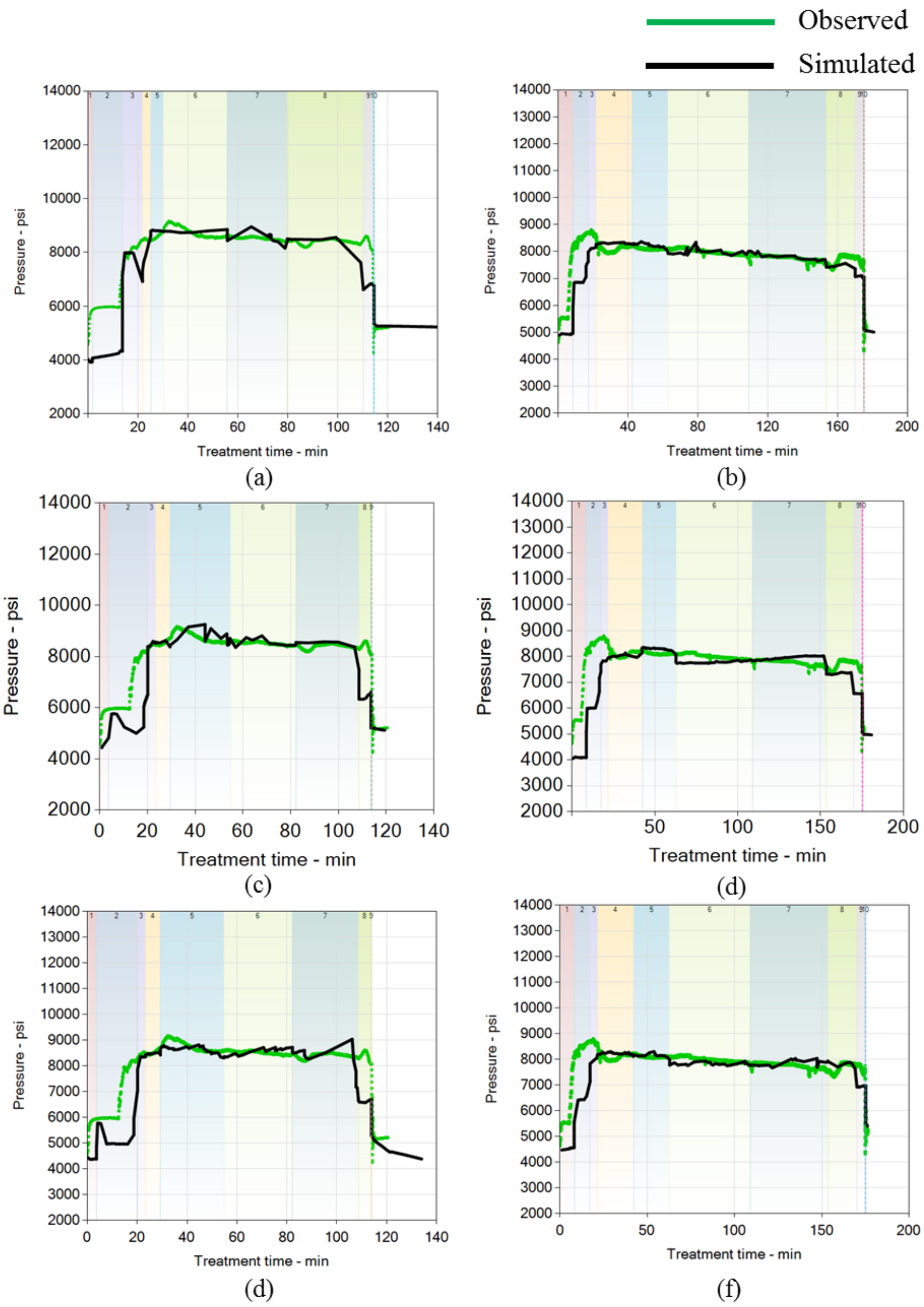

Figure 5.7 Matched results of the injection treatment pressure (a) Well 1 H_f=120ft Leak-off Multiplier=2 (b) Well 2 H_f=120ft Leak-off Multiplier=2 (c) Well 1 H_f=100ft Leak-off Multiplier=2.6 (d) Well 2 H_f=100ft Leak-off Multiplier=2.6 (e) Well 1 H_f=80ft Leak-off Multiplier=3 (f) Well 2 H_f=80ft Leak-off Multiplier=3

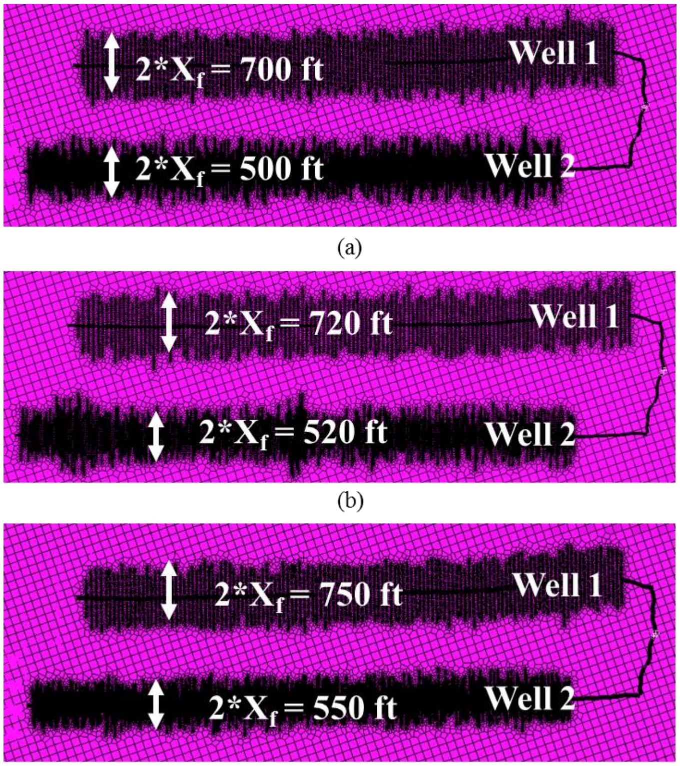

(a)

(b)

(c)

Figure 5.8 Fracture models after fracture geometry calibration (a) H_f=120ft (b) H_f=100ft (c) H_f=80ft

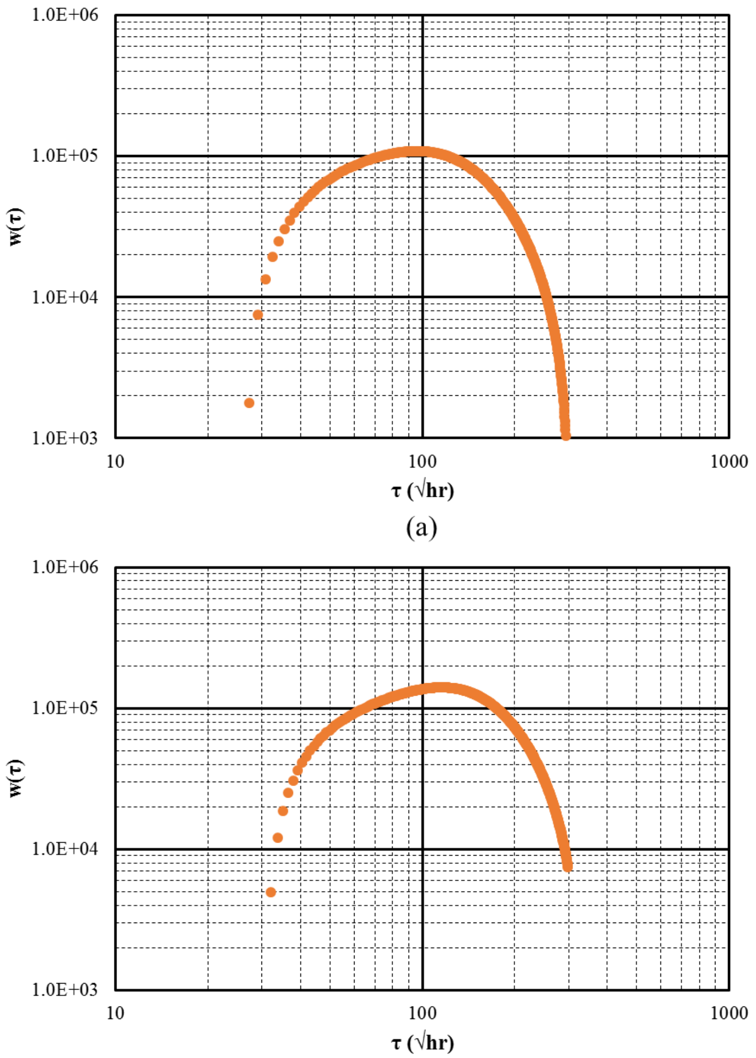

(a)

(b)

Figure 5.9 w(τ) plot of the two wells (a) Well 1 (b) Well 2

5.4 Conclusions

In this chapter, we utilize the Mangrove® as the forward simulator to conduct a field scale history matching. This field model is designed to understand the impact of tighter cluster spacing on the fracture geometry and well performance. We analyze and discuss the history matching results to examine the impact of tighter cluster spacing on the fractures and well performance. Some key conclusions for this chapter are summarized as follows:

- We developed a workflow for fracture propagation and geometry identification by history matching the treatment pressure using completion data. This workflow can generate multiple realizations of fracture network, which can serve as the starting point for the production history matching.
- Most of the fractures are planar in Eagle Ford due to large stress anisotropy. The well with wider cluster spacing develops longer fractures in all of the scenarios. However, the well with tighter cluster spacing has more complex fracture networks.

CHAPTER VI

CONCLUSIONS AND RECOMMENDATIONS

6.1 Summary and Conclusions

In this dissertation, we developed novel diagnostic plots and FMM-based simulation for complex fracture networks simulation and characterization. The following summary and conclusions can be drawn from each chapter in the dissertation:

In the second chapter, we proposed a novel diagnostic tool for the interpretation of the characteristics of the complex fracture systems and well drainage volume. We utilized the $w(\tau)$ and IRR plots for the identification of characteristic signatures that imply complex fracture geometry, formation linear flow, partial reservoir completions, fracture interference and compaction effects during production. The $w(\tau)$ analysis gives us the fracture surface area and formation diffusivity whereas the IRR analysis provides additional information on fracture conductivity. Also, quantitative analysis is conducted using the novel $w(\tau)$ plot to interpret fracture interference time, formation permeability, total fracture surface area and stimulated reservoir volume (SRV). We demonstrated the feasibility of this novel diagnostic tool using multiple synthetic and field examples.

In the third chapter, we extended the FMM-based simulation to LGRs. This required novel gridding through introduction of triangles (in 2D) and tetrahedrons (in 2.5D) to link the local and global domain and solution of the Eikonal equation in unstructured grids to compute the ‘diffusive time of flight.’ The FMM-based flow simulation reduces 3D simulation to an equivalent 1D simulation using the ‘diffusive time of flight (DTOF)’ as the spatial coordinate. The 1D simulation can be carried out using a standard finite-difference method leading to orders of magnitude savings in computation time compared to full 3D simulation for high-resolution models. Multiple numerical examples are presented to illustrate the power and validity of this extended FMM-based simulation.

In the fourth chapter, we extended the FMM-based simulation to EDFM. Similar to the LGRs workflow in Chapter III, FMM with EDFM workflow also requires novel gridding to link the embedded discrete fractures and the matrix using Delaunay triangulation. The ‘diffusive time of flight’ is calculated based on Eulerian discretization in unstructured grids. Using the ‘diffusive time of flight (DTOF)’ as a spatial coordinate, the FMM-based flow simulation reduces 3D complex fracture networks simulation to an equivalent 1D simulation. Multiple examples are shown to validate this workflow. This workflow can simulate arbitrary fracture patterns without simplification and shows good accuracy and efficiency compared to FMM with unstructured grid.

In the fifth chapter, we utilized the Mangrove® to study the impact of tighter cluster spacing on fractures and well performance. The Eagle Ford injection and production data are from two horizontal wells completed side by side. We identified the fracture geometry and properties by history matching the field injection treatment pressure using Mangrove®. The impact of cluster spacing is examined through the calibrated fracture geometry and properties. The calibrated models suggest that most of the fractures are planar in Eagle Ford. The well with wider cluster spacing tends to develop longer fractures. However, the well with tighter cluster spacing has more complex fracture networks resulting in better production performance.

6.2 Recommendations

The following points are recommended as an extension/improvement to current dissertation:

1. In the second chapter, for the field application, the drainage volume calculation is based on the global fit of both BHP and production rate. We can further investigate non-parametric regression techniques to calculate monotonic well drainage volume directly from the raw data. This novel diagnostic tool can be further used in more field cases. We can analyze the results based on different fields to reveal the similarity and difference of fracture networks at field level.
2. In the third chapter, all the implementation is conducted using Matlab. To further increase the speed of FMM, C++ implementation is necessary. For the local Eikonal solver, the parallel computing can further speed up the FMM calculation. In addition, currently the input of LGRs are designed by ourselves. We can take advantage of commercial software like Eclipse or CMG to generate the LGRs. In this way, the input format will become standard and easy to use.
3. In the fifth chapter, the FMM-based black oil simulation workflow and genetic algorithm can be used to history match the production data and further understand the difference between the two wells. In addition, we can optimize the cluster spacing, well spacing, and the usage of fracturing fluid and proppant. Under different

geomechanical and reservoir conditions, we can investigate what is the best cluster and well spacing.

NOMENCLATURE

B = Formation Volume Factor

BHP = Bottom Hole Pressure

c_t = Total Compressibility

DFM = Discrete Fracture Model

DTOF = Diffusive Time of Flight

EDFM = Embedded Discrete Fracture Model

EUR = Estimated Ultimate Recovery

FMM = Fast Marching Method

FDSim = Finite Difference Simulation

IRR = Instantaneous Recovery Ratio

k = Permeability

k_r = Relative Permeability

p = Pressure

PSS = Pseudo-Steady State

q = Flow Rate

Q = Cumulative Production

RNP = Rate Normalized Pressure

S = Saturation

SRV = Stimulated Reservoir Volume

V_{dp} = Dykstra-Parson’s Coefficient

$V_p(\tau), V_p(t)$ = Drainage Pore Volume

t = Time

t_e = Material Balance Time

$w(\tau)$ = Drainage Volume Derivative

α = Diffusivity

ϕ = Porosity

μ = Viscosity

ρ = Mass or Mole Density

τ = Diffusive Time of Flight

Subscript

g = Gas

o = Oil

p = Pore

ref = Reference Condition

w = Water

REFERENCES

Al-Kobaisi, M., Ozkan, E., Kazemi, H. et al. 2006. Pressure Transient Analysis of Horizontal Wells with Transverse, Finite-Conductivity Fractures. Paper presented at the Canadian International Petroleum Conference, Calgary, Alberta. Petroleum Society of Canada. DOI: https://doi.org/10.2118/2006-162.

An, C., Alfi, M., Yan, B. et al. 2016. A New Study of Magnetic Nanoparticle Transport and Quantifying Magnetization Analysis in Fractured Shale Reservoir using Numerical Modeling. *Journal of Natural Gas Science and Engineering* **28**: 502-521.

An, C., Yan, B., Alfi, M. et al. 2017. Estimating Spatial Distribution of Natural Fractures by Changing NMR T2 Relaxation with Magnetic Nanoparticles. *Journal of Petroleum Science and Engineering* **157**: 273-287. DOI: https://doi.org/10.1016/j.petrol.2017.07.030.

Arps, J.J. 1945. Analysis of Decline Curves. *Transactions of the AIME* **160** (1): 228-247. DOI: https://doi.org/10.2118/945228-G.

Barker, J. 1988. A Generalized Radial Flow Model for Hydraulic Tests in Fractured Rock. *Water Resources Research* **24** (10): 1796-1804.

Bourdet, D., Whittle, T., Douglas, A. et al. 1983. A New Set of Type Curves Simplifies Well Test Analysis. *World Oil* **196** (6): 95-106.

Cipolla, C.L., Lolon, E.P., Erdle, J.C. et al. 2010a. Reservoir Modeling in Shale-Gas Reservoirs. *SPE Reservoir Evaluation & Engineering* **13** (4): 638-653. DOI: https://doi.org/10.2118/125530-PA.

Cipolla, C.L., Lolon, E.P., Erdle, J.C. et al. 2010b. Reservoir Modeling in Shale-Gas Reservoirs. *SPE Reservoir Evaluation & Engineering* **13** (04): 638-653. DOI: 10.2118/125530-PA.

Datta-Gupta, A., Xie, J., Gupta, N. et al. 2011. Radius of Investigation and its Generalization to Unconventional Reservoirs. *Journal of Petroleum Technology* **63** (7): 52-55. DOI: https://doi.org/10.2118/0711-0052-JPT.

Deng, L. and King, M.J. 2016. Estimation of Relative Permeability from Laboratory Displacement Experiments Application of the Analytic Solution with Capillary Corrections. Paper presented at the International Petroleum Exhibition & Conference, Abu Dhabi, UAE. Society of Petroleum Engineers. DOI: https://doi.org/10.2118/183139-MS.

Deng, L. and King, M.J. 2018. Theoretical Investigation of Water Blocking in Unconventional Reservoirs Due to Spontaneous Imbibition and Water Adsorption. Paper presented at the Unconventional Resources Technology Conference, Houston, Texas, USA. Society of Petroleum Engineers. DOI: https://doi.org/10.15530/URTEC-2018-2875353.

Deng, L. and King, M.J. 2019. Theoretical Investigation of the Transition From Spontaneous to Forced Imbibition. *SPE Journal* **24** (1): 215-229. DOI: https://doi.org/10.2118/190309-PA.

Dijkstra, E.W. 1959. A Note on Two Problems in Connexion with Graphs. *Numerische Mathematik* **1** (1): 269-271.

Du, S., Liang, B., and Yuanbo, L. 2017. Field Study: Embedded Discrete Fracture Modeling with Artificial Intelligence in Permian Basin for Shale Formation. Paper presented at the SPE Annual Technical Conference and Exhibition, San Antonio, Texas, USA. Society of Petroleum Engineers. DOI: https://doi.org/10.2118/187202-MS.

Du, S., Yoshida, N., Liang, B. et al. 2015. Dynamic Modeling of Hydraulic Fractures Using Multisegment Wells. Paper presented at the SPE Liquids Rich Basins Conference, Midland, Texas, USA. Society of Petroleum Engineers. DOI: https://doi.org/10.2118/175540-MS.

Duong, A.N. 1989. A New Approach for Decline Curve Analysis. Paper presented at the SPE Production Operations Symposium, Oklahoma City, Oklahoma. Society of Petroleum Engineers. DOI: https://doi.org/10.2118/18859-MS.

Dykstra, H. and Parsons, R. 1950. *The Prediction of Oil Recovery by Waterflood*. Secondary Recovery of Oil in the United States. New York: American Petroleum Institute.

Evans, S., Halliburton, F., Siddiqui, S. et al. 2018. Impact of Cluster Spacing on Infill Completions in the Eagle Ford. Paper presented at the Unconventional Resources Technology Conference, Houston, Texas, 23-25 July 2018. Society of Petroleum Engineers. DOI: https://doi.org/10.15530/urtec-2018-2899323.

Fetkovich, M.J. 1980. Decline Curve Analysis Using Type Curves. *Journal of Petroleum Technology* **32** (6): 1065-1077. DOI: https://doi.org/10.2118/4629-PA.

Fujita, Y., Datta-Gupta, A., and King, M.J. 2016. A Comprehensive Reservoir Simulator for Unconventional Reservoirs That Is Based on the Fast Marching Method and Diffusive Time of Flight. *SPE Journal* **21** (6): 2276-2288. DOI: https://doi.org/10.2118/173269-PA.

Grechka, V., Li, Z., Howell, B. et al. 2018. Microseismic Imaging of Unconventional Reservoirs. Paper presented at the SEG International Exposition and Annual Meeting, Anaheim, California, USA. Society of Exploration Geophysicists.

Holditch, S.A. 2013. Unconventional Oil and Gas Resource Development–Let’s do it Right. *Journal of Unconventional Oil and Gas Resources* **1**: 2-8.

Huang, J., Yang, C., Xue, X. et al. 2016. Simulation of Coupled Fracture Propagation and Well Performance under Different Refracturing Designs in Shale Reservoirs. Paper presented at the SPE Low Perm Symposium, Denver, Colorado, USA. Society of Petroleum Engineers. DOI: https://doi.org/10.2118/180238-MS.

Iino, A. and Datta-Gupta, A. 2018. Optimizing CO2 and Field Gas Injection EOR in Unconventional Reservoirs Using the Fast Marching Method. Paper presented at the SPE Improved Oil Recovery Conference, Tulsa, Oklahoma, USA. Society of Petroleum Engineers. DOI: https://doi.org/10.2118/190304-MS.

Iino, A., Vyas, A., Huang, J. et al. 2017. Efficient Modeling and History Matching of Shale Oil Reservoirs Using the Fast Marching Method: Field Application and Validation. Paper presented at the SPE Western Regional Meeting, Bakersfield, California. Society of Petroleum Engineers. DOI: https://doi.org/10.2118/185719-MS.

Ilk, D., Anderson, D.M., Stotts, G.W.J. et al. 2010. Production Data Analysis--Challenges, Pitfalls, Diagnostics. *SPE Reservoir Evaluation & Engineering* **13** (3): 538-552. DOI: https://doi.org/10.2118/102048-PA.

Jensen, J., Lake, L.W., Corbett, P.W. et al. 2000. *Statistics for Petroleum Engineers and Geoscientists*: Gulf Professional Publishing.

Jiang, J. and Younis, R.M. 2016. Hybrid Coupled Discrete-Fracture/Matrix and Multicontinuum Models for Unconventional Reservoir Simulation. *SPE Journal* **21** (3): 1009-1027. DOI: https://doi.org/10.2118/178430-PA.

John, L., John, B.R., and John, P.S. 2003. *Pressure Transient Testing*. SPE Textbook Series. Richardson, Texas: Society of Petroleum Engineers.

Karimi-Fard, M., Durlofsky, L.J., and Aziz, K. 2004. An Efficient Discrete-Fracture Model Applicable for General-Purpose Reservoir Simulators. *SPE Journal* **9** (2): 227-236. DOI: https://doi.org/10.2118/88812-PA.

Karimi-Fard, M. and Firoozabadi, A. 2001. Numerical Simulation of Water Injection in 2D Fractured Media Using Discrete-Fracture Model. Paper presented at the SPE Annual Technical Conference and Exhibition, New Orleans, Louisiana. Society of Petroleum Engineers. DOI: https://doi.org/10.2118/71615-MS.

King, M.J., Wang, Z., and Datta-Gupta, A. 2016. Asymptotic Solutions of the Diffusivity Equation and Their Applications. Paper presented at the 78th EAGE Conference and Exhibition, Vienna, Austria. Society of Petroleum Engineers. DOI: https://doi.org/10.2118/180149-MS.

Kresse, O., Weng, X., Wu, R. et al. 2012. Numerical Modeling of Hydraulic Fractures Interaction In Complex Naturally Fractured Formations. Paper presented at the 46th U.S. Rock Mechanics/Geomechanics Symposium, Chicago, Illinois. American Rock Mechanics Association.

Kulkarni, K.N., Datta-Gupta, A., and Vasco, D.W. 2000. A Streamline Approach for Integrating Transient Pressure Data into High Resolution Reservoir Models. Paper presented at the SPE European Petroleum Conference, Paris, France. Society of Petroleum Engineers. DOI: https://doi.org/10.2118/65120-MS.

Lee, W.J. and Sidle, R. 2010. Gas Reserves Estimation in Resource Plays. *SPE Economics & Management* **2** (2): 86-91. DOI: https://doi.org/10.2118/130102-PA.

Li, L. and Lee, S.H. 2008. Efficient Field-Scale Simulation of Black Oil in a Naturally Fractured Reservoir Through Discrete Fracture Networks and Homogenized Media. *SPE Reservoir Evaluation & Engineering* **11** (4): 750-758. DOI: https://doi.org/10.2118/103901-PA.

lino, A., Onishi, T., Olalotiti-Lawal, F. et al. 2018. Rapid Field-Scale Well Spacing Optimization in Tight and Shale Oil Reservoirs Using Fast Marching Method. Paper presented at the Unconventional Resources Technology Conference, Houston, Texas, USA. Society of Petroleum Engineers. DOI: https://doi.org/10.15530/URTEC-2018-2901376.

Maity, D. and Aminzadeh, F. 2012. Framework for Time Lapse Fracture Characterization Using Seismic, Microseismic & Well Log Data. Paper presented at the SEG Annual Meeting, Las Vegas, Nevada. Society of Exploration Geophysicists.

Matthews, C.S., Brons, F., and Hazebroek, P. 1954. A Method for Determination of Average Pressure in a Bounded Reservoir. Paper presented at the Petroleum Branch Fall Meeting, Dallas. Society of Petroleum Engineers.

Mayerhofer, M.J., Lolon, E., Warpinski, N.R. et al. 2010. What Is Stimulated Reservoir Volume? *SPE Production & Operations* **25** (1): 89-98. DOI: https://doi.org/10.2118/119890-PA.

Mi, L., Zhang, Y., Jiang, H. et al. 2016. Fractured Shale Gas Reservoir Development Evaluation Based on Discrete Fracture Model. Paper presented at the SPE Kingdom of Saudi Arabia Annual Technical Symposium and Exhibition, Dammam, Saudi Arabia. Society of Petroleum Engineers. DOI: https://doi.org/10.2118/182784-MS.

Mohammed, S.A.A. and Al-Ansari, F. 1995. Modelling Of Multiple Horizontal Wells In Full Field Models Using Local Grid Refinements. Paper presented at the Middle East Oil Show, Bahrain. Society of Petroleum Engineers. DOI: https://doi.org/10.2118/29813-MS.

Moinfar, A., Varavei, A., Sepehrnoori, K. et al. 2014. Development of an Efficient Embedded Discrete Fracture Model for 3D Compositional Reservoir Simulation in Fractured Reservoirs. *SPE Journal* **19** (2): 289-303. DOI: https://doi.org/10.2118/154246-PA.

Ren, G., Jiang, J., and Younis, R.M. 2017. Fully-Coupled XFEM-EDFM Hybrid Model for Geomechanics and Flow in Fractured Reservoirs. Paper presented at the SPE Reservoir Simulation Conference, Montgomery, Texas, USA. Society of Petroleum Engineers. DOI: https://doi.org/10.2118/182726-MS.

Roussel, N.P., Manchanda, R., and Sharma, M.M. 2012. Implications of Fracturing Pressure Data Recorded during a Horizontal Completion on Stage Spacing Design. Paper presented at the SPE Hydraulic Fracturing Technology Conference, The

Woodlands, Texas, USA. Society of Petroleum Engineers. DOI: https://doi.org/10.2118/152631-MS.

Ruppert, J. 1995. A Delaunay Refinement Algorithm for Quality 2-Dimensional Mesh Generation. *Journal of Algorithms* **18** (3): 548-585.

Sethian, J.A. 1996. A Fast Marching Level Set Method for Monotonically Advancing Fronts. *Proceedings of the National Academy of Sciences* **93** (4): 1591-1595.

Sethian, J.A. 1999. Fast Marching Methods. *SIAM Review* **41** (2): 199-235.

Sethian, J.A. and Vladimirsky, A. 2000. Fast Methods for the Eikonal and Related Hamilton–Jacobi Equations on Unstructured Meshes. *Proceedings of the National Academy of Sciences* **97** (11): 5699-5703.

Shewchuk, J.R. 1996. Triangle: Engineering A 2D Quality Mesh Generator and Delaunay Triangulator. In *Applied Computational Geometry Towards Geometric Engineering*: Springer.

Simpson, M.D., Patterson, R., and Wu, K. 2016. Study of Stress Shadow Effects in Eagle Ford Shale: Insight from Field Data Analysis. Paper presented at the 50th U.S. Rock Mechanics/Geomechanics Symposium, Houston, Texas. American Rock Mechanics Association.

Song, B. and Ehlig-Economides, C.A. 2011. Rate-Normalized Pressure Analysis for Determination of Shale Gas Well Performance. Paper presented at the North American Unconventional Gas Conference and Exhibition, The Woodlands, Texas, USA. 14. Society of Petroleum Engineers. DOI: https://doi.org/10.2118/144031-MS.

Suarez, M. and Pichon, S. 2016. Combining Hydraulic Fracturing Considerations and Well Spacing Optimization for Pad Development in the Vaca Muerta Shale. Paper presented at the Unconventional Resources Technology Conference, San Antonio, Texas, USA. Unconventional Resources Technology Conference. DOI: https://doi.org/10.15530/URTEC-2016-2436107.

Sun, J. and Schechter, D. 2015. Optimization-Based Unstructured Meshing Algorithms for Simulation of Hydraulically and Naturally Fractured Reservoirs With Variable Distribution of Fracture Aperture, Spacing, Length, and Strike. *SPE Reservoir Evaluation & Engineering* **18** (4): 463-480. DOI: https://doi.org/10.2118/170703-PA.

Tafti, T.A. and Aminzadeh, F. 2012. Characterizing Fracture Network in Shale Reservoir Using Microseismic Data. Paper presented at the SPE Western Regional Meeting, Bakersfield, California, USA. Society of Petroleum Engineers. DOI: https://doi.org/10.2118/153814-MS.

Tang, J., Ehlig-Economides, C., Li, J. et al. 2018a. Investigation of Multiple Hydraulic Fracture Propagation for Low-Pressure Tight Sandstone Reservoirs in Northern Ordos Basin of Changqing Oilfield, China. Paper presented at the International

Hydraulic Fracturing Technology Conference and Exhibition, Muscat, Oman. Society of Petroleum Engineers. DOI: https://doi.org/10.2118/191454-18IHFT-MS.

Tang, J. and Wu, K. 2018b. A 3-D Model for Simulation of Weak Interface Slippage for Fracture Height Containment in Shale Reservoirs. *International Journal of Solids and Structures* **144**: 248-264. DOI: https://doi.org/10.1016/j.ijsolstr.2018.05.007.

Tang, J., Wu, K., Li, Y. et al. 2018c. Numerical Investigation of the Interactions Between Hydraulic Fracture and Bedding Planes with Non-Orthogonal Approach Angle. *Engineering Fracture Mechanics* **200**: 1-16. DOI: https://doi.org/10.1016/j.engfracmech.2018.07.010.

Tang, J., Wu, K., Zeng, B. et al. 2018d. Investigate Effects of Weak Bedding Interfaces on Fracture Geometry in Unconventional Reservoirs. *Journal of Petroleum Science and Engineering* **165**: 992-1009. DOI: https://doi.org/10.1016/j.petrol.2017.11.037.

Tang, J., Zuo, L., Xiao, L. et al. 2019. A 3-D Hydraulic Fracture Propagation Model Applied for Multiple-Layered Formation. Paper presented at the International Petroleum Technology Conference, Beijing, China. Society of Petroleum Engineers. DOI: https://doi.org/10.2523/IPTC-19238-MS.

Valko, P.P. 2009. Assigning Value to Stimulation in the Barnett Shale: A Simultaneous Analysis of 7000 Plus Production Hystories and Well Completion Records. Paper presented at the SPE Hydraulic Fracturing Technology Conference, The Woodlands, Texas. Society of Petroleum Engineers. DOI: https://doi.org/10.2118/119369-MS.

Valko, P.P. and Lee, W.J. 2010. A Better Way to Forecast Production from Unconventional Gas Wells. Paper presented at the SPE Annual Technical Conference and Exhibition, Florence, Italy. Society of Petroleum Engineers. DOI: https://doi.org/10.2118/134231-MS.

Vasco, D., Keers, H., and Karasaki, K. 2000. Estimation of Reservoir Properties Using Transient Pressure Data: an Asymptotic Approach. *Water Resources Research* **36** (12): 3447-3465.

Warren, J.E. and Root, P.J. 1963. The Behavior of Naturally Fractured Reservoirs. *SPE Journal* **3** (3): 245-255. DOI: https://doi.org/10.2118/426-PA.

Winestock, A.G. and Colpitts, G.P. 1965. Advances in Estimating Gas Well Deliverability. *Journal of Canadian Petroleum Technology* **4** (3): 111-119. DOI: https://doi.org/10.2118/65-03-01.

Wu, K., Olson, J., Balhoff, M.T. et al. 2017. Numerical Analysis for Promoting Uniform Development of Simultaneous Multiple-Fracture Propagation in Horizontal Wells. *SPE Production & Operations* **32** (1): 41-50. DOI: https://doi.org/10.2118/174869-PA.

Xian, H., Tueckmantel, C., Giorgioni, M. et al. 2018. Fracture Characterisation Through Image Log Conductive Feature Extraction. Paper presented at the Offshore Technology Conference Asia, Kuala Lumpur, Malaysia. Society of Petroleum Engineers. DOI: https://doi.org/10.4043/28462-MS.

Xie, J., Yang, C., Gupta, N. et al. 2015a. Depth of Investigation and Depletion in Unconventional Reservoirs with Fast-Marching Methods. *SPE Journal* **20** (4): 831-841. DOI: https://doi.org/10.2118/154532-PA.

Xie, J., Yang, C., Gupta, N. et al. 2015b. Integration of Shale-Gas-Production Data and Microseismic for Fracture and Reservoir Properties With the Fast Marching Method. *SPE Journal* **20** (2): 347-359. DOI: https://doi.org/10.2118/161357-PA.

Xiong, H., Wu, W., and Gao, S. 2018. Optimizing Well Completion Design and Well Spacing with Integration of Advanced Multi-Stage Fracture Modeling & Reservoir Simulation-A Permian Basin Case Study. Paper presented at the SPE Hydraulic Fracturing Technology Conference and Exhibition, The Woodlands, Texas, USA. Society of Petroleum Engineers. DOI: https://doi.org/10.2118/189855-MS.

Xue, X., Rey, A., Muron, P. et al. 2019. Simplification and Simulation of Fracture Network Using Fast Marching Method and Spectral Clustering for Embedded Discrete Fracture Model. Paper presented at the SPE Hydraulic Fracturing Technology Conference and Exhibition, The Woodlands, Texas, USA. Society of Petroleum Engineers. DOI: https://doi.org/10.2118/194368-MS.

Xue, X., Yang, C., Park, J. et al. 2018. Reservoir and Fracture-Flow Characterization Using Novel Diagnostic Plots. *SPE Journal* **Preprint**. DOI: https://doi.org/10.2118/194017-PA.

Xue, X., Yang, C., Sharma, V.K. et al. 2016. Reservoir and Fracture Flow Characterization Using a Novel w(τ) Formulation. Paper presented at the Unconventional Resources Technology Conference, San Antonio, Texas, USA. Society of Petroleum Engineers. DOI: https://10.15530/URTEC-2016-2440083.

Yang, C., Sharma, V.K., Datta-Gupta, A. et al. 2015. A Novel Approach for Production Transient Analysis of Shale Gas/Oil Reservoirs. Paper presented at the Unconventional Resources Technology Conference, San Antonio, Texas, USA. Society of Petroleum Engineers. DOI: https://doi.org/10.15530/URTEC-2015-2176280.

Yang, C., Xue, X., Huang, J. et al. 2016. Rapid Refracturing Candidate Selection in Shale Reservoirs Using Drainage Volume and Instantaneous Recovery Ratio. Paper presented at the Unconventional Resources Technology Conference, San Antonio, Texas, USA. Society of Petroleum Engineers. DOI: https://doi.org/10.15530/URTEC-2016-2459368.

Yang, C., Xue, X., King, M.J. et al. 2017. Flow Simulation of Complex Fracture Systems With Unstructured Grids Using the Fast Marching Method. Paper presented at the Unconventional Resources Technology Conference, Austin, Texas, USA. Society of Petroleum Engineers. DOI: https://doi.org/10.15530/URTEC-2017-2691393.

Yang, D., Xue, X., and Chen, J. 2018. High Resolution Hydraulic Fracture Network Modeling Using Flexible Dual Porosity Dual Permeability Framework. Paper presented at the SPE Western Regional Meeting, Garden Grove, California, USA. Society of Petroleum Engineers. DOI: https://doi.org/10.2118/190096-MS.

Yu, W., Zhang, Y., Varavei, A. et al. 2018. Compositional Simulation of CO2 Huff-n-Puff in Eagle Ford Tight Oil Reservoirs with CO2 Molecular Diffusion, Nanopore Confinement and Complex Natural Fractures. Paper presented at the SPE Improved Oil Recovery Conference, Tulsa, Oklahoma, USA. Society of Petroleum Engineers. DOI: https://doi.org/10.2118/190325-MS.

Zhang, S. and Zhu, D. 2017. Inversion of Downhole Temperature Measurements in Multistage Fracture Stimulation in Horizontal Wells. Paper presented at the SPE Annual Technical Conference and Exhibition, San Antonio, Texas, USA. Society of Petroleum Engineers. DOI: https://doi.org/10.2118/187322-MS.

Zhang, S. and Zhu, D. 2019a. Efficient Flow Rate Profiling for Multiphase Flow in Horizontal Wells Using Downhole Temperature Measurement. Paper presented at the International Petroleum Technology Conference, Beijing, China. Society of Petroleum Engineers. DOI: https://doi.org/10.2523/IPTC-19138-MS.

Zhang, S. and Zhu, D. 2019b. Inversion of Downhole Temperature Measurements in Multistage Fracture Stimulation of Horizontal Wells in Unconventional Reservoirs *SPE Production & Operations* **Preprint**. DOI: https://doi.org/10.2118/187322-PA.

Zhang, Y., Bansal, N., Fujita, Y. et al. 2016. From Streamlines to Fast Marching: Rapid Simulation and Performance Assessment of Shale-Gas Reservoirs by Use of Diffusive Time of Flight as a Spatial Coordinate. *SPE Journal* **21** (5): 1883-1898. DOI: https://doi.org/10.2118/168997-PA.

Zhou, J., Huang, H., and Deo, M. 2016. Numerical Study of Critical Role of Rock Heterogeneity in Hydraulic Fracture Propagation. Paper presented at the 50th US Rock Mechanics/Geomechanics Symposium. American Rock Mechanics Association.

Zhou, Z., Zhang, G.Q., Zhou, D. et al. 2016. Analysis of Shale Gas Hydraulic Fracture Induced Stress and Optimization of Perforation Cluster Spacing. Paper presented at the ISRM International Symposium, Ürgüp, Turkey. International Society for Rock Mechanics and Rock Engineering.

Zhu, D., Hill, D., and Zhang, S. 2018. Using Temperature Measurements from Production Logging/Downhole Sensors to Diagnose Multistage Fractured Well Flow Profile. Paper presented at the SPWLA 59th Annual Logging Symposium, London, UK. Society of Petrophysicists and Well-Log Analysts.

APPENDIX A

INVERSION PROCEDURE FOR THE W(τ) FUNCTION

The w(τ) function is inverted in a way which truncates the infinite integral to be finite and divides the domain into smaller intervals. Our goal is to invert for a piecewise constant w(τ) function.

$$V_d(t_i)=\sum_{j=1}^{N}\int_{\tau_a}^{\tau_b} w(\tau)\exp\left(-\frac{\tau^2}{4t_i}\right)d\tau \tag{A-1}$$

Any type of w(τ) function can be assumed, here w(τ) is considered as piecewise constant. This is a fair assumption for two reasons: firstly, we are not trying to obtain a purely analytical solution of w(τ) and it is not possible to so without an analytical formula for $V_d(t)$; and secondly, it is good approximation as long as a sufficient number of intervals are used. The integral in Eq. (A-1) can be explicitly expressed in terms of error function as follows:

$$V_d(t_i)=\sqrt{\pi t_i}\sum_{j=1}^{N} w(\tau_i)\cdot\left(Erf\left(\frac{\tau_{jb}}{2\sqrt{t_i}}\right)-Erf\left(\frac{\tau_{ja}}{2\sqrt{t_i}}\right)\right) \tag{A-2}$$

We end up solving a linear matrix Ax=b, where each individual terms are expressed as Eq. (A-3).

$$a_{ij}=\sqrt{\pi t_i}\left(Erf\left(\frac{\tau_{jb}}{2\sqrt{t_i}}\right)-Erf\left(\frac{\tau_{ja}}{2\sqrt{t_i}}\right)\right),\ x_i=w(\tau_i),\text{ and }b_i=V_d(t_i) \tag{A-3}$$

The error function gets quite close to unity (0.9996), at arguments larger than 2.5, thus the coefficient is very small. The coefficient matrix quickly becomes singular and the entire system is not readily solvable. We can further reduce the upper limit of the integral for particular time t, here we choose $5\sqrt{t}$. For the first step, i.e. smallest time t_1, the $w(\tau_1)$ is considered constant in the entire interval and can be solved directly. And at the *n*th interval, all previous $w(\tau)$ values have been solved and the corresponding interval for solved value $w(\tau_i)$ is $[2\sqrt{t_{i-1}}, 2\sqrt{t_i}]$.

$$\begin{gathered}
V_d(t_1) = \sqrt{\pi t_1}\, w(\tau_1) \cdot \left(Erf\left(\frac{5\sqrt{t_1}}{2\sqrt{t_1}} \right) - Erf\left(\frac{0}{2\sqrt{t_1}} \right) \right) \approx \sqrt{\pi t_1}\, w(\tau_1) \\
V_d(t_2) = \sqrt{\pi t_2}\, w(\tau_1) \cdot \left(Erf\left(\frac{2\sqrt{t_1}}{2\sqrt{t_2}} \right) - Erf\left(\frac{0}{2\sqrt{t_2}} \right) \right) + \sqrt{\pi t_2}\, w(\tau_2) \cdot \left(Erf\left(\frac{5\sqrt{t_2}}{2\sqrt{t_2}} \right) - Erf\left(\frac{2\sqrt{t_1}}{2\sqrt{t_2}} \right) \right) \\
\cdots\cdots \\
V_d(t_n) = \sqrt{\pi t_n} \sum_{j=1}^{n-1} w(\tau_j) \cdot \left(Erf\left(\frac{2\sqrt{t_j}}{2\sqrt{t_n}} \right) - Erf\left(\frac{2\sqrt{t_{j-1}}}{2\sqrt{t_n}} \right) \right) + \sqrt{\pi t_n}\, w(\tau_n) \cdot \left(Erf\left(\frac{5\sqrt{t_n}}{2\sqrt{t_n}} \right) - Erf\left(\frac{2\sqrt{t_{n-1}}}{2\sqrt{t_n}} \right) \right)
\end{gathered} \tag{A-4}$$

Through this way, we can obtain fairly good $w(\tau)$ function, which shows distinct characteristics and helps explaining the differences of model responses.